UNIVERSITÀ DEGLI STUDI DI PADOVA

Dipartimento di Fisica e Astronomia *"Galileo Galilei"*

Corso di Laurea Magistrale in Astronomia

Characterisation of a nuclear transient in NGC 6315

Relatore:
Prof. Stefano Ciroi
Correlatore:
Dr. Andrea Pastorello

Laureanda:
Irene Salmaso

Anno Accademico 2019/2020

Veni ab astris et ad astra revertam.

"Per correr miglior acque alza le vele
omai la navicella del mio ingegno,
che lascia dietro a sé mar sì crudele;
e canterò di quel secondo regno
dove l'umano spirito si purga
e di salire al ciel diventa degno."

Divina Commedia, Purgatorio, Canto I, vv. 1-6

CONTENTS

LIST OF FIGURES

LIST OF TABLES

SUMMARY

In questa tesi ci si concentra sullo studio di transienti nel nucleo di galassie. Questi possono essere principalmente di tre tipi: nuclei galattici attivi (AGN), supernovae (SNe) o tidal disruption events (TDE).
Gli AGN sono fenomeni legati al buco nero supermassiccio (SMBH) che si trova al centro delle galassie. Alcuni SMBHs sono circondati da un disco di accrescimento che genera un continuo luminoso non termico. Nubi di gas ionizzate dal continuo e dischi di polvere forniscono diversi contributi all'emissione caratteristica degli AGN, che può essere quindi molto varia. L'emissione degli AGN è altresì molto variabile, a causa di fluttuazioni che si propagano nel disco. Questa variabilità fa rientrare gli AGN tra i fenomeni transienti.
Le SNe sono esplosioni di stelle evolute. Le SNe "core-collapse" derivano da stelle massicce ($M \gtrsim 8M_{\odot}$). Esse arrivano ad avere un core di ferro alla fine della loro evoluzione, il quale non può essere fuso ulteriormente in elementi più pesanti. Viene quindi a mancare l'energia nucleare che supporta la stella ed essa collassa. Il nucleo interno collassa e diventa talmente denso da essere incomprimibile, perciò il materiale più esterno che vi cade sopra viene espulso in una violenta esplosione, lasciandosi dietro un resto compatto (stella di neutroni o buco nero). Le SNe "termonucleari" derivano da sistemi binari in cui almeno una delle due componenti è una nana bianca che accresce materiale dalla compagna attraverso il lobo di Roche. Quando la nana bianca raggiunge la massa limite di Chandrasekar ($1.44M_{\odot}$), il materiale nel nucleo subisce una serie di esplosioni nucleari, espellendo tutto il materiale stellare nel mezzo interstellare e non lasciando alcun resto compatto.
Ci sono poi molti transienti stellari che ricordano alcune caratteristiche delle SNe, quali evoluzione della curva di luce e/o dello spettro. In particolare, i TDE sono stelle che vengono disgregate dal potenziale gravitazionale del SMBH centrale. La massa stellare, cadendo sul SMBH, dà luogo a un transiente luminoso.

Sebbene la ricerca nell'ambito dei transienti abbia una lunga storia, transienti in nuclei galattici sono stati studiati solo negli ultimi vent'anni. Ciò è in parte dovuto al fatto che tradizionalmente le osservazioni di AGN sono fatte ad energie molto alte o molto basse, mentre transienti stellari sono studiati soprattutto in ottico, UV e IR. Negli ultimi anni, cataloghi di AGN sempre più accurati e scoperte di nuovi tipi di transienti stellari hanno catturato l'interesse dei ricercatori, portando attenzione a questo filone di ricerca.
È in questo filone che si innesta la ricerca alla base di questa tesi. SNhunt133 è un fenomeno transiente scoperto nel 2012 nel nucleo della galassia NGC 6315. La sua classificazione è stata dibattuta tra AGN e TDE da diversi autori. Lo scopo della tesi è analizzare i dati raccolti da diversi osservatori, di tipo sia fotometrico che spettroscopico, per caratterizzare il transiente. I dati raw sono stati ridotti e analizzati. Sono state eseguite analisi della curva di luce, del continuo spettrale e delle righe di emissione. Dopo attente considerazioni e confronti con altri transienti nucleari, si è concluso che i dati raccolti non corrispondono a nessuno dei transienti più comuni, e si ipotizza che SNhunt133 sia un episodio di variabilità del nucleo galattico.
La tesi è strutturata come segue:

- Nel capitolo 1 si dà una breve overview dei transienti conosciuti ad oggi, con descrizione delle rispettive tipiche caratteristiche spettro-fotometriche;
- Nel capitolo 2 si descrive più nel dettaglio l'emissione di AGN, SNe e TDE. Si fornisce inoltre un modello fisico che spieghi l'emissione osservata;
- Nel capitolo 3 si introducono SNhunt133 e la sua galassia ospite e si danno stime di redshift, distanza e reddening;
- Nel capitolo 4 si presenta il set di dati fotometrici, se ne descrive la riduzione e si presenta l'analisi attuata;
- Nel capitolo 5 si presenta il set di dati spettroscopici, se ne descrive la riduzione e si presenta l'analisi attuata;
- Nel capitolo 6 si discutono i risultati e si confrontano con altri transienti noti. Si traggono infine le conclusioni.

CHAPTER

1

INTRODUCTION

The search, classification and comprehension of transient astrophysical sources have attracted the interest of astrophysicists. Since ancient times, humankind was fascinated by novel lights in the sky. Nevertheless it was only in recent epochs that, with the aid of new discoveries in the fields of nuclear physics and the newborn astrophysics, transient sources started to be understood. New discoveries piqued researchers' interest and a huge work was done on classical stellar transient sources such as novae and supernovae (SNe), as well as Active Galactic Nuclei (AGN) which, on the contrary, are not related to stellar sources but are intrinsic variability of the galaxy cores.

Although research on transient sources has a long and thriving history, the systematic studies of transient astrophysical objects hosted in galactic nuclei have been initiated about twenty years ago. This is not only due to object properties, such as a low intrinsic brightness that would make them difficult to spot amidst bright sources like galactic nuclei until recent times. In fact, these objects are usually quite bright. Part of the reason is to ascribe to researchers and their interests: up until a couple decades ago, there was limited literature on AGN photometric variability. The unified model [Antonucci, 1993], which put together blazars, Seyfert galaxies and quasars under the broad category of AGN, has grown the interest of researchers towards this field and gave scientist a clearer vision of the ongoing phenomena. Given the historical background, it is not surprising that the majority of AGN observations were performed mostly at high energy or at radio wavelengths.

Before, AGN were usually classified through spectral features, with help from information at high frequency at most. Optical photometry was not commonly employed. By the end of the 20^{th} century, AGN variability started to be investigated also with UV and optical photometry (e.g. [Netzer et al., 1996], [Giveon et al., 1999], [Webb and Malkan, 2000]). The research on long

term variability, with timescales of months to years which is of interest for this thesis, has been performed along with research on intranight variability [Sagar et al., 2004], [Stalin et al., 2004]. Nowadays, novel surveys and observational strategies allow to detect small scale variations in bright sources. Moreover, more completed and detailed AGN catalogues make the discrimination of different types of nuclear sources easier, as it is less and less likely to confuse a proper transient, coming from a stellar object, with an unknown AGN. Last but not least, in the past the only known transients were novae and SNe, whereas many new object classes started to be discovered, both foreseen in theory and not. Huge investments were made in order to gain a better understanding of these particular sources.
Figure 1.1 shows the various categories of known transients following a modern classification scheme, in peak luminosity vs. luminosity timescale diagram. A brief overview of transients visible outside the Milky Way is reported in Section 1.1.

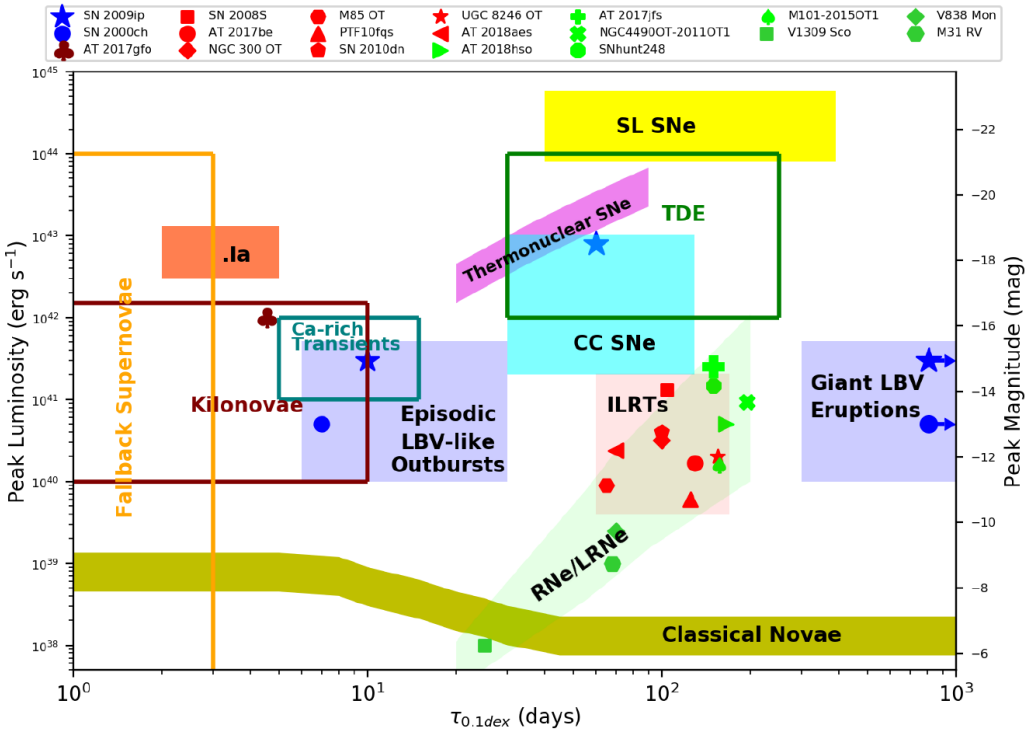

Figure 1.1: Plot of typical peak luminosity of known transients in the local Universe versus their respective timescale of evolution [Cai, 2019].

1.1 The Transient Forest

1.1.1 Novae

Novae are eruptive events that happen in a close binary system where one of the two stars is a white dwarf (WD) and the other is a main-sequence star. The white dwarf accretes material from the companion through an accretion disk. Occasionally, the WD erupts and expels materials outward, polluting the interstellar medium and enhancing its luminosity. The outburst is not terminal, meaning that the star survives the event and can continue accreting material from the companion, although occasionally a readjustment of angular momentum occurs. Nova eruptions can thus be periodic events [Rose, 1968], [Fujimoto, 1982].
The absolute magnitude of a nova light-curve varies from +4 mag at the lowest point to −9 mag at peak magnitude [Mobberley, 1999]. Optical spectra show Balmer lines and either Fe II or He and N, with a distinct P-Cygni profile in later, photospheric-phase. Fe II lines likely come from winds generated after the shock, whereas He and N come from the ejected shell right at the outburst maximum [Williams, 1992].

1.1.2 Core-collapse Supernovae

Core-collapse supernovae are the endpoint of the life of massive stars. These stars have an initial mass $M \gtrsim 8M_{\odot}$. Those with a mass between $7-8$ and $9\ M_{\odot}$ develop O-Ne degenerate cores, where a collapse can be triggered by electron capture: if the core mass grows to $1.37\ M_{\odot}$, which is the critical mass for Ne ignition, electrons are captured by ^{24}Mg and ^{20}Ne [Nomoto, 1984]; this removes thermal energy (2 MeV per nucleon) that sustains the core. The electron pressure then decreases and the core collapses.
Stars with initial mass higher than $9\ M_{\odot}$ can burn all elements in their core up to iron. At this point, the core is made of neutron-rich nuclei of the iron group, mainly ^{56}Fe. Iron is the element with the most stable nuclear configuration, thus it is not possible for a star to continue nuclear fusion without an energy supply and element production is quenched. Without nuclear energy to support it, the star shrinks under its own gravity and starts collapsing.
The inner core collapses, increasing its density until it becomes almost incompressible. The outer material, which keeps free-falling towards the nucleus, bounces back on the core, generating a strong shock outwards.
During the collapse, an energy of about 3×10^{53} erg is liberated, mostly as neutrino losses. About 1% is needed to blow out the envelope, whilst 10^{49} erg go in radiation [Branch and Wheeler, 2017]. After the explosion, a compact remnant is formed in the centre of the expanding envelope. Depending on the initial stellar mass and the specific physical conditions of the explosion, it can either be a neutron star or a black hole. I will go more in depth on the physics of CC-SNe in Section 2.2.1.
There are several types of core-collapse supernovae (for a review, see [Gal-Yam, 2017]), their classification being based on photometric and spectroscopic properties:

- **Regular SN II** are divided in two different classes based on light-curve evolution: **II-P**,

which show a red plateau, and **II-L**, which are rapidly declining. II-P SNe have average absolute peak magnitude of -16.80 ± 0.37 (B), whereas type II-L SNe have average absolute peak magnitude of -17.98 ± 0.34 (B) [Richardson et al., 2014]. They are rich in H, which dominates early spectra and the expansion velocity at peak is 10000 km/s. Later, metal lines are also detected [Gal-Yam, 2017];

- **1987A-like** are regular type II SNe with an initial radius smaller by an order of magnitude. The rise to peak is then longer and their peculiar secondary peak is the equivalent of a plateau. Progenitors are likely blue supergiants [Taddia et al., 2016];

- **Interacting SN IIn** have average absolute peak magnitude of -18.62 ± 0.32 (B) [Richardson et al., 2014], whereas the expansion velocity is not determinable, since the shock of the interaction hides any photospheric feature. Their spectra are quite diverse and several show narrow emission lines of H, He and FeII. The narrow peak is due to photo-ionisation of slow moving circumstellar material (CSM) from high-energy photons produced in the collision between CSM and ejecta [Schlegel, 1990];

- **Transitional SN IIb** have average absolute peak magnitude of -17.03 ± 0.45 (B) [Richardson et al., 2014] and expansion velocity of 8400 km/s at peak. They are called "transitional" because their spectra are similar to those of type II SNe in early times, and then they evolve to resemble type Ib SNe. Their light-curves often have an initial bump and are overall similar to those of type Ib and Ic SNe [Modjaz et al., 2014];

- **Regular SN Ib** have average absolute peak magnitude of -17.54 ± 0.33 (B) [Richardson et al., 2014] and expansion velocity of 10000 km/s at peak. Their spectra show strong He features and no H lines [Modjaz, 2007];

- **Interacting SN Ibn** peak around -19 mag (R), but they can span about 2 magnitudes around that value [Pastorello et al., 2008], [Hosseinzadeh et al., 2017]. Their spectra can be heterogeneous, but are discernible from other types of SNe because of the strong, narrow He lines in early spectra [Pastorello et al., 2016]. As with SN IIn, the narrow peak is due to photo-ionisation of the CSM caused by energetic photons produced in the shocked material [Chevalier et al., 1994];

- **SN Ic** have average absolute peak magnitude of -17.67 ± 0.40 (B) [Richardson et al., 2014] and expansion velocity of 10000 km/s at peak. They lack both H and He, which could assimilate them to type Ia SNe, but at peak they have shallower Si II absorption lines around 6150 Å, and Ca II and O I (λ7774 Å) dominate the spectrum [Modjaz et al., 2014];

- **SN Ic-BL** have average absolute peak magnitude of -19.0 ± 1.1 (R) [Drout et al., 2011] and expansion velocity of 19000 km/s at peak. They also lack both H and He and the expansion velocity of the ejected material is so high that the spectral lines generate broad blends [Modjaz, 2007].

1.1.3 Type Ia Supernovae

Type Ia supernovae are also called "Thermonuclear supernovae" because of the mechanism of explosion. Much like novae, these transients happen in close binary systems where one of the components is a C-O WD accreting mass from its companion through a Roche lobe. When the WD mass reaches the limit for stability, the Chandrasekar mass (1.44 $M_{\odot}$), the temperature increase in the degenerate core is high enough to lift the degeneracy. This allows all the material in the core to incinerate to Fe-peak elements. The burning flame propagates outward, whilst the material behinds it undergoes explosive nuclear burning. The released energy is $\sim 10^{51}$ erg, enough to overcome the binding energy of the WD. In this case, no compact remnant is left behind, and the whole stellar material is expelled into the interstellar medium [Branch and Wheeler, 2017]. I will delve into the physics of explosion in Section 2.2.2.
In general, SN Ia are classified through their spectra, which lack both H and He features. Nevertheless, there are several peculiar features that allow to distinguish different type Ia subtypes. Here are the best known (a comprehensive review is in [Taubenberger, 2017]):

- **Regular SNe Ia** have average absolute peak magnitude of -19.26 ± 0.20 (B) [Richardson et al., 2014], and expansion velocity of 11000 km/s at peak. Their spectra show no H, no He, but strong Si II, O, S, Ca, Fe I, Fe II, Fe III, Co and Ni. The IR light-curve has a secondary peak;

- **1991T-like** average peak magnitude is 0.4–0.5 mag brighter than regular type Ia, and their expansion velocity is around 10000 km/s at peak [Taubenberger, 2017]. Fe III dominates before maximum light. They tend to be more luminous, because they produce more ^{56}Ni, than regular type Ia and also their decline is slower;

- **1991bg-like** have absolute peak magnitude between -16.7 and -17.7 mag (B) and expansion velocity of 10000 km/s at peak [Taubenberger et al., 2008]. Between $4000 - 5000$ Å the absorption is dominated by Ti II. The light-curve shows no secondary infrared peak and has a faster decline compared to regular type Ia;

- **Super-Chandra** have absolute peak magnitude of between -19.5 and -20.4 (B) and expansion velocity of 8000 km/s in photospheric phase [Taubenberger, 2017]. There is no Fe III before maximum, but at peak C II is very strong. Super-Chandra are only about 1% of all SNe Ia;

- **SN Iax (2002cx-like)** have absolute peak magnitude between -14.2 and -18.9 (B) and expansion velocity of less than 8000 km/s at peak [Foley et al., 2013]. Their spectral evolution resembles that of 91T-like but they are usually fainter and with narrower spectral lines;

- **SN Ia-CSM** have absolute peak magnitude between -21.3 and -19 (R) and expansion velocity of 2000 km/s (from Hα) in late spectra. Their spectra are similar to those of 91T-like; in addition they have a blue continuum and strong Balmer lines due to interaction with the circumstellar medium [Silverman et al., 2013]. The interpretation as thermonuclear disruption of a WD within a H-rich CSM is disputed as for some authors (e.g. [Benetti et al., 2006]) their progenitors could be core-collapse SNe interacting with a hydrogen-rich

circumstellar medium.

1.1.4 Gap Transients

In past years, when only novae and supernovae were acknowledged, there was a gap in luminosity between the two classes. Novel transients that appeared to have intermediate characteristics were generally dubbed "gap-transients" [Pastorello and Fraser, 2019], [Kasliwal, 2012] because they appeared to fill the luminosity gap between the two classes (absolute magnitudes range between -9 and -15, in general). However, this does not imply that the formation mechanism is the same, nor that there is a continuity in the mass of the progenitors. Some of these transients are also called "supernova impostors" because, although they mimic observed properties of SNe, they do not come from the last stage of nuclear burning in massive stars. Moreover, the progenitor can survive the event. The most famous and best studied transients are:

- **Luminous Red Novae (LRNe)** span a wide range in luminosity, from -4 to -15. The luminosity is tied to the progenitor mass, with more luminous LRNe coming from more massive progenitors. More luminous events are also rarer than fainter ones. The light-curve has a distinct large-amplitude double peak. Spectra are blue during the first peak, with strong Balmer lines, whereas during their evolution they become redder and metal lines in absorption tend to prevail [Pastorello et al., 2019]. The most likely formation scenario is the merging of "non-degenerate" stars [Tylenda et al., 2011];

- **Intermediate Luminosity Red Transients (ILRTs)** show a slow rise to maximum light and a linear post-peak decline, whilst the peak magnitude stays dimmer than typical SNe, between -12 and -14 mag, although the prototypical object of this class, SN 2008S, reached -14 mag (R). Spectra are blue at the beginning and tend to become redder with time [Cai, 2019]. Likely progenitors are weak electron-capture SNe coming from extreme Asymptotic Giant Branch (eAGB) stars [Thompson et al., 2009];

- **Ca-rich transients** have absolute peak magnitude between -15.5 and -16.5 (R) and expansion velocity between 6000 and 11000 km/s. Late spectra show CaII features and the light-curves, albeit similar to those of regular type Ib, decline faster [Kasliwal et al., 2012]. It is debated that their progenitor could be a binary WD undergoing thermonuclear collapse [Perets et al., 2010];

- **Luminous Blue Variables (LBVs)**. LBV is an evolutionary phase characteristic of massive ($\gtrsim 40 M_{\odot}$) stars that become blue supergiants and can erupt multiple times [Humphreys and Davidson, 1994], since the star survives the outbursts. The light-curve is usually erratic, with peak magnitude fainter than normal supernovae, since they can reach -14 mag (R) at maximum. Spectra have blue continuum and narrow Balmer lines [Tartaglia et al., 2015].

In Figure 1.2 examples of typical light-curves for some of these objects are shown, whereas in Figure 1.3 typical spectra with remarkable spectral lines pointed out are plotted.

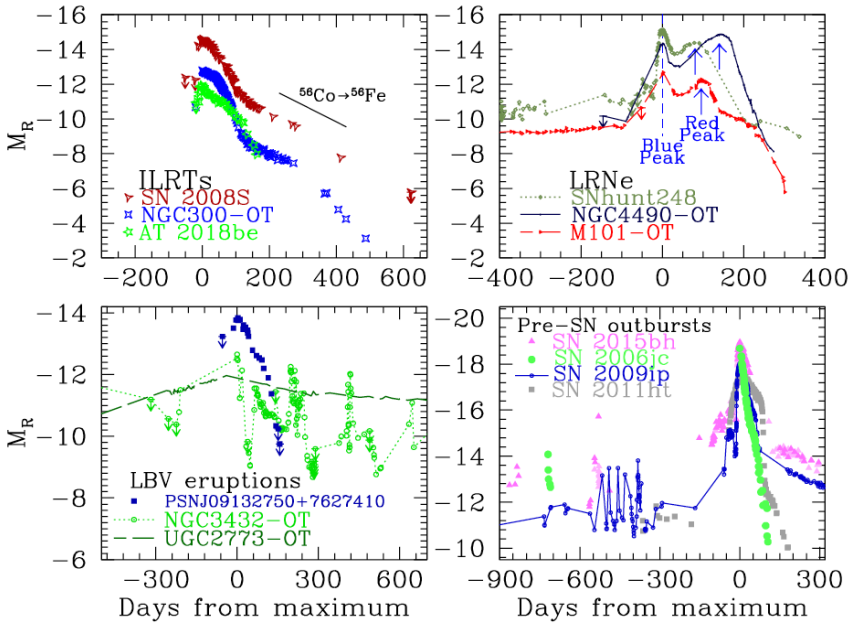

Figure 1.2: Top left: light-curves of typical ILRTs. Top right: light-curves of typical LRNe. Bottom left: light-curves typical of LBVs. Bottom right: light-curves of pre-supernova outbursts followed by type IIn SN explosions. The image is from [Pastorello and Fraser, 2019].

1.1.5 Luminous Transients

Novel surveys not only discovered intermediate-luminosity transients, but also very luminous events that were difficult to reconcile with canonical SN explosion mechanisms, due to their extreme luminosity and their peculiar spectro-photometric characteristics. These transients are:

- **Super-luminous Supernovae (SLSNe)**. As the name suggests, these events are intrinsically brighter than the average SN, peaking around −21 mag [Gal-Yam, 2017]. Their expansion velocity in photospheric phase is 14000 km/s, and they are hosted by very faint, dwarf, metal-poor galaxies [Quimby et al., 2011]. SLSNe are divided into two classes: SLSN-II, hydrogen-rich, and SLSN-I, hydrogen-poor. Early spectra have a blue continuum, which peaks in the UV. They show a pattern of characteristic O II lines near peak light [Howell, 2017] which disappear short after, leaving Ca II, Mg II, Si II and Fe II to dominate. Late spectra resemble Type Ic SNe, although with a longer timescale [Pastorello et al., 2010].
  The extreme luminosity of SLSNe cannot be explained solely by ^{56}Ni powering. The most favoured powering mechanisms are the energy deposition by a magnetar or an interaction of the ejecta with circumstellar material (e.g. [Inserra et al., 2013], [Nicholl et al., 2013]).

- **Tidal Disruption Events (TDEs)**. TDEs come from stars that are disrupted by the gravitational pull of a super-massive black hole (SMBH). The disrupted mass, falling onto the black hole, is what powers the transient [Rees, 1988]. Spectroscopically, TDEs

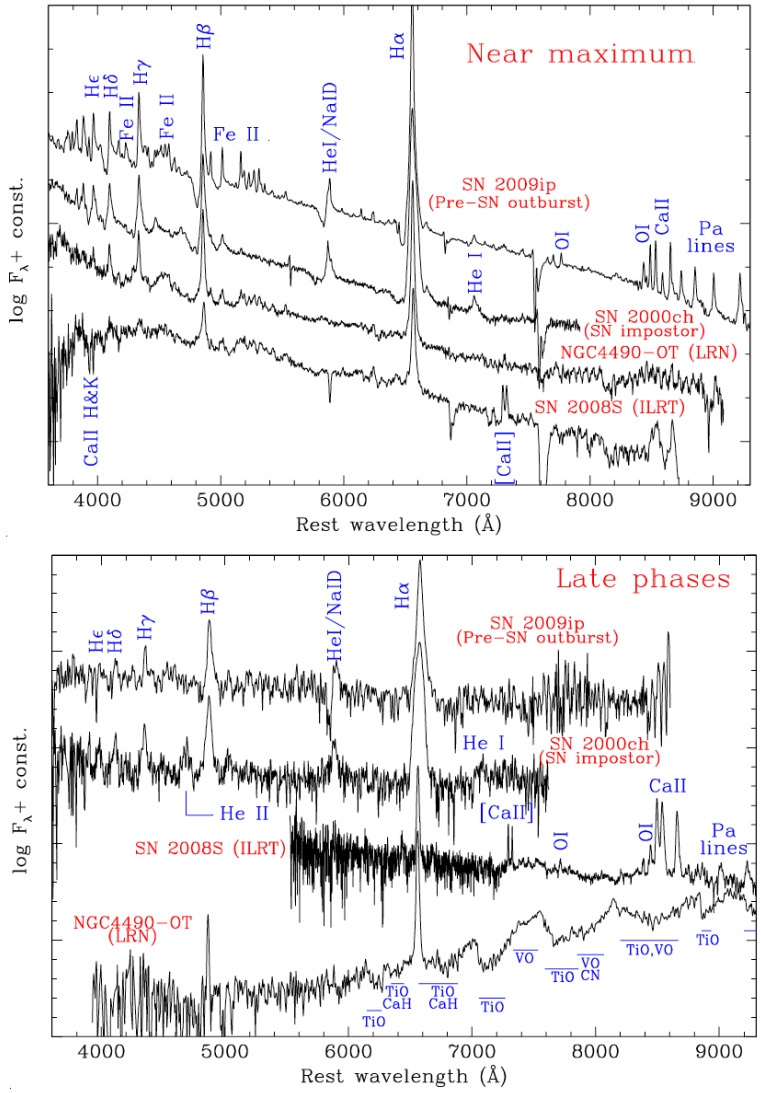

Figure 1.3: Top: Spectra of different Gap Transients taken near maximum light. Bottom: Spectra of the same targets but obtained months to years after maximum light. The figure is from [Pastorello and Fraser, 2019].

show blue continuum and broad emission lines, whilst the light-curve has a longer rise time to peak magnitude and negligible cooling compared to normal SNe, and a power-law decline [van Velzen et al., 2011]. I will more widely discuss TDEs in Section 2.3 in the context of the transient discussed in this thesis.

1.1.6 Kilonovae

Kilonovae (KNe) are the electro-magnetic counterpart produced by the merge of two neutron stars (NSs) or a NS and a BH in a close binary system. The two components spiral around each other, whilst emitting gravitational waves.
The optical emission is thermal, due to r-process radioactive decay. In the case of AT2017gfo (SSS17a), to date the best sampled optical counterpart of a gravitational wave event [Abbott et al., 2017a], the light-curve followed an initial decline with t^{-1}, which then changed to t^{-3} [Kashyap et al., 2019]. Whilst the early spectrum showed a blue, featureless continuum, broad spectral features given by lanthanides appeared in later spectra. In Figure 1.4 a sample of photometric and spectroscopic observation is shown, as retrieved from [Pian et al., 2017]. The optical emission is accompanied by a weak X-ray source, and a delayed radio emission due to ejecta interaction with the medium [Abbott et al., 2017b].
The compact remnant can either be a BH or a NS, depending on the specific condition of the merge, such as mass of the NSs and characteristics of the environment [Kawaguchi et al., 2020].

1.1.7 Gamma-ray bursts

Gamma-ray bursts (GRBs) are highly energetic transients. Classically, they were divided in two classes following the event duration: short (< 2 s) and long (> 2 s). Short-GRB are usually harder, whilst long-GRB are soft [Kouveliotou et al., 1993]. Later, GRB events have been re-sorted into three classes: class I, which is comprised of long (10-20 s), bright, soft events; class II, whose GRBs are short (< 2 s), faint in brightness but hard; and class III, in which GRBs are of intermediate duration ($2 - 5$ s), intermediate brightness and soft [Mukherjee et al., 1998].
Usually, long events are associated with type Ic-BL SNe which had previously lost part of their envelope through stellar wind or because of a binary companion [Mazzali et al., 2005]. Short GRBs are part of the electromagnetic emission coming from the coalescence of compact objects, such as binary NS mergers [Abbott et al., 2008].
The GRB emission is due to the dissipation of the jet-like, ultrarelativistic explosion and the spectrum is not thermal, with an energy peak in keV or GeV.
GRB events are not confined to the gamma domain, instead the majority of long GRBs show an optical afterglow when a shock, usually with the circumstellar material, slows the jet. The afterglow spectrum resembles a power-law, with absorption lines due to material between the source and the observer [Piran, 2004].

In this Section, I presented a general picture of the transient zoo to date. Among the variety of new transients categories, a lot of attention was directed towards transients in the nucleus of

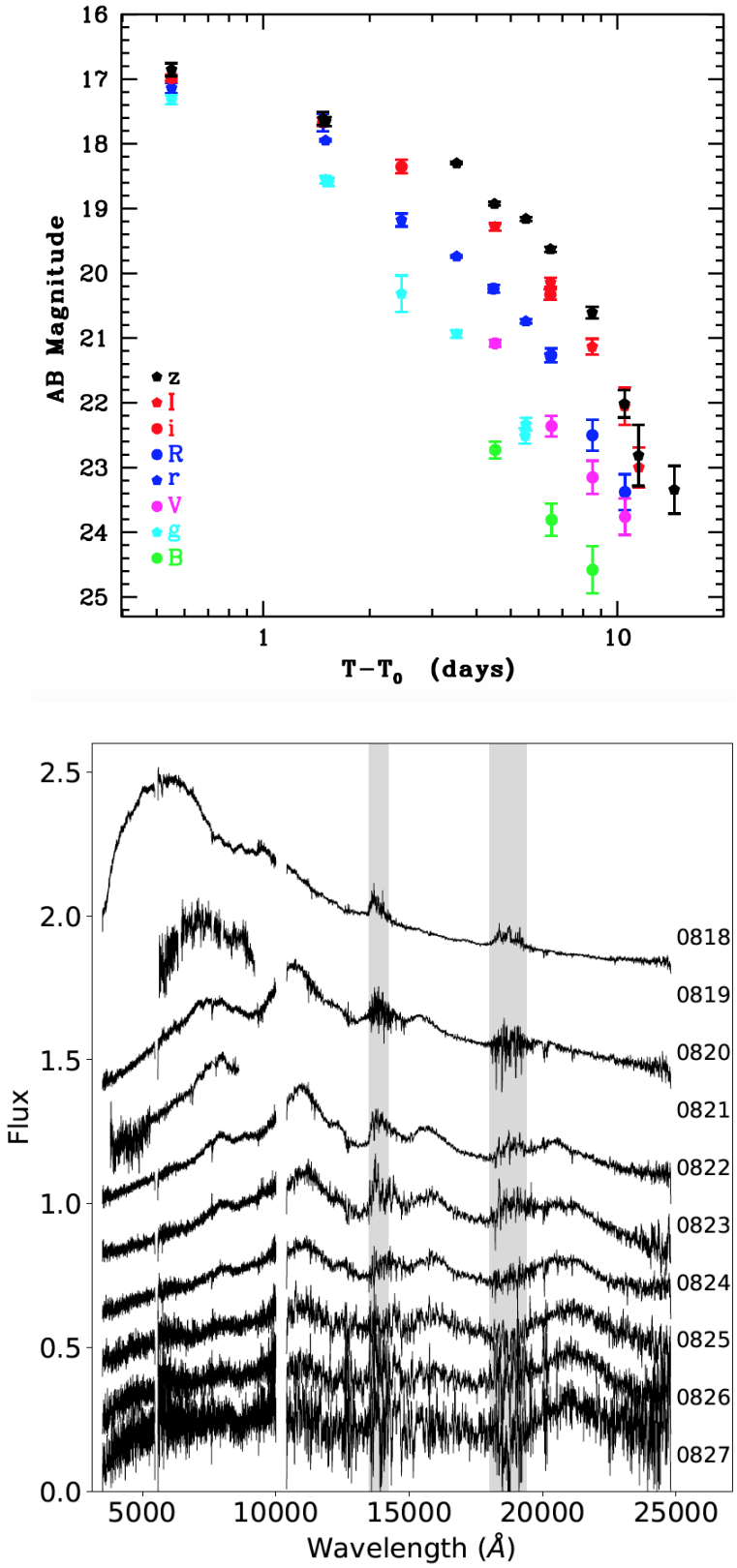

Figure 1.4: Top: AT2017gfo multi-band light-curve. Bottom: Spectral evolution of AT2017gfo from early (top) to late time (bottom). As AT2017gfo is the best sampled optical counterpart of a binary neutron star merger, the dataset is not statistically significant to determine whether the behaviour of this transient is standard or peculiar. Images are from [Pian et al., 2017].

spiral galaxies, which can be TDE or trigs of new AGN phases, as well as supernova explosions in a crowded environments. This is the case of SNhunt133, the focus of this thesis.

CHAPTER

2

TRANSIENTS IN THE CORE OF GALAXIES

As mentioned before, the interest of astronomers towards transient events observed in the core of galaxies has increased in the last few years. In this context, [Kankare et al., 2017] reported the discovery of PS1-10adi, a highly energetic transient hosted in the nucleus of a spiral galaxy. It radiated a total energy $E \sim 2.3 \cdot 10^{52}$ erg in a slowly evolving light-curve and narrow-line spectra for more than 3 years. The profile of the narrow Balmer emission was indicative of electron scattering, with the profile becoming asymmetric at late phases. In particular, a red wing was observed in spectra taken about 200 days from the optical peak. The photometric evolution of the transient was inconsistent with an intrinsic variability of the core of the galaxy, hence it was more likely consistent with a TDE or even a SN explosion in the proximity of the galactic core.
Both a TDE and a SN could produce this phenomenon. This discovery prompted the idea of similar transients classified erroneously as normal AGN in the past. SNhunt133 is another object whose observables have controversial explanations, as it can be interpreted either an the birth of an AGN, or a stellar transient in an hyper-dense region of the host galaxy.
In this chapter, I will detail the physics of AGN (Section 2.1), SN (Section 2.2) and TDE (Section 2.3) phenomena, as well as their major observable characteristic.

2.1 Active Galactic Nuclei: the Unified Model

Active Galactic Nuclei (AGN) show a strong emission in X-ray, a non-stellar UV and optical continuum and prominent emission lines, and a relatively strong radio contribution. Quasars, Type I and II Seyfert galaxies and Blazars are all active galaxies. Quasars are very far and luminous objects with a stellar-like luminosity profile. Seyfert galaxies are spiral galaxies with high central surface brightness, and are subdivided into type I, having both narrow and broad emission lines, and type II with only narrow emission components. Blazars are blue, variable objects lacking spectral lines, often seen in radio. Until the early 90s, with the publication of the *Unified Model* [Antonucci, 1993], all these astronomical sources were considered different phenomena. Now it is universally accepted that all of them are manifestations of the same AGN phenomenon, seen from different viewing angles.
The centre of the galaxy hosts the engine, the supermassive black hole (SMBH, $M > 10^6$ $M_\odot$), which powers the AGN. An accretion disk between 0.01 and 1 pc surrounds the SMBH [Carroll and Ostlie, 2017]. From this region the non-thermal continuous emission originates, and it emits over optical to X-ray domains. The broad line region (BLR) is located outwards. In that region, the gas moves at high velocity due to the SMBH gravitational potential, thus the broadening of the spectral lines is kinetic. The non-thermal continuum from the disk photo-ionises the region, which is $0.01 - 0.1$ pc wide in the case of Seyfert I galaxies, and up to few parsecs for bright quasars [Netzer, 1990]. There are no forbidden lines, thus the density in the region is high. The intensity of the emission is also high, leading to a short recombination time. The BLR is surrounded by a dust torus, which has a thickness larger than the BLR (~ 1 pc), thus if the AGN is seen from a high inclination angle, the BLR can be totally hidden. The torus is not a single entity, but is in fact better modelled with small dusty clouds. Above and below the torus there is the narrow line region (NLR), which gives rise to narrow spectral lines. It is mostly empty, with emission due to small clouds of gas. The line profile is typically asymmetric in the blue, indicating outflows obscuring the far redward side. The NLR is never completely obscured by the torus, since it is more extended, around $100 - 300$ pc [Netzer, 1990]. Occasionally, emission jets can be seen from the polar regions. In Figure 2.1 a schematic representation of an AGN is shown.
From this description, it is clear that Seyfert galaxies are lower luminosity AGN, Type I Seyfert galaxies are face-on AGN, Type II Seyfert galaxies are edge-on AGN, whilst quasars are very far, higher-luminosity AGN, with the nuclear luminosity dominating the rest of the emission. Blazars are AGN seen exactly along the polar axis.

2.1.1 Observational properties and emission models

Although AGN spectra can greatly vary from one object to the other, and even the spectrum of the same object may vary in a short time, there are some universal physical properties. In Figure 2.2 a multi-wavelength spectrum of an AGN is shown.
First of all, the continuum follows a power-law

$$F_\nu = \nu^{-\alpha}$$

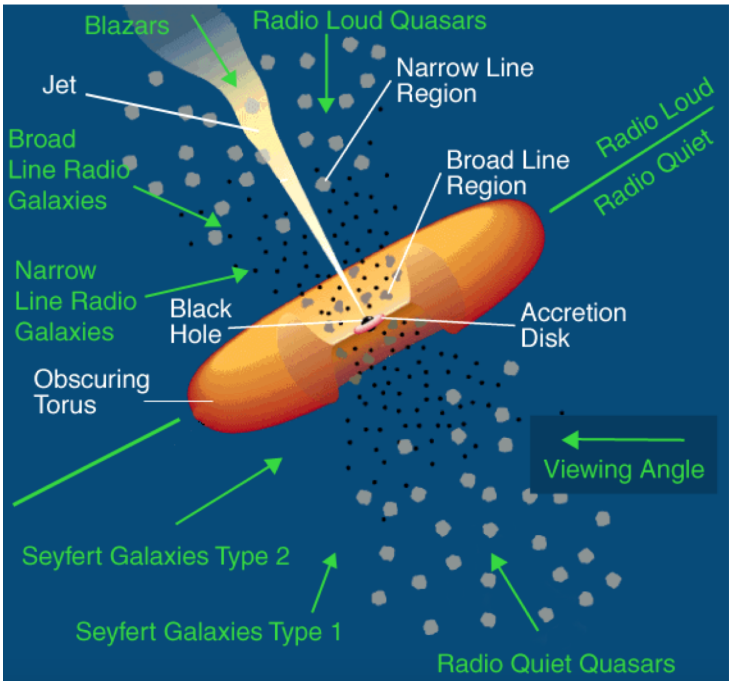

Figure 2.1: Schematic representation of an AGN. The picture is from [Reynolds et al., 2014].

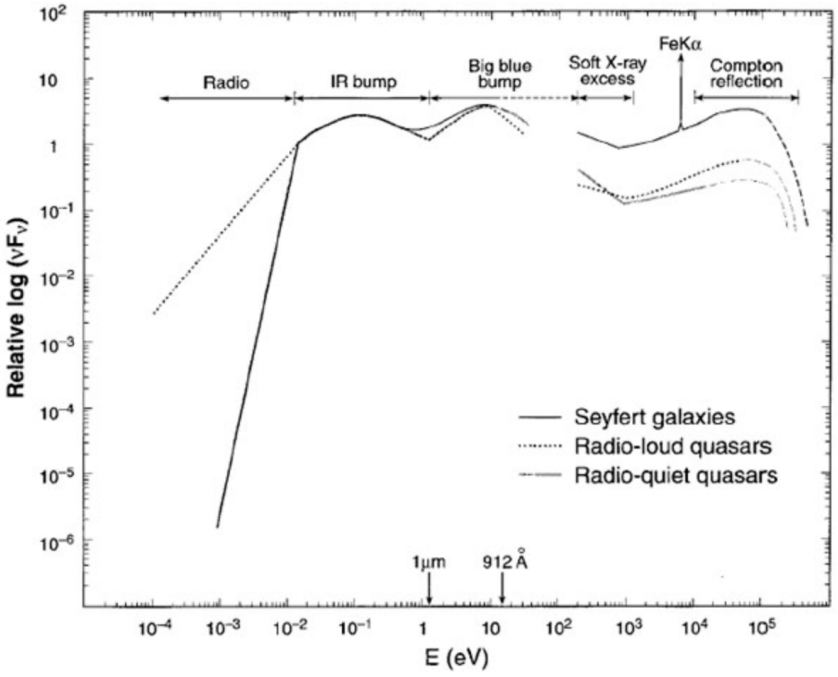

Figure 2.2: Multiband view of AGN emission. The most prominent features are highlighted. The figure is from [Koratkar and Blaes, 1999]

where F_ν is the monochromatic flux at frequency ν and α is the spectral index, usually between 0.5 and 2 and increasing with the frequency [Carroll and Ostlie, 2017].
AGN emission stems from a series of different physical mechanisms at work at different wavelengths. In the following, I will refer to [Risaliti and Elvis, 2004] for a complete review of the spectral characteristics of AGN, and to [Padovani et al., 2017] and a series of lectures by B. M. Peterson [B. M. Peterson, April 2019, Osservatorio Astronomico di Padova] for the specifics of the emission.

Unobscured AGN

A first important distinction to make is whether the AGN is obscured or not. Obscuration in fact hinders several spectral features.

- **Radio:** For unobscured AGN, there is another difference at radio wavelength between radio-quiet (RQ) and radio-loud (RL) AGN. [Baloković et al., 2012] define radio loudness as $R_K = log(L_{rad}) - Klog(L_{opt})$, where L_{rad} is the continuum luminosity at 1.4 GHz, L_{opt} is the continuum optical luminosity and K is a model-dependent parameter. RL AGN show a strong, non-thermal continuum from radio to FIR, whilst RQ AGN have a steep slope in the FIR, corresponding to dust emission and their radio contribution is negligible. For both RQ and RL, the radio spectrum is flat and corresponding to a power-law, indicating synchrotron radiation[1].

- **Infrared:** Unobscured AGN emit nearly 30% of their luminosity at IR wavelengths. The continuum has a minimum between 1 and 2 μm, in correspondence to the sublimation temperature of the dust ($1000 - 2000$ K, depending on the composition). There is a distinct bump at $10 - 30$ μm caused by the thermal emission from the dust torus. In Figure 2.3 the IR spectrum of a typical AGN is shown.
  Dust surrounds the accretion disk outside the BLR, since the inner limit of the torus is set by the sublimation of dust ant the estimated temperatures of the BLR are too high to allow dust survival [Barvainis, 1987]. Also, all lines disappear, indicating that the BLR ends where the dust starts. Dust scatters, absorbs and re-emits light coming from the disk in the IR. Scattering by the material in the throat of the torus induces polarisation. With a spectro-polarimetric analysis, it is also possible to discern that the emission from Seyfert I and II is the same but coming from different angles. The torus is often represented as a compact and uniform structure, but it is more likely to be an ensemble of small, dusty clouds [Elitzur and Shlosman, 2006] (see also the incipit of Section 2.1).

[1] In synchrotron radiation, electrons are subjected to a Lorentz force by the magnetic field $\vec{F} = q(\vec{E} + \vec{v} \times \vec{B})$, where q is the electron charge, $\vec{E}$ is the electric field, $\vec{v}$ is the velocity of the electron and $\vec{B}$ is the magnetic field. The interaction forces the electrons to move in helicoidal orbits around the magnetic field force lines. Since electrons are relativistic, the emission is channelled in a restricted cone with aperture $\gamma = \frac{1}{\sqrt{1-v^2/c^2}}$, where c is obviously the speed of light.

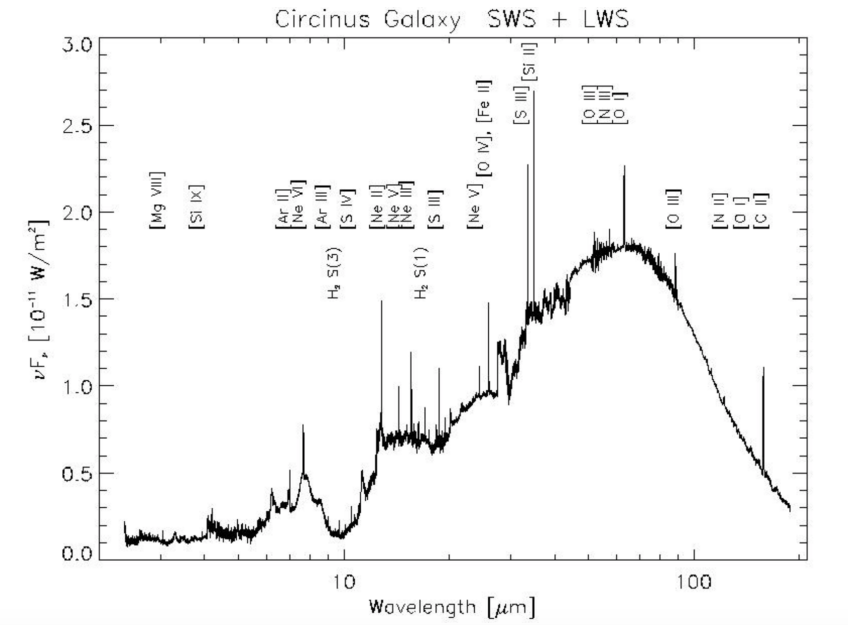

Figure 2.3: Typical IR spectrum of an AGN, with the distinct peak due to dust. The picture is from [Moorwood, 1999].

- **UV and visible light:** At optical and UV wavelengths, the principal feature is the blue bump. Around the peak, the spectrum has a power-law shape. In fact, between 300 and 5000 Å the continuum can be modelled with two power-laws, one between 300 and 1300 Å with slope $\alpha = -1.76$ and the other from 1300 to 5000 Å with slope $\alpha = -0.44$. Afterwards, the galactic emission flattens the spectrum [Vanden Berk et al., 2001]. In the optical/UV range permitted broad ($2000 - 15000$ km/s) lines are found, along with much narrower ($300 - 800$ km/s) forbidden emission features. There can also be a smaller bump at wavelengths longer than Hβ, due to FeII lines and Balmer lines recombination continuum [Wills et al., 1985]. In Figure 2.4, a typical broad-lined AGN spectrum is shown.

  The UV/optical thermal emission of the continuum is generally attributed to the accretion disk. The luminosity of the spheroidal component of a galaxy correlates with the mass of the central BH [Marconi and Hunt, 2003], and thus with its Eddington limit. It follows then that the luminosity ratio between the AGN and the host galaxy L_{AGN}/L_{host} at each wavelength depends on the Eddington limit of the AGN.
  For a source to vary, it must be smaller than the light travel time associated to the variation, otherwise a variation cannot be observed from Earth. The only source small enough to support the rapid variation, but massive enough to provide the registered luminosity, is a SMBH. The mass accretion onto it releases gravitational potential, which ultimately generates energy. A SMBH with $M > 10^6$ $M_\odot$ satisfies the Eddington limit, assuming it has an average luminosity of 10^{44} erg/s, which is typical for a Seyfert galaxy. Infalling material produces angular momentum, which explains the formation of an accretion disk. Matter

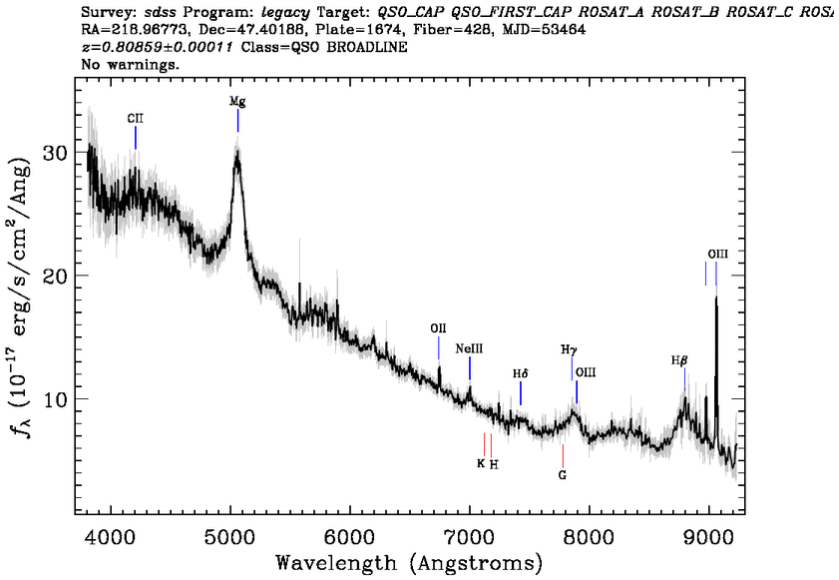

Figure 2.4: Typical spectroscopic optical emission of a broad-line AGN. The picture is from [Baldini, 2015].

spiralling onto the SMBH through the accretion disk has its kinetic energy converted in heat and radiation because of viscosity. The generated luminosity can vary, depending on the efficiency of the conversion, which ultimately depends on the characteristics of the SMBH, as

$$L_{acc} = \eta \dot{M} c^2$$

where $0.0572 \leq \eta \leq 0.423$ is the efficiency of the process and $\dot{M}$ is the mass accretion rate necessary to sustain the measured luminosity [Carroll and Ostlie, 2017]. The Eddington ratio is defined as

$$\dot{m} = \frac{\dot{M}}{\dot{M}_{Edd}}$$

with $\dot{M}_{Edd}$ being the mass accretion rate to sustain the Eddington luminosity. With a value $\dot{m} < 0.01$ accretion is radiatively inefficient, whilst a typical quasar has $\dot{m} \sim 0.1$. Taking energy conservation into account, and if we suppose the disk to be optically thick but geometrically thin,

$$L = \frac{GM_{BH}\dot{M}}{2r} = 2\pi r^2 \sigma T^4$$

where L is the luminosity, M_{BH} is the black hole mass, r is the dimension of the disk, σ is the Stefan-Boltzmann constant and T is the temperature. Thus the accretion disk has an effective temperature

$$T(r) = \left(\frac{GM_{BH}\dot{M}}{4\pi\sigma r^3} \right)^{\frac{1}{4}}$$

In the BLR, measured velocities span $1000 \leq FWHM \leq 25000$ km/s, where $FWHM$ is the full-width measured at half-maximum of the line. Spectra are typical of photo-ionised gas at $\sim 10^4$ K. Emission lines are only permitted, both of low and high ionisation levels. It is impossible to fit them with a single cloud model and the energy of the continuum is insufficient to power the most luminous lines [Ferland and Mushotzky, 1982], thus a model composed of multiple clouds (although there is no trace of small-scale structure in the line profiles [Arav et al., 1998]) and a disk-generated wind has been proposed.
AGN of different luminosity show similar spectra, so it is likely that the BLR has similar conditions in all AGN. With the technique of reverberation mapping, a relation R-L was found between the size of the BLR and the luminosity of the Hβ line, with a slope of 0.55 ± 0.03 [Bentz et al., 2013].
The NLR has measured velocities of $200 \leq FWHM \leq 1000$ km/s. In near AGN, the NLR is actually resolvable is "ionisation cones" [Falcke et al., 1998]. Spectra have forbidden high ionisation lines, from which it is possible to measure density and temperature of the region. The FWHM correlates with the critical density (in fact, gas at critical density emits more efficiently) and with the excitation potential. Measures are consistent with high density and excitation potential closer to the accretion disk, where the gravitational potential is deeper.
The NLR is dense and compact, at least in some AGN. The characteristic blueward asymmetry in higher ionisation lines of type I Seyfert galaxies corresponds to material outflow [Leighly et al., 2001]. Thus, the wind must have a strong radial component [Vestergaard et al., 2000]. Also the absorption in X and UV is blueshifted relatively to systemic. Along with large column density, multiple velocity components and broad absorption lines found in quasars, they are all indicators of outflow (e.g. [Hamann et al., 2018]). A visual representation can be seen in Figure 2.5.

- **High frequency radiation:** In the X-rays, observed emission goes from the Galactic cut-off at 0.1 keV up to 300 keV. There is a primary component in the shape of a power-law, which is found from 1 to 100 keV and more. Another rather strong component is the soft X-ray emission around $0.2 - 1$ keV. Many AGN show a distinct absorption at these wavelengths, indicating the presence of a warm, ionised reflector in the central regions. To be held accountable of the absorption, the gas has to have a column density of $N_H \sim 10^{21} - 10^{23}$ cm^{-2}. Lastly, another recurrent feature is the Fe K line at 6.4 keV.
  Emission in the X-rays is due to physical processes in the inner disk. There is no self-consistent model of the innermost region of an AGN, but it is theorised that the SMBH is surrounded by a corona emitting X-rays ($T_e \sim 10^9$ K), a part of which is reflected on the disk, and jets are emitted from the BH. The disk can Compton-scatter photons up until the high energy cut-off, at 50 keV. At each scatter, the photons lose energy and move towards lower frequencies. This gives a power-law shape [Done, 2010] which leads to absorption fluorescence in atomic lines, especially Fe Kα at 6.4 keV. Above 50 keV, photons are only reflected. The soft X-ray excess is attributed to the Compton Wien tail of the accretion disk (only for AGN of smaller mass and higher accretion rate [Ponti et al., 2010]) or to

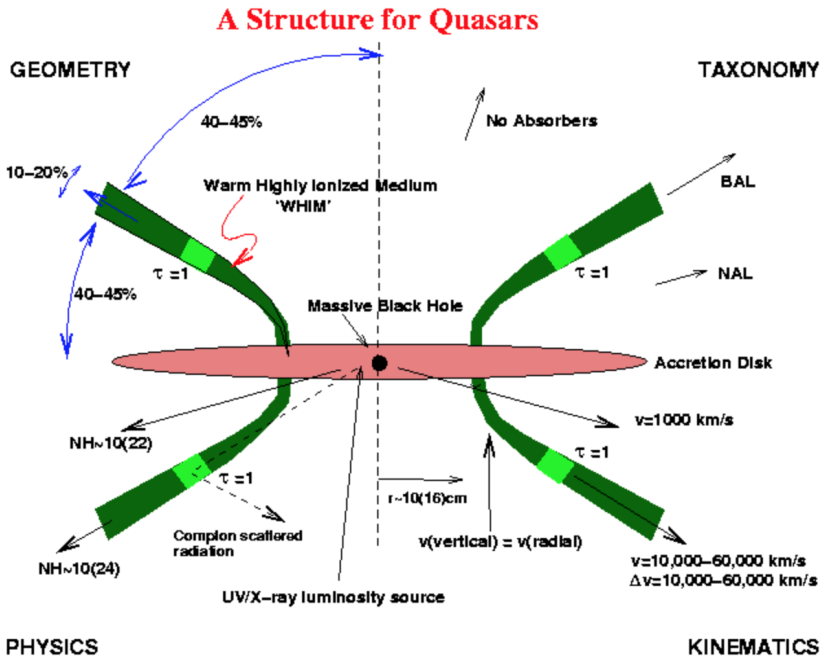

Figure 2.5: Model of AGN structure comprehensive of gas and wind. The picture is from [Elvis, 2000].

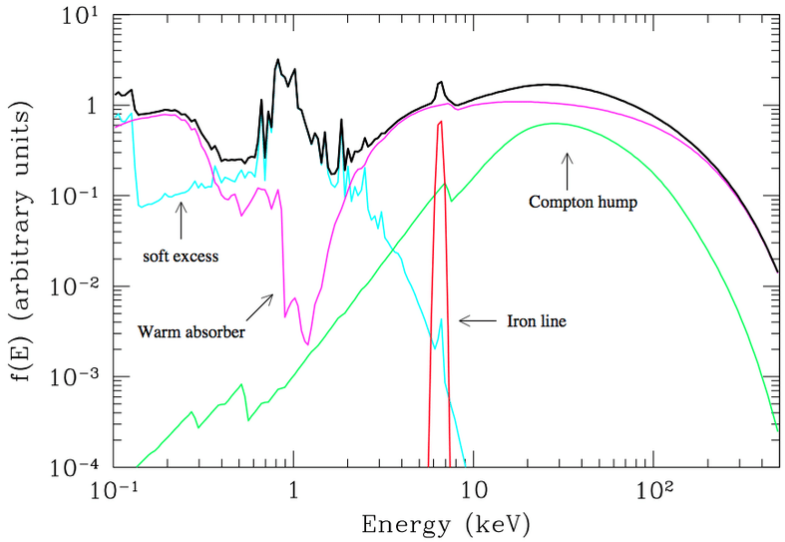

Figure 2.6: The typical AGN X-ray emission is plotted in black; other colours represent the different components of the emission. The soft X-ray excess is represented in blue, the synchrotron power-law, absorbed by warm gas, in pink, the Fe Kα line in orange, the Compton hump in green. The picture is from [Risaliti and Elvis, 2004].

partially ionised absorption [Gierliński and Done, 2004], whilst some variations may be due to occultation from gas clouds [Risaliti, 2010].
Only jetted AGN emit γ-rays. Blazars are thus the predominant sources in the gamma sky. Their spectral energy distribution (SED) covers the whole spectrum and it shows a characteristic "double-hump" in the νF_ν vs. ν plane, as can be seen in Figure 2.7.

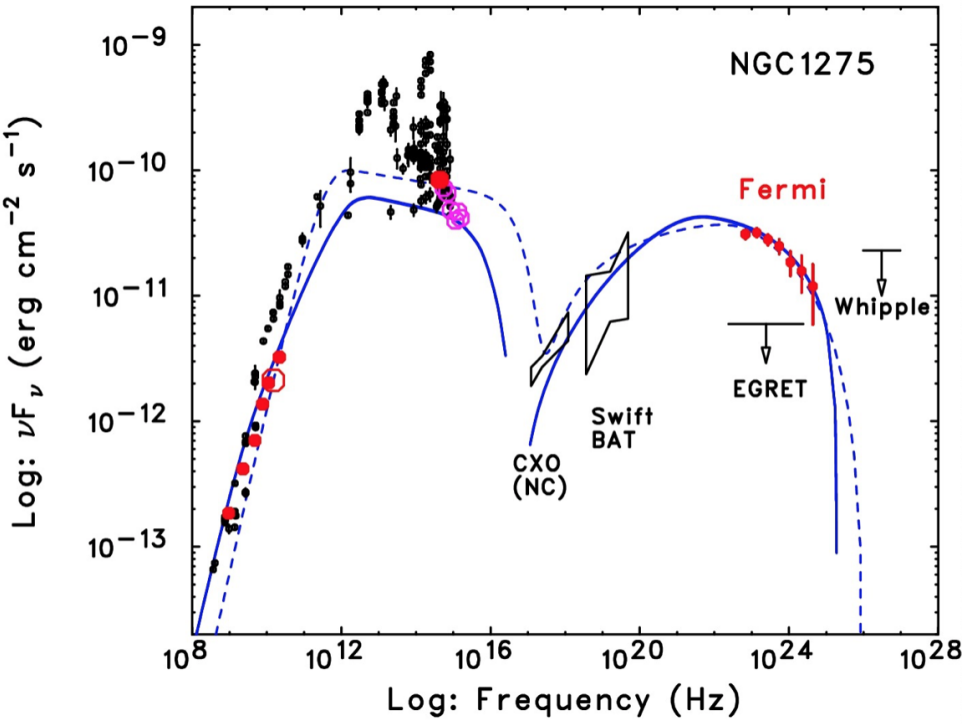

Figure 2.7: Multiband (from radio to γ-rays) SED of NGC 1275, with the characteristic double hump. NGC 1275 is a giant elliptical galaxy, host of the bright radio source Perseus A (3C 84). Fit with synchrotron model (dashed line) and decelerating flow model (solid line) are also shown. The figure is from [Abdo et al., 2009].

Obscured AGN

As a major difefrence from unobscured AGN, obscured AGN have negligible radio luminosity. Free-free processes [Neufeld et al., 1994] and HI emission [Véron-Cetty et al., 2000] can absorb and alter the shape of the continuum.
Whilst the UV flux is also affected by line absorption from the NLR and BLR, the UV-to-NIR is affected by dust absorption and re-emission at longer wavelengths. Emission lines, including H I and forbidden lines of O, N, Ne and Ar, are narrow ($300 - 800$ km/s). If Kepler motions explain the line width, the emitting gas is more distant from the centre than that responsible for the BLR. The ratio of high ionisation lines, such as [OIII] at 5007 Å, with respect to Hα and Hβ is higher than in starburst galaxies, which allows to distinguish the two phenomena even in

cases of severe absorption. As we will see later, this method is relevant for characterising the host of SNhunt133.
The X-ray region of the continuum is obscured by photoelectric absorption from dust and gas at energies below 3 keV. At higher energies, the main responsible for absorption is the Compton scatter. Here, the only source of opacity is Thompson scattering, thus $\tau = N_H \sigma_e$, with τ optical depth, N_H column density and σ_e Thompson cross-section. The denser the gas, the more portion of light is absorbed. When the column density exceeds 10^{24} cm^{-2}, the medium becomes Compton-thick and only the Fe K line and a reflected continuum are seen.

2.1.2 AGN variability

The main characteristic of AGN is their variability. Their flux varies irregularly and aperiodically, with timescales ranging from minutes to years. The variation is usually quantified through the power spectral density, which is the Fourier transform of the convolution of the light-curve with its complex conjugate. It is $P(f) = f^{-\alpha}$, with the spectral index $1 \leq \alpha \leq 2.5$ that depends on the observation band [Uttley et al., 2002]. The minimum timescale of the variability gives an estimate of the linear dimension of the emitting part of the source [Terrell, 1967]. Variations are faster in the X-ray region than at optical wavelengths, with the X-ray emission showing large variations from minutes to hours. They are thought to be originated by the corona and the inner disk, and they drive the variability of the outer disk that is seen in the UV/optical range. In fact, signals from variation are delayed at different wavelengths, providing researchers with insight on the inner structure of the AGN through reverberation-mapping.
Signals between 1158 and 9163 Å are delayed with respect to shorter wavelengths [Fausnaugh et al., 2016]. Moreover, in general soft X-rays follow hard X-rays at higher frequency, as expected from the fact that higher energies are driving everything radially, but at lower frequencies there are hard lags of hard X-rays behind soft X-ray. This could be interpreted as some kind of signal going from the outer to the inner disk, probably a property of the accretion.
The near-IR continuum variation follows the UV/optical variation with a longer time-delay, consistent with a dust sublimation radius [Suganuma et al., 2006].
At gamma frequencies, the observed variability is the variability of the jets, but jets can also contribute to variability with either particles or shocks [Marscher and Gear, 1985].
Observations of Cyg X-1 showed that there exist a scaling relation between the RMS of the power spectrum and the flux [Uttley and McHardy, 2001]. This indicates that, at least in the X-ray domain, the amplitude of the variability correlates with the flux, thus more luminous AGN tend to have larger variability. Therefore, the process is multiplicative and X-ray variations with longer timescales are in control of variations at smaller timescales [Uttley et al., 2005]. This would mean than, in contrast with previous beliefs, the variability does not arise from flares or active regions, but rather from propagating fluctuations. Standing to Lyubarskii's model [Lyubarskii, 1997], local perturbations of the disk parameters can affect the variation rate. If these perturbations have a timescale longer than the time for radial diffusion, they can propagate in the inner regions, joining those produced at smaller radii. When they reach the innermost regions, the energy is liberated and the variation is detectable [Churazov et al., 2001], [Hogg and Reynolds, 2016].

SNhunt133 may be a brightening of a new AGN phase in NGC 6315. In order to understand that, a scrupulous analysis of its emission lines will be needed.

2.2 Supernovae

I will now investigate more thoroughly the physical processes that lead to a supernova explosion and their effects on a high density environment. This review is based on [Carroll and Ostlie, 2017] and [Branch and Wheeler, 2017].

2.2.1 Core-collapse Supernovae

A typical type II SN releases about 10^{46} J in energy, about 1% in kinetic energy and less than 0.01% in photons. The rest is used up by neutrinos. SNe Ib and Ic produce the same amount of energy on average.
Stars with initial mass $M \geq 8\ M_{\odot}$ can efficiently burn carbon and oxygen. The He-burning shell adds its ashes to the C-O core which contracts until C-burning initiates, producing ${}^{16}_{8}\mathrm{O}$, ${}^{20}_{10}\mathrm{Ne}$, ${}^{23}_{11}\mathrm{Mg}$ and ${}^{24}_{12}\mathrm{Mg}$ [Carroll and Ostlie, 2017]. Supposing that each reaction of this series reaches an equilibrium, the evolved star will have an "onion-like" structure, as shown in Figure 2.8.
In fact, at the end of the C-burning phase, a O-Ne core will be generated, O-burning in turn

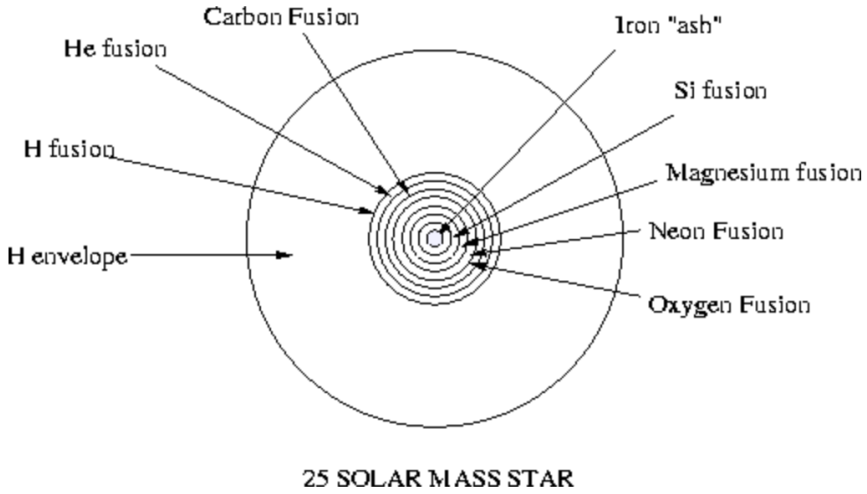

Figure 2.8: Onion-like structure of a pre-supernova-collapse massive star. Different burning envelopes can be seen. Ashes from an envelope accumulate on interior layers. The picture is from http://www.ucolick.org/∼bolte/AY4_00/week8/massive_stars.html.

will initiate and generate a ${}^{28}_{14}\mathrm{Si}$ core. At T$\sim 3 \cdot 10^9$ K, Si-burning can ensue:

$$ {}^{28}_{14}\mathrm{Si} + {}^{4}_{2}\mathrm{He} \leftrightarrow 32_{16}\mathrm{S} + \gamma,\ {}^{32}_{16}\mathrm{S} + {}^{4}_{2}\mathrm{He} \leftrightarrow 36_{16}\mathrm{Ar} + \gamma,\ \ldots,\ {}^{52}_{24}\mathrm{Cr} + {}^{4}_{2}\mathrm{He} \leftrightarrow 56_{28}\mathrm{Ni} + \gamma $$

The chain of reactions produces a series of nuclei close to the binding energy peak of $^{56}_{26}$Fe, especially $^{54}_{26}$Fe, $^{56}_{26}$Fe and $^{56}_{28}$Ni. The result is a core made primarily of iron. Since with each burning the produced energy decreases, the timescale of each burning is shorter than the former one (from $10^6 - 10^7$ years for H-burning, to $2 - 6$ days for Si-burning) [Carroll and Ostlie, 2017].
A combination of photodisintegration and electron-capture is at the base of core-collapse SNe. With the high temperature in the nucleus, photons produced during the Si-burning have enough energy to destroy nuclei via *photodisintegration*. In particular, $^{56}_{26}\mathrm{Fe} + \gamma \rightarrow 13^4_2\mathrm{He} + 4\mathrm{n}$ and $^4_2\mathrm{He} + \gamma \rightarrow 2\mathrm{p}^+ + 2\mathrm{n}$. Photodisintegration destroys the nuclei of heavier elements and it is an endothermic process, therefore thermal energy is removed from the gas which gave the necessary pressure to support the core. Moreover, with the high temperature and density in the core, free electrons that helped sustaining the star through degeneracy pressure are captured by protons and nuclei. This produces neutrinos that carry energy away (e.g. $\mathrm{p}^+ + \mathrm{e}^- \rightarrow \mathrm{n} + \nu_e$) [Carroll and Ostlie, 2017]. With photodisintegration and electron-capture, the core is no longer sustained by electron-pressure, hence it collapses.
The density (and the mass) distribution is conserved and the collapse is homologous (that is, *M(x)*, $x = r/r_0$, is constant) and each mass point has a constant velocity, $r(M) = v(M)t$, so that $v \propto r$ and then *M(x)*, $\rho(x) \propto t^3$ [Branch and Wheeler, 2017]. The structure in homologous collapse maintains the same profiles of density and pressure without modifying the binding energy [Goldreich and Weber, 1980], [Yahil, 1983]. In the beginning, the material is transparent to neutrinos, but then it becomes thick as density increases and neutrinos are blocked when the timescale for neutrino diffusion is equal to the free-fall timescale. For typical values, this happens at $\rho \sim 10^{12}$ g cm^{-3} [Bethe, 1990]. A proofs of neutrino trapping are the low energy and long decline of 1987A. In fact, if neutrinos escaped, energies would be higher and the decline timescale shorter [Burrows, 2013].
The Chandrasekhar mass is $M_{Ch} = 5.76 < Y_e >^2 \mathrm{M}_\odot$, where Y_e is the number of electrons per barion. In order for the collapse to start in the iron core, it must be $Y_e \simeq 0.42$, so that $M_{Ch} \simeq 1.0$ $\mathrm{M}_\odot$. The typical core mass is 1.5 $\mathrm{M}_\odot$, so it exceeds the Chandrasekhar mass and thus it is not dominated by degeneracy pressure. The mass of the homologous core is $M_{Ch}(Y_{e,trap}) \simeq 0.6 - 0.8$ $\mathrm{M}_\odot < M_{core}$. At the surface of the neutrino trapping, $Y_e \simeq 0.35 \Rightarrow M_{Ch} \simeq 0.7$ $\mathrm{M}_\odot$. There, the portion of the core within M_{Ch} undergoes a homologous collapse. With $v \propto r$, there exists a certain radius at which the inward flux becomes supersonic. At greater radii, pressure waves cannot propagate to balance the pressure gradient and the material is in free-fall, with $v \propto r^{-\frac{1}{2}}$ and $M(r) \sim$ constant. This means there is a maximum infall velocity where $v \propto r^{-\frac{1}{2}}$ and $v \propto r$ meet [Branch and Wheeler, 2017]. In this point, the inner core is decoupled from the supersonic outer core. The collapse is too fast to transmit mechanical information at the speed of sound to the outer core, thus the outer core remains almost suspended above the collapsing core. When the core exceeds the critical density of $\rho_c \simeq 2\rho_{nuc} \simeq 6 \cdot 10^{14}$ g/cm^3, the strong force changes from attractive to repulsive under the Pauli exclusion principle [Branch and Wheeler, 2017]. Nuclear density is reached, the homologous collapse halts and a gas of degenerate nucleons forms. The nuclear equation of state stiffens and hence the pressure rises, steeply. This in turn increases the density, generating a steep pressure gradient. Supersonic material in free-fall falls on the low-speed material in homologous collapse, creating a shock, at $0.4 - 0.6$ $\mathrm{M}_\odot$ [Janka, 2012]. The inner core overshoots and overcompresses, then it rebounds and sends the shock outward.

The shock wave meets the outer material and the high temperature causes photodisintegration. This is not enough to eject the outer layers because it is depleted by the initial momentum of the free-falling material and by the energy used to dissociate the infalling iron [Bethe, 1990]. About 1 $M_\odot$ of Fe is disintegrated into He. The shock loses energy and it becomes quasi-stationary. The failed bounce produces an *accretion shock*, and the infalling material starts accreting on its surface. It stalls at $2 \cdot 10^7$ cm, where the pressure of the post-shock balances the pressure of the infall. Mass accumulates there and the density grows to $\rho > 10^{11}$ g/cm^3. From photodisintegration, electron-capture and pair annihilation of $e^+ - e^-$, a neutrino shell is generated underneath the surface of the shock. The material is dense and neutrinos cannot escape, so they deposit energy on the material behind the shock, heating it to a point when the the shock can proceed. If the deposition is not fast enough, the material falls back on the core and there is no explosion. Instead, the post-shock pressure can decrease and the shock proceeds backward to a NS surface. [Branch and Wheeler, 2017]
If the shock resumes, at the reprise of the shock propagation the kinetic energy is 10^{44} J, 1% of the energy liberated by neutrinos. At R$\sim 10^{13}$ m $\sim$ 100 AU, it becomes optically thin and the display of 10^{42} J in photons can be seen [Carroll and Ostlie, 2017].
The plateau displayed in type II-P SN light-curves (shown in Figure 2.9) comes from the energy deposited by the shock on the H-rich envelope. The shock also ionises the gas, thus recombination processes release energy at an almost constant temperature of $\sim$ 5000 K. The shock produces $^{56}_{28}$Ni which can deposit radioactive-decay energy on the envelope to support the plateau. Other by-products of the shock are $^{57}_{27}$Co, $^{22}_{11}$Na, $^{44}_{22}$Ti, and each radioactive element can contribute to the light-curve, whose decline rates change accordingly [Carroll and Ostlie, 2017]. Differences among SN classes can be reduced to composition and mass of the envelope at collapse and quantity of radioactive materials synthesised in the ejecta, but the physical mechanism of the explosion is the same.
$^{56}_{28}$Ni undergoes beta-decay ($^{56}_{28}\text{Ni} \rightarrow^{56}_{27}\text{Co} + e^+ + \nu_e + \gamma$). Radioactive isotopes decay as

$$N(t) = N_0 e^{-\lambda t}$$

where *N(t)* is the number of isotopes at time t, N_0 is the initial number of isotopes and $\lambda = \frac{ln2}{\tau_{1,2}}$, $\tau_{1,2}$ time of nuclear half-life. The rate of energy deposition is proportional to

$$\frac{dN}{dt} = -\lambda N$$

thus the slope of the bolometric light-curve is

$$\frac{dlogL}{dt} = -0.434\lambda \quad \text{or} \quad \frac{dM_{bol}}{dt} = 1.086\lambda$$

so measuring the slope of the light-curve provides an estimate of the abundance of isotopes [Carroll and Ostlie, 2017].
In Figure 2.9, spectra and light-curves of the major SN subtypes are shown.

2.2.2 Thermonuclear Supernovae

Type Ia SNe have very homogeneous absolute peak magnitudes [Taubenberger, 2017], with $< M_B > \simeq < M_V > \simeq -19.3 \pm 0.3$. The spectra show no trace of H, whilst they are characterised

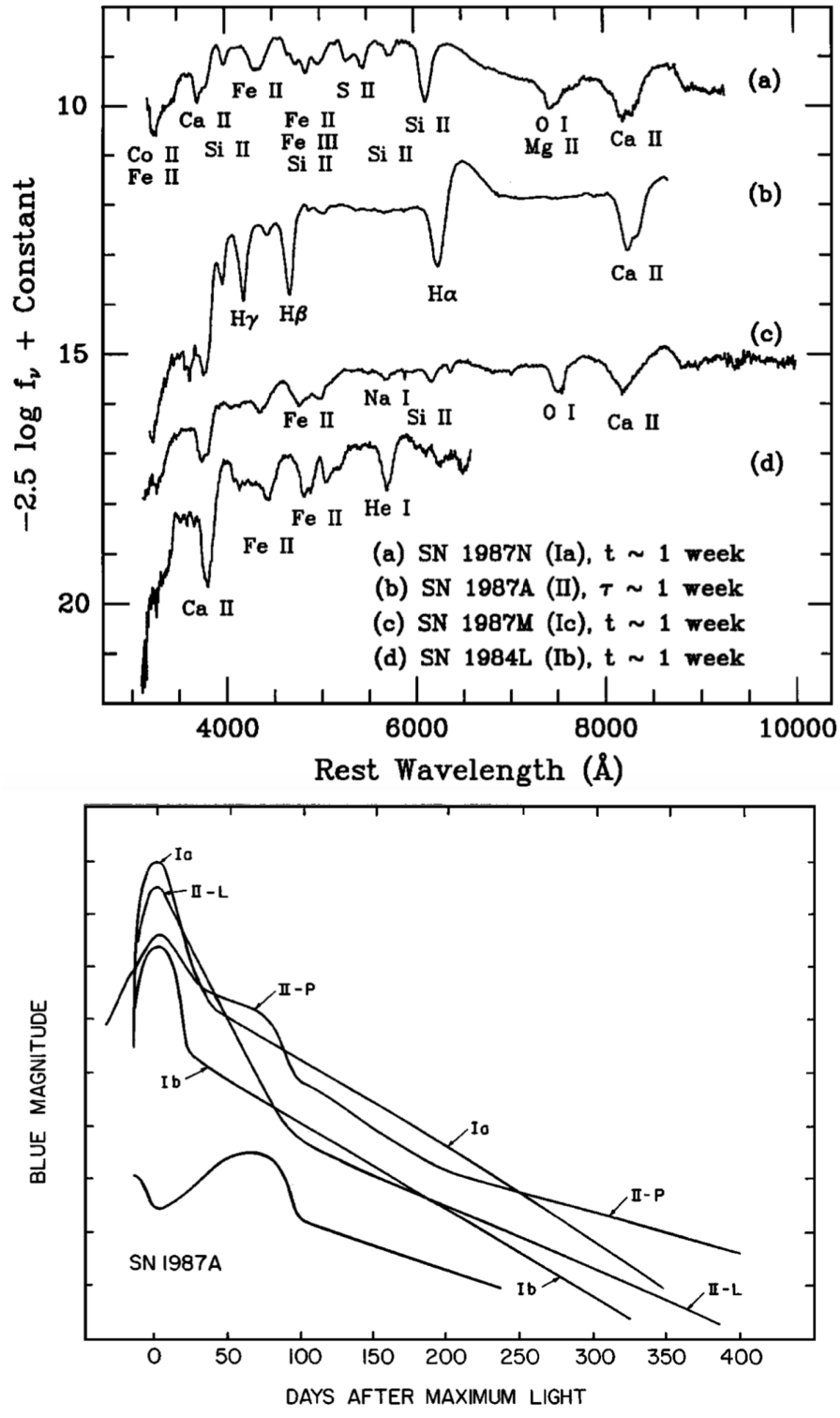

Figure 2.9: Top: Early prototype spectra of the four major SN subtypes, Ia, Ib, Ic and II. t is the time after maximum light, whereas τ is the time after core-collapse. The main absorption lines are highlighted on the plot. Bottom: Schematic light-curve of the major SN subtypes and SN 1987A. Type II SNe are distinguished in II-P and II-L, whilst type Ib and Ic are averaged in a single light-curve labelled "Ib". Both pictures are from [Filippenko, 1997].

by Si II and lines of O I, Mg I, S II, Ca II, Fe II and Fe III. The blueshifted absorption features indicate ejecta velocities $\gtrsim 10^4$ km/s at peak. The mechanism is the thermonuclear explosion of a WD which accreted its mass to reach the Chandrasekhar limit. There are two plausible explosion mechanisms: (1) **double degenerate** and (2) **single degenerate**.
In the double degenerate model, two WDs orbit each other, emitting gravitational waves. The WD with the bigger radius (that is to say, the less massive) ultimately passes the Roche lobe. Its C-O rich material sets in a thick disk around the primary WD, accreting its mass. When it grows closer to the Chandrasekhar limit, thermonuclear reactions start in the interior of the WD, disrupting it. This scenario can successfully explain the rate of observed SNe Ia and the lack of H and of a surviving companion [Carroll and Ostlie, 2017]. In the single degenerate model, a non-degenerate (hence, a main sequence star or a red sub/giant) star orbits a WD accreting its mass, much like with novae. The key distinction is that in this case the accreted mass gives the complete disruption of the WD, due to different accretion rates than novae [Carroll and Ostlie, 2017]. In the single degenerate scenario C ignites in a degenerate WD in hydrostatic equilibrium, when the rate of C-burning is higher than the local neutrino loss rate [Arnett, 1969], [Barkat, 1975]. The ignition happens at $\rho_c \simeq 3 \cdot 10^9$ g/cm^3. The burning rate is initially modest to then increase as the temperature gradient becomes super-adiabatic, initiating convection. This is the *smoldering phase*, which sets the conditions for the dynamical runaway, deciding where, how many and when spots of dynamical burning will start [Branch and Wheeler, 2017]. During the smoldering phase, ^{12}C is concerted in heavier nuclei which will determine the composition at explosion. Furthermore, electron-capture contributes to control abundances. This will have a bearing on the quantity of ^{56}Ni that supports the light-curve [Brachwitz et al., 2000], [Höflich et al., 2004]. Smoldering is also associated with convective Urca-process[2] [Paczyński, 1972]. Convection brings electron-capture and then β-decay. The composition remains unaltered, but neutrinos and anti-neutrinos are lost. This loses energy but temperature and entropy do not decrease; the Urca-process in fact slows down convective currents and reduces the rate of entropy increase associated with the injection of nuclear energy. In other words, Urca-process changes the rate of increase in nuclear burning [Branch and Wheeler, 2017].
In the single degenerate scenario, the process that leads to C-burning continues after the ignition. The central mass and density increase, as well as temperature, due to adiabatic compression [Branch and Wheeler, 2017].
In both scenarios, moreover, it is still unclear whether the C-O burning takes place at subsonic speed (*deflagration*) or if the front accelerates to supersonic speed (*detonation*), which leads to a real explosion. From this distinction depend details of the light-curve, like the maximum luminosity, the speed of the decay and the abundances of synthesised elements [Carroll and Ostlie, 2017] (an example of SN Ia light-curve is shown in Figure 2.9).
With deflagration, since the nuclear burning can be faster than the dynamical timescale, the burning is faster than the dynamical response. It propagates and can act as a piston to accelerate the material until the fronts of the shock, leading to detonation [Branch and Wheeler, 2017]. The basic properties of deflagration and detonation are described by the equations of fluidodynamics expressed in steady-state Chapman-Jouguet solutions (see for example [Khokhlov, 1991] and [Khokhlov et al., 1997]). Their nature depends on metallicity, mass of the WD, density at

[2]It is a process of neutrino production that supposedly cools the gas of the WD.

ignition, rotation and magnetic fields.
The explosion of the WD expands the material, bringing a strong adiabatic cooling. Temperature and opacity are very low in this phase, often referred to as *Dark Time*. There is about a day between the breakout emission and the start of the rise to maximum light by deposition of radioactive energy decay [Branch and Wheeler, 2017].
It is argued that explosions can happen also at sub-Chandrasekhar mass if they are triggered by detonation of a He-shell. In this case, $\rho_{WD} > 10^9$ g/cm^3. Super-Chandrasekhar explosions are also theorised, with a violent merging between two WDs with total mass > 1.4 M$_\odot$.

SNhunt133 may be a SN explosion in the crowed environment of a galactic core. The analysis of its light-curve and spectral evolution, as well as the comparison with other known SNe, will be crucial in the characterisation of SNhunt133.

2.3 Tidal Disruption Events

Another possible explanation for transients observed in the nucleus of galaxies is they are TDEs. TDEs have been theorised for more than 30 years [Rees, 1988], but they have been observed at optical and radio wavelengths only in the last decade (e.g. [Gezari et al., 2012], [van Velzen et al., 2016]). Some debris are ejected at high speed, whilst the rest is swallowed by the BH, causing a luminous flare which can last for years [Rees, 1988].
TDEs are very diverse, their spectra can have H, or He, or N [Leloudas et al., 2019] and it likely depends on how the UV and X luminosity of the accretion is reprocessed. The absolute peak magnitude spans a wide range, $-21 \lesssim M_R \lesssim -19$ [Arcavi et al., 2014], and the light-curve is well fitted with a $t^{-\frac{5}{3}}$ decay. It is still unclear what powers the optical emission, and whether it is due to debris collision, disk winds, or reprocessing of accretion luminosity [Jiang et al., 2016].
A few TDEs are only observable in the IR [Mattila et al., 2018], as they are believed to come from dust-surrounded transients in luminous IR galaxies. Overall, observed rates are lower than predicted ones.
A TDE could be a viable explanation of SNhunt133, since the transient was hosted in the nucleus of a spiral galaxy.

2.3.1 Spectro-photometric characteristics

A TDE displays a luminous accretion flare at $T_{BB} \sim 10^5$ K [Rees, 1988], [Evans and Kochanek, 1989]. Several parameters characterise the observational properties: impact parameters, mass, age, composition, evolutionary stage and spin of the disrupted star, stellar demographics, fraction of accelerated material, accretion geometry, mass and spin of the BH [Hinkle et al., 2020].
The UV/optical SED of a TDE is well-fitted with a black-body. The black-body radius r_{BB} increases until the light-curve reaches the maximum, then declines monotonically. Whilst the temperature is a heterogeneous parameter in TDEs, in each object it remains nearly constant with time, with only a minor rise at late phases [Holoien et al., 2019], [van Velzen et al., 2020]. UV/optical TDEs in the sample of [Hinkle et al., 2020] have temperatures in the

range $20000 - 50000$ K. Multiple peaks in an otherwise smooth evolution can indicate collision shocks due to debris [Gezari et al., 2017] or reprocessing of X-ray emission from the accretion disk [Wevers et al., 2019a], [Leloudas et al., 2019].
As an example, Figure 2.10 shows the light-curve of the TDE AT2017eqx, whereas in Figure 2.11 its spectroscopic evolution and SED are plotted.

TDEs have a persistent blue colour, a longer rise time than canonical SNe, and a smooth,

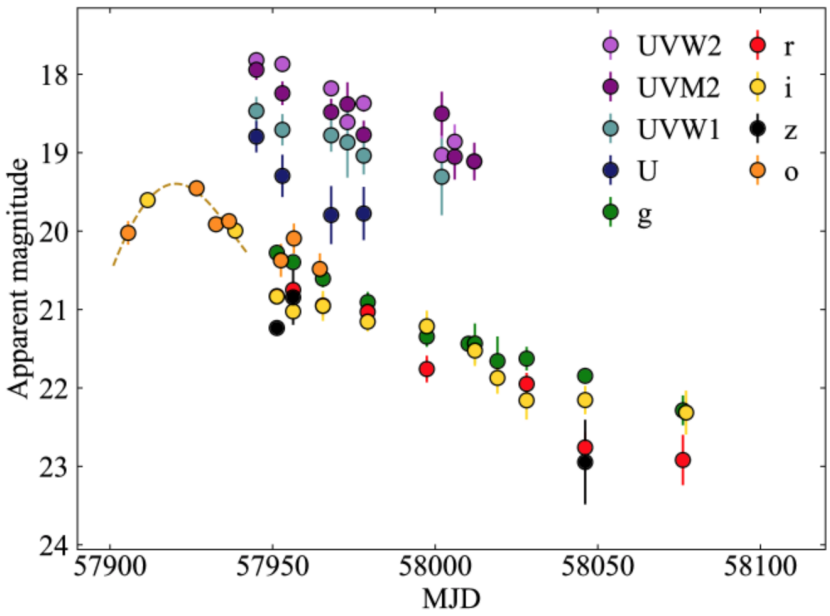

Figure 2.10: Optical and UV host-subtracted light-curves of the TDE AT2017eqx from different telescopes. The plot is from [Nicholl et al., 2019].

power-law decline [van Velzen et al., 2011], [Hung et al., 2017], [van Velzen et al., 2019]. Spectra have a blue, thermal continuum and broad ($5000 - 15000$ km/s) emission lines [Arcavi et al., 2014], [Hung et al., 2017]. Some have a soft X component, consistent with thermal emission from the inner part of the accretion disk [Komossa, 2015], [Miller, 2015], [Gezari et al., 2017], [van Velzen et al., 2019], [Wevers et al., 2019b]. The r_{BB} is $10 - 100$ times larger than the size expected from the debris disk, thus there is an unknown structure produced by outflows [Miller, 2015], [Metzger and Stone, 2017], [Dai et al., 2018] or by the intersecting streams of debris [Piran et al., 2015], [Jiang et al., 2016], [Bonnerot et al., 2017].
TDEs can be divided in X-ray bright and UV/optical bright. TDEs in the X-rays domain can also be divided in *X-ray TDEs*, *likely X-ray TDEs* and *possible X-ray TDEs* [Auchettl et al., 2018]. Such classes are only based on observational properties and may not reflect a true difference at physical level, since part of the emission could have been lost [French et al., 2020b].
Optical TDEs can be divided into several classes based on spectroscopic properties: those with He II but without H [Gezari et al., 2012], the He-rich to H-rich sequence [Arcavi et al., 2014], those showing Bowen fluorescence features of O III and N III [Blagorodnova et al., 2018], [Leloudas et al., 2019], those with gradual disappearance of broad H component whilst the broad

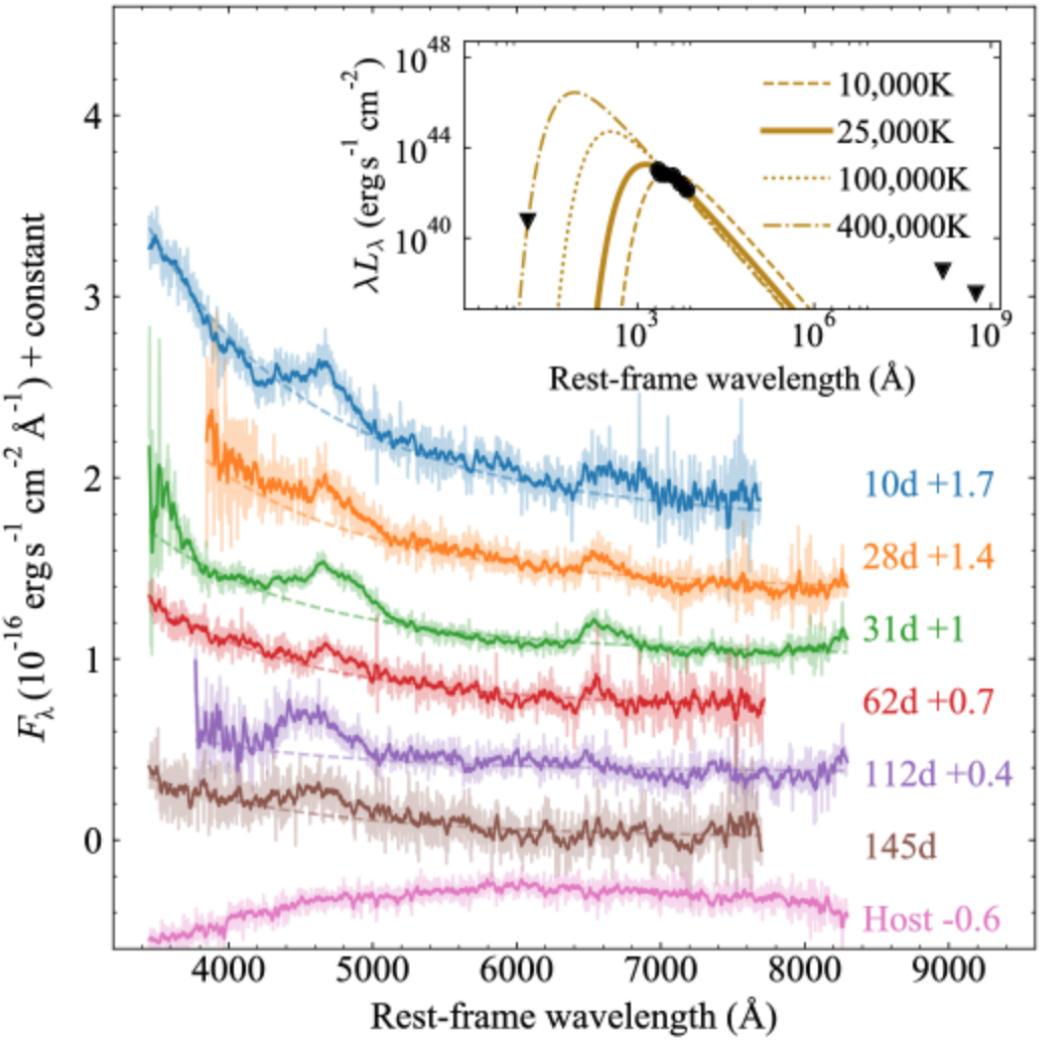

Figure 2.11: Post-peak spectral evolution of TDE AT2017eqx. The spectrum labelled "Host" contains only light from the host galaxy and has been subtracted from the others. Darker lines show the smoothed spectra, whilst dashed lines show fits with a black-body of $T_{BB} \approx 25000$ K. The insert shows the SED from X-ray to radio about 50 days after maximum light. The plot is from [Nicholl et al., 2019].

He II at 4686 Å remains strong [Nicholl et al., 2019]. UV spectra are also unique, with strong [N III] at 1750 Å but faint Mg II at 2896 and 2803 Å and [C III] at 1909 Å [Cenko et al., 2016]. In particular, [van Velzen et al., 2020] find that, in their flux limited sample comprehensive of ZTF observations, the ratio of H:Bowen:He TDEs is 9:7:1. H-TDEs have broad Hα and Hβ. Bowen-TDEs also have broad Hα and Hβ, in addition to broad emission around He II at 4686 Å and N III at 4640 Å, and emission at 4100 Å identified as N III, and sometimes O III at 3760 Å. He-TDEs have no Balmer lines, but only the broad He II emission close to 4686 Å. The diversity can be attributed to chemical composition [Gezari et al., 2012], [Kochanek, 2016], ionisation state of the debris [Guillochon et al., 2014] or reprocessing of X radiation in a dense and optically thick gas [Leloudas et al., 2019], [Wevers et al., 2019b].
Optically-bright TDEs are also characterised by a modest X-ray flux, either because the X-rays are reprocessed to optical wavelengths by the accretion disk [Guillochon et al., 2014], [Auchettl et al., 2018], [Dai et al., 2018], or because they are intrinsically faint because of a delayed accretion due to the timescale for debris circularisation [Piran et al., 2015], [Krolik et al., 2016], [Gezari et al., 2017].
TDEs with Bowen fluorescence features have smaller r_{BB}, longer rise time and higher rates than H-rich TDEs [Hinkle et al., 2020], [van Velzen et al., 2020]. The Bowen mechanism requires high densities, obtained at small radii, hence a longer diffusion timescale. This would indicate that the pre-peak light-curve of a TDE is dominated by the photon diffusion (rather than fallback) timescale. TDEs with only He have the longest rise time, highest luminosity and lower rates [van Velzen et al., 2020].
It appears that TDEs with higher bolometric luminosity have flatter slopes near peak, implying a slower light-curve decline. This is reminiscent of Phillips' relation found for type Ia SNe [Phillips, 1993]. [Hinkle et al., 2020] find that the UV/optical luminosity evolves smoothly and becomes flat in later observations. They find a correlation between peak luminosity and decline rate:

$$L_{peak} = 44.1^{+0.1}_{-0-1} + \left(1.1^{+0.3}_{-0.3}\right)(\Delta L_{40} + 0.5)$$

in CGS units, with $\Delta L_{40} = log_{10}(L_{40}/L_{peak})$, where -0.5 is the mean value of ΔL_{40} and L_{40} is the luminosity of the TDE 40 days after peak. The reduced χ^2 is 4.5, thus an intrinsic scatter is likely. If this is true, then TDEs are not well suited as distance indicators. Probably, this relation exists in the first place because the mass of the BH is the main driver of luminosity and evolutionary timescale. In a time Δt, the luminosity changes of $\delta L = \Delta t\,(L_{peak}/t_d)$, where t_d is the decay timescale. It thus follows that $L_{peak} \propto t_d^{-\alpha}$, with α being the slope of the relation. t_d is linked to the standard fallback time as $t_d \propto t_{fb} \propto M_{BH}^{1/2}$, hence $L_{peak} \propto M_{BH}^{-\alpha/2} \propto M_{BH}^{-0.55\pm0.15}$. This is consistent with the consideration that the peak accretion rate relative to Eddington luminosity is $\propto M_{BH}^{-3/2}$, or equivalently $\dot{M}_{peak} \propto M_{BH}^{1/2}$, with $L_{peak} \propto \dot{M}_{peak}$ [Metzger and Stone, 2016], [Kochanek, 2016], [Ryu et al., 2020].

2.3.2 Mechanism

The mathematical treatment of a stellar disruption operated by a SMBH described in this section is based on [Rees, 1988].

A central mass influences dynamics at all radii where $(GM_{BH}/r)^{\frac{1}{2}} \gtrsim \sigma(r)$, with $\sigma(r)$ the velocity dispersion at r. If the distribution of stars in the galaxy has a well-defined core, with its radius r_c and density N_*, a star of mass m_* has virial velocity $\sigma \simeq (Gm_*/r_c)^{\frac{1}{2}}$. Then, if $M_{BH} << N_* r_c^3$ the stars in the core will spend the majority of their lifetime moving under the influence of other stars, whereas the BH will dominate only inside a radius $r_h = GM_{BH}/\sigma^2 = \left(M_{BH}/N_* r_c^3\right) r_c$. There, a star that passes too close can no longer be considered a mass point because it is distorted by the BH gravitational force. The effect is important when the pericenter of the orbit r_{min} is comparable to the tidal radius $r_t \simeq 5 \cdot 10^{12} M_6^{1/3} (r_*/r_\odot)(m_*/m_\odot)^{-1/3}$ cm, where M_6 is the BH mass in units of 10^6 $M_\odot$. For a solar-type star, the escape velocity is $\sim 10^3$ km/s. Even if it passes at 2 or 3 times r_t, the external envelopes can be ripped off. If we consider isotropic velocities at r_h, the frequency at which a solar-type star approaches the BH at r_{min} is

$$10^{-4} M_6^{4/3} \left(\frac{N_*}{10^5\ pc^{-3}}\right) \left(\frac{\sigma}{100\ km/s}\right)^{-1} \left(\frac{r_{min}}{r_t}\right)\ \mathrm{yr}^{-1}$$

In order to have complete disruption, it must be $r_{min} < r_t$. If $r_{min} > 2 - 3r_t$, the star is only distorted and when it sets back to its original shape, internal dissipation takes place. If the dissipated energy is greater than the kinetic energy $E_K = \frac{m_* \sigma^2}{2}$, the star will set in an orbit bound to the BH because of energy conservation.

In order to disrupt a star, its self-binding energy must be overcome at the expenses of the orbital kinetic energy, which at r_t is larger by $\sim (M/m_*)^{\frac{2}{3}}$. Thus, unless there is an explosive input (and even then, only if the star passes ar $r << r_t$ [Carter and Luminet, 1982]), the debris will be tied to the BH, unless it has a very hyperbolic initial orbit. Whilst falling into the BH, a star develops a quadrupole distortion and the gravitational torque force makes it spin at near break-up angular velocity. The parts further from the BH have an extra velocity to the orbital velocity $v_{orb} \simeq (2GM/r_t)^{\frac{1}{2}} \simeq c(r_g/r_t)^{\frac{1}{2}}$ of order $v_* = (m_*/M_{BH})^{\frac{1}{3}} v_{orb}$. The portions closer to the BH have a velocity deficit and they are also deeper in the gravitational field of $\sim (GM_{BH}/r_t)(r_*/r_t) \simeq (Gm_*/r_*)$. This creates a spread in debris energies of $v_{orb}\Delta v$, with $\Delta v \simeq v_*$, which can also be enhanced by shocks. Some debris are also launched in hyperbolic orbits [Lacy et al., 1982].

On average, the debris have binding energy $\sim \frac{1}{2}(Gm_*/r_*)(M_{BH}/m_*)^{\frac{1}{3}}$. The orbits are very eccentric and debris of different stars are swallowed separately, since the swallowing timescale is short ($t \simeq 0.03 M_6^{1/2}$ years for a solar-type star). The debris inside $10^3 - 10^4$ r_g form a torus in a timescale slightly longer than the free-fall time, if they have angular momentum $\sim c r_t^{1/2} r_g^{1/2}$, with $r_g = GM_{BH}/c^2$. The torus is asymmetric and it is supported by radiation pressure. The binding energy is radiated without exceeding the Eddington luminosity of the BH, so that the timescale must be longer than $2.5 \cdot 10^8 (m_*/M_{BH})(r_t/r_g)^{-1}$ yr for a star at $r = r_t$. It takes then at least $5 M_6^{-1/3}$ years for 1 $M_\odot$ of debris to deflate to a thin ring and $50 \epsilon_{0.1} M_6^{-1}$ years to be swallowed by the BH with a radiative efficiency $\epsilon = 0.1\epsilon_{0.1}$. Viscosity can play a role in faster processing of the material, then $L \simeq L_{Edd} = 10^{44} M_6$ erg/s for no longer than $17 \epsilon_{0.1}^{-0.4} M_6^{-0.6} t_i \sim 0.5 M_6^{-0.1} \epsilon_{0.1}^{0.4}$ yr, then it declines as $t^{-5/3}$. Most debris are swallowed quickly, so that a flare peaking in UV/X-ray at $L \simeq L_{Edd}$ becomes significantly luminous, only to become fainter in few days.

Half of debris escape in hyperbolic orbits, with material beamed in a cone close to the orbital

plane. There is no flare until they fall back onto the BH after an orbital period $t_i \simeq 0.03 M_6^{1/2}$ yr, unless they are decelerated by external matter.
When $M_{BH} > 10^8$ $M_\odot$, relativistic effects cannot be ignored and also the form of the BH (Schwarzschild or Kerr) and eventually the orientation of the star orbit with respect to its spin (in a Kerr BH) become important. In this case, smaller stars are completely swallowed and only massive stars lead to TDEs. Stars are entirely swallowed if $M_{BH} > M_{Hills} \approx 10^8$ $M_\odot$ for a non-spinning BH and a solar-type star [Hills, 1975].
Debris are believed to circularise fast, creating an accretion disk. The process is fast if $r_p \lesssim 10 r_g$. This is true for $\lesssim 1/4$ of the events with $M_{BH} = 10^6$ $M_\odot$. For $10 < r_p/r_g < 27$ and $M_{BH} = 10^6$ $M_\odot$, a main sequence star is completely disrupted but the debris have eccentric orbits with a semimajor axis 100 times the expected disk [Krolik et al., 2020]. Partial disruption events with $\gtrsim 10\%$ of mass lost have about the same rate as total disruption, whereas partial disruption ones with $\gtrsim 50\%$ of mass lost are 30% more frequent. A partial disruption precedes a total disruption when the angular momentum of the star evolves in the "empty loss cone" regime, and it changes the orbital energy of $\gtrsim O(1)$. Usually, remnants of partial disruptions are not in thermal equilibrium [Krolik et al., 2020].
About half m_* becomes unbound and is ejected at 10^4 km/s. Interaction with the interstellar medium generates shocks which can produce synchrotron emission. [Yalinewich et al., 2019] find that when the periapse distance of the star decreases, the outflow is faster and wider.
[Coughlin and Nixon, 2019] propose a model for which the stellar core survives the encounter and keeps an active gravitational influence on the stellar debris. The asymptotic fallback rate in partial TDEs scales as $t^{-2.26\pm0.01}$ and is independent from the mass of the core. They also find that the late-time accretion rate scales as $t^{-5/3}$ if the the star is completely disrupted, or as $t^{-9/4}$ if the disruption is only partial and a core remains. This results follows the consideration that a Kepler energy-period relation in debris orbits cannot work in presence of a core generating a time-dependent gravitational potential.

2.3.3 Rates and host galaxies

The expected frequency of TDEs is between $10^{-4} - 10^{-5}$ per year per galaxy [van Velzen and Farrar, 2014], [Holoien et al., 2016], although several galaxies show enhanced rates.
The rate of UV/optical TDEs depends on the recent star formation history of the galaxy. The rate increases of $20 - 200$ times in quiescent, Balmer-strong and post-starburst galaxies (e.g. [French et al., 2016], [Law-Smith et al., 2017], [Graur et al., 2018]), perhaps due to a higher star concentration in the centre, which means more stars available for disruption, or these galaxies could be post-mergers with an inspiralling SMBH binary (SMBHB).
Morphologies are diverse, but there are no grand design spirals nor irregular dwarfs. Dust is generally absent, aside for the spiral arms. This is not surprising, considering that dust in the centre could make TDE detections practically impossible. [French et al., 2020a] find that even non-starburst hosts have a central surface brightness close to a starburst. The colour in general is bluer in the centre than at the outskirts, but this is not always the case. This could hint to a different origin of the central point source, with bluer galaxies dominated by a young stellar cluster, or an AGN, or a more concentrated light profile of the stars, and redder dominated by

a concentrated old stellar population or covered by dust.
Host spectra often show recent but not ongoing star formation. They lack strongly disrupted morphologies, thus indicating that there have not been major merging events. Minor merges are instead possible, and they could have triggered the starburst. The hypothesis of a SMBHB is less plausible, because the coalescence time after a merger is longer than the post-burst age [Boylan-Kolchin et al., 2008], so the two SMBHs could not be close enough to form a binary system to enhance TDE rates yet [Ivanov et al., 2005], [Chen et al., 2011]. This leaves high central density as the most probable cause of the observed enhancements [French et al., 2020a].
Many hosts of UV/optical bright TDEs with large H and He emission lines show E+A (no signs of evident ongoing star formation, but dominated by a young stellar population [Dressler and Gunn, 1983]) or post-starburst spectra [Arcavi et al., 2014], characterised by lack of strong emission lines, indicating low rate of current star formation, and strong Balmer absorption, which in turns points to bursts of star formation within a Gyr. These galaxies are rare in the local Universe, but they are frequent TDE hosts [French et al., 2016], [French et al., 2017], [Law-Smith et al., 2017], [Graur et al., 2018].
Theoretical predictions pose most TDEs in low mass galaxies with a SMBH of $10^4 - 10^6$ $M_\odot$ [Wang and Merritt, 2004], but the observed distribution peaks at 10^7 $M_\odot$ [Stone and Metzger, 2016], [Kochanek, 2016] or 10^6 $M_\odot$ [Wevers et al., 2017]. Between $10^{5.5} - 10^{7.5}$ $M_\odot$ the TDE rates seem constant [van Velzen, 2018]. Since the temperature of the accretion disk decreases with increasing M_{BH} [Dai et al., 2015], it would appear that X-ray TDEs have smaller M_{BH} than UV/optical TDEs, but their emission requires a rapid cirularisation of debris, which is favoured at larger M_{BH} [Guillochon and Ramirez-Ruiz, 2015]. This dichotomy could be explained if X-ray and UV/optical TDEs were the same event with a difference in the viewing angle or geometry [French et al., 2020b].
TDE hosts are dominated by their elliptic component, typical of early-type galaxies. Those at close redshift show a compact core and an extended spiral or disk structure.

A TDE is a possible explanation for SNhunt133. The analysis of its light-curve, as well as its spectral lines, will give insights on the matter. Its host, which is a SB(s)c starburst galaxy, shall be taken into consideration as well.

CHAPTER

3

THE DISCOVERY OF SNHUNT133 AND ITS HOST GALAXY

3.1 Discovery

The target discussed in this dissertation, SNhunt133 (a.k.a. PSN J17124620+2313265), was discovered in 2012 in the nucleus of NGC 6315 at coordinates RA = 17:12:46.15, DEC = +23:13:24.9 (J2000.0) by the Catalina Real-Time Transient Survey, [Drake, 2012]. A first evidence of a variability at the location of the galaxy nucleus was found on 2012 May 30^{th}, with the outburst onset likely occurring between May 13^{th} and May 27^{th}.
On June 26^{th}, 2012, the source brightened by $0.2 - 0.3$ mag, reaching a luminosity peak of 14.9 mag. Between 2005 April 10^{th} and 2012 April 25^{th}, the galaxy core remained quiescent, according to the 293 observations of Catalina Surveys Data Release 1[1] [Drake, 2012].
A classification spectrum of the transient was taken on 2012 July 24^{th}, and it was found to be similar to an archival spectrum of NGC 6315 of the Sloan Digital Sky Survey (SDSS) taken several years before the transient discovery (see chapter 5). [McCrum et al., 2012] classified the transient as the likely onset of AGN-like variability of a previously quiescent nucleus of a star-forming galaxy. However, [Drake, 2012] questioned this conclusion, remarking that the spectrum of the core of NGC 6315 still showed line ratios that were inconsistent with those of a narrow-lined AGN, whereas they well fitted those of a normal star-forming galaxy. For this reason, [Drake, 2012] favoured a SN or TDE interpretation for SNhunt133.

[1] http://nesssi.cacr.caltech.edu/DataRelease/index1.html

3.2 Host galaxy, redshift, distance

NGC 6315 was so far considered to be a star-forming, SB(s)c galaxy without a known photometric variability. A coloured picture of the host galaxy is shown in Figure 3.1. The redshift

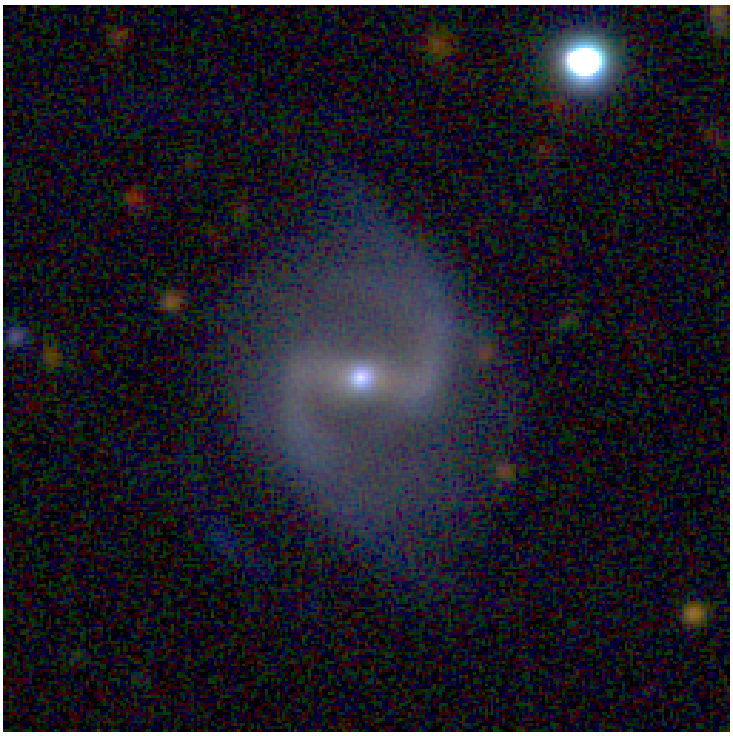

Figure 3.1: Coloured picture of NGC 6315 in g,r,i bands. The image is from [Baillard et al., 2011].

is $z = 0.02260 \pm 0.00006$ from [De Vaucouleurs et al., 1991]. From this redshift, a recessional velocity of 7048 ± 21 km/s (corrected for the Virgo infall only, disregarding the Great Attractor and the Shapley supercluster) is derived [Mould et al., 2000]. This is the preferred estimate of the velocity considering that at this distance scale the Virgo cluster is the main attractor. This yields a distance of 103.96 ± 7.28 Mpc and a distance modulus $(m - M) = 35.08 \pm 0.15$ mag, adopting $H_0 = 67.8$ km/sec/Mpc, $\Omega_{matter} = 0.308$, $\Omega_{vacuum} = 0.692$.

3.3 Reddening towards SNhunt133

The line-of-sight extinction towards SNhunt133 includes two main contributions. A local reddening contribution is due to the dust within the Milky Way (MW), as tabulated by [Schlafly and Finkbeiner, 2011] and reported in Table 3.1. The adopted reddening law is $R_V = \frac{A_V}{E(B-V)} = 3.2$ from [Olson, 1975]. Therefore, the colour excess is $E(B-V) = \frac{A_V}{R_V} = 0.054 \pm 0.005$ mag, where an error of 10% is adopted. Additional reddening can be due to the host galaxy dust.
For estimating the host galaxy contribution to the total reddening, I made use of the highest resolution spectrum of the transient obtained on 2012 August 19^{th} with VLT and XShooter

Band	A_λ
U	0.274
B	0.229
V	0.174
R	0.137
I	0.095

Table 3.1: Coefficients of Galactic absorption.

(see chapter 5). The extinction due to the host galaxy is evaluated from the equivalent width (EW) of the lines of the interstellar Na $\lambda\lambda 5890 - 5896$, through empirical relations provided by [Poznanski et al., 2012]. These relations state that:

$$log(E(B-V)) = 2.16 \cdot EW(D_2) - 1.91 \pm 0.15$$

$$log(E(B-V)) = 2.47 \cdot EW(D_1) - 1.76 \pm 0.17$$

$$log(E(B-V)) = 1.17 \cdot EW(D_1 + D_2) - 1.85 \pm 0.08$$

where $EW(D_2)$ is the EW of Na $\lambda 5896$, $EW(D_1)$ is the EW of Na $\lambda 5890$ and $EW(D_1 + D_2)$ is the EW of both lines combined.
A zoom on the Na I doublet in the X-Shooter spectrum is shown in Figure 3.2.

The above relations are used to compute three different estimates of $E(B-V)$, whose weighted average value is $E(B-V) = 0.086 \pm 0.003$ mag. This value is to be added to the MW component, which gives a total $E(B-V) = 0.140 \pm 0.006$ mag. This will be the value of the colour excess adopted hereafter.

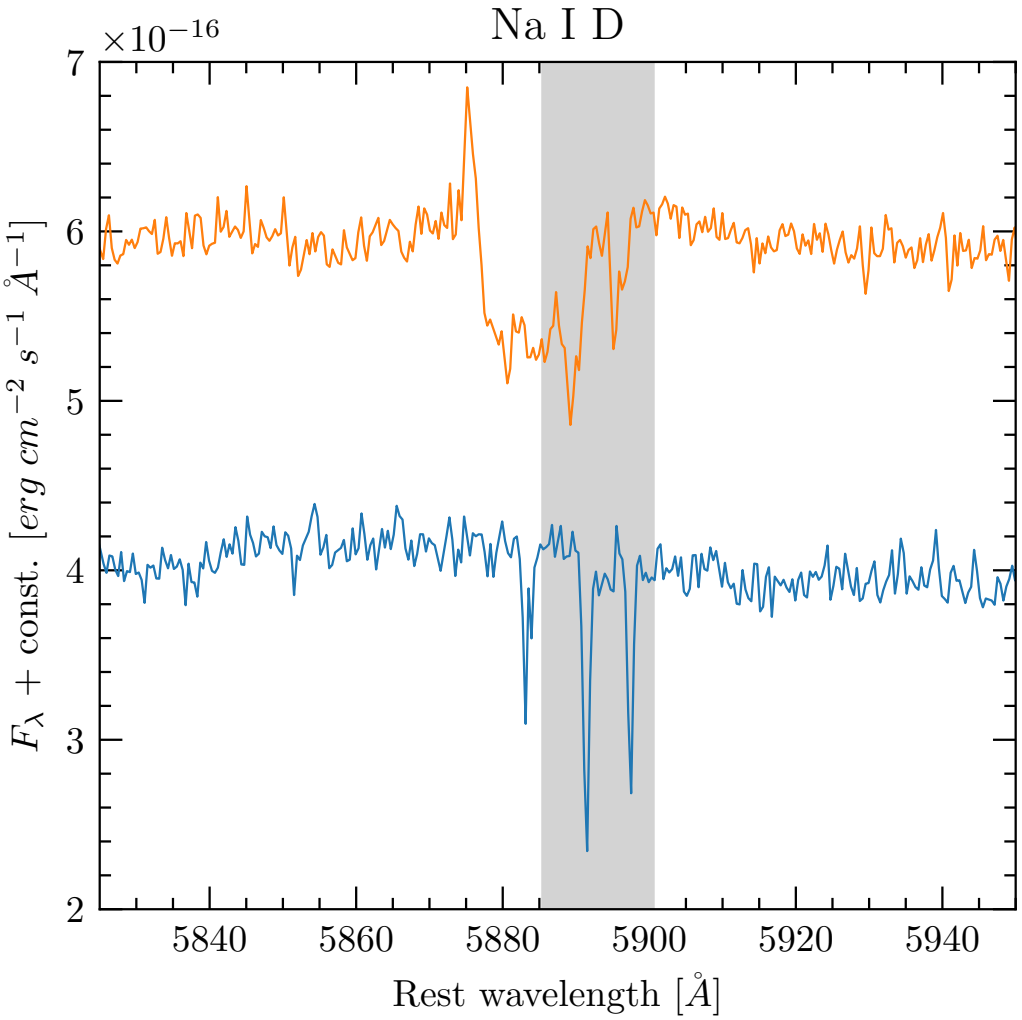

Figure 3.2: Blow-up of the XShooter spectrum of SNhunt133 in the region of the interstellar Na $\lambda\lambda$5890−5896 lines, emphasised with a thick grey column. The blue line represents the spectrum not corrected for redshift, hence the Na I D shown is of the MW. The orange line represents the spectrum corrected for redshift and the narrow Na I D is of the host galaxy.

CHAPTER

4

PHOTOMETRY

SNhunt133 was observed by professional and amateur telescopes, providing an extensive dataset with multiple instruments. Data are both photometric (bands U, B, V, R, I, J, H, K) and spectroscopic in the optical and near-infrared (NIR) domains. Observations of the transient with professional telescopes span a period from 2012 July 26^{th} to 2013 March 20^{th}. Archival images from 2MASS (Two Micron All Sky Survey) taken in 1997 where used as templates for IR data. Unfiltered amateur photometric monitoring started in 2009 and continued until 2019. Telescopes and instruments used are listed in Section 4.1 and Table 5.1.
Data reduction was performed both for photometric and spectral images. Different data reduction techniques, which will be extensively described later in this chapter and the next one, were applied to the spectro-photometric dataset.

4.1 Photometric data set

The goal is to determine the transient magnitude in order to construct its light-curve evolution in various bands. Data were taken with the following instrumental configurations:

- AFOSC (Asiago Faint Object Spectrograph and Camera), mounted on Copernico 1.82 m telescope in Asiago. U, V, B, R, I bands.
- EFOSC2 (ESO Faint Object Spectrograph and Camera 2), mounted on NTT (New Technology Telescope) telescope in La Silla. U, V, B, R, I bands.
- SofI (Son of ISAAC), mounted on NTT telescope in La Silla. J, H, K bands.

- NICS (Near Infrared Camera Spectrometer), mounted on TNG (Telescopio Nazionale Galileo) telescope in La Palma. J, H, K bands.
- 1.3-m telescopes at Mt. Hopkins and CTIO (Cerro Tololo Inter-American Observatory), Chile, dedicated to 2MASS. J, H, K bands.
- Amateur photometry, collected using the 0.53 m Ritchey-Chretien telescope of the Montarrenti Astronomical Observatory (Siena, Italy) and an Apogee Alta U47 CCD camera. Unfiltered photometry.

Since the transient is located in the nucleus of a galaxy, it is of fundamental importance to carefully subtract the galactic contamination. This can either be done before or after measuring the magnitude. In this work, both approaches will be used, leading to slightly different results. In Sections 4.1.3 and 4.1.4 they will be discussed more thoroughly.

4.1.1 Preliminary reduction

First of all, raw images are corrected for *bias* and *flat-field*. Several bias and flat-field frames are taken and combined to produce a median image. This is mainly done using tasks `zerocombine` and `flatcombine` in IRAF package `ccdred`. The resulting images, generally called *masterbias* and *masterflat*, are applied to scientific images using `ccdproc`. At the same time, the overscan strip is trimmed from the raw images. In Figure 4.1 an example of pre-reduced image is shown.

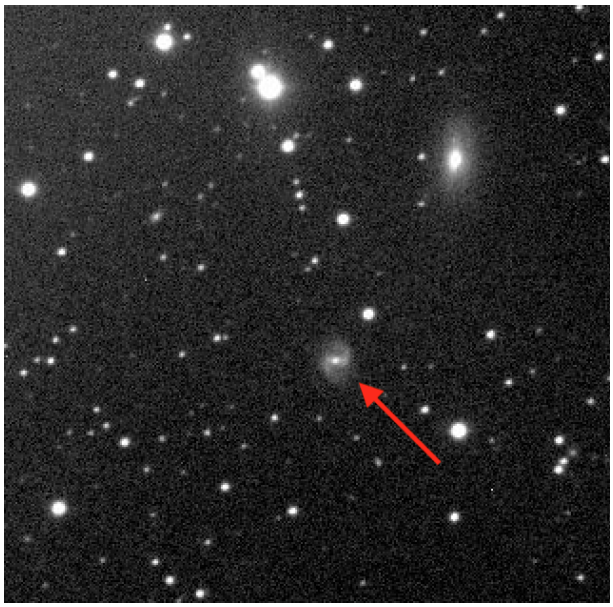

Figure 4.1: Pre-reduced image of NGC 6315 taken with Copernico 1.82 m telescope equipped with AFOSC (R band). The red arrow indicates the target.

4.1.2 SNoOPy

Once the images are corrected, it is possible to proceed with magnitude measurement. This is done using SNoOPy (SuperNOva PhotometrY) pipeline[1]. It makes use of various python scripts, as well as the classical packages HOTPANTS, SEXTANT and DAOPHOT.
The seeing is evaluated, either automatically or selecting reference stars by hand and measuring their FWHM, via SNoOPy task `ecseeing`. This will be important for PSF modelling.
All images are astrometrised using `ecastro`, which compares reference stars with catalogued stars. Several catalogues are available; in this case, the 2MASS catalogue is used.
After the images are astrometrised, it is possible to combine multiple images obtained in the same night and in the same band to increase the signal-to-noise ratio (S/N). This is done using the task `ecdither`. Multiple images were usually taken in U and B bands, as the source is typically fainter in such bands. Multiple images are preferentially taken instead of longer single images to avoid saturating the source, which can happen if the exposure time is too long compared to the target emissivity.
Then, the PSF is modelled using field stars in the image. The task `ecpsf` allows us to select and examine stars to ensure they are not saturated or otherwise contaminated by residual background light. The Gaussian profiles of the stars are averaged to generate the PSF model for that particular image. In some cases, where the image had some field distortion, it was necessary to select only stars close to the source, since it was noted that the PSF tended to vary within the image. In Figure 4.2 an example of averaged PSF is shown.

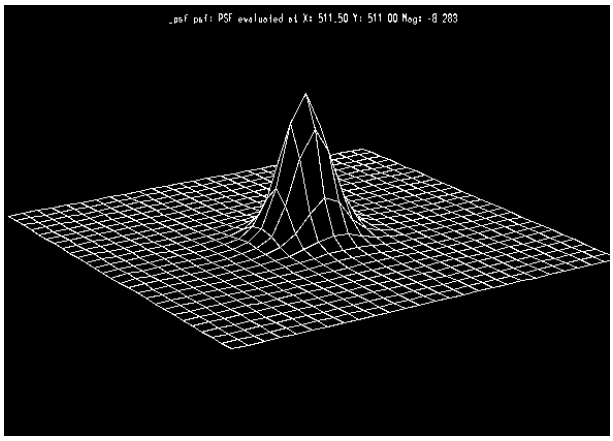

Figure 4.2: An example of averaged PSF profile over multiple reference stars PSF.

4.1.3 PSF-fitting photometry

In this case, the magnitude was measured directly on the image and it accounts for the contributions of the galactic nucleus and the transient itself. A priori, the weight of each component

[1]SNOoPy is a package for SN photometry using PSF fitting and/or template subtraction developed by E. Cappellaro. A package description can be found at http://sngroup.oapd.inaf.it/ecsnoopy.html.

is unknown. The resulting magnitudes for the different bands and epochs are shown in Table 4.1 and are plotted in the light-curve of Figure 4.3.

Date	MJD	U	B	V	R	I	Instrument
20120726	56134.930	17.122 ± 0.297	17.417± 0.252	16.950 ± 0.611	16.852 ± 0.408	16.165 ± 0.344	AFOSC
20120731	56139.965	-	17.273± 0.073	16.844± 0.079	16.412 ± 0.082	15.965± 0.073	AFOSC
20120801	56140.880	16.863 ±0.326	17.300 ±0.308	17.054± 0.532	16.519 ± 0.230	16.061± 0.341	AFOSC
20120808	56147.065	17.041± 0.030	17.389± 0.021	16.857± 0.029	16.414± 0.021	15.984 ±0.026	EFOSC
20120817	56156.940	17.165± 0.205	17.676 ±0.541	17.105± 0.626	16.712 ±0.674	16.096± 0.177	AFOSC
20120818	56157.940	-	17.518± 0.288	17.222 ±0.365	16.642 ±0.399	16.482 ±0.557	AFOSC
20120822	56161.885	-	17.567± 0.129	17.008± 0.145	16.695 ±0.274	16.147 ± 0.075	AFOSC
20120910	56180.865	-	17.856± 0.388	17.174 ±0.085	16.857 ± 0.188	16.444± 0.205	AFOSC
20120917	56187.845	-	18.137 ±0.303	17.365 ±0.053	16.992 ±0.120	16.539 ± 0.118	AFOSC
20121019	56219.740	-	17.671 ±0.149	17.366 ±0.089	16.927 ±0.076	16.565 ± 0.080	AFOSC
20121107	56238.715	17.249± 0.062	17.693± 0.119	17.348± 0.156	16.949± 0.146	16.547± 0.136	AFOSC
20130320	56371.160	17.311 ±0.121	17.770± 0.124	17.417± 0.102	17.029 ±0.152	16.645± 0.077	AFOSC

Table 4.1: Magnitudes measured through PSF-fitting, comprehensive of both galactic nucleus and transient.

The data analysis procedure is as follows: the PSF model previously obtained is fitted to a squared region where the background is estimated with the task `ecsnfit`. The polynomial order for fitting the background can also be varied. Once the fit is done, the program shows the residual image, as well as the fitted source (see for example Figure 4.4). The fit is optimal when it provides a negligible residual. The task `ecarterr` returns an error estimate that accounts for the PSF-fitting error and the location of the target in a non-flat background region.

The magnitudes resulting from this operation are instrumental, meaning they depend on the counts on the pixels selected within the aperture and are simply equal to $-2.5\log(\text{counts})$. In order to compare magnitudes retrieved from different instruments or even just in different nights, it is necessary to calibrate them to a standard system.

A catalogue of reference stars is downloaded from the Sloan Digital Sky Survey (SDSS)[2], which covered the field of SNhunt133. The Johnson-Cousins catalogue of the same reference stellar sample is obtained by converting SDSS magnitudes using the relations of [Chonis and Gaskell, 2007]. Night zeropoints and instrumental colour terms are obtained using the task `ecph`. Zeropoint corrections for non-photometric nights (or nights for which zeropoints are not available) are computed using `ecnightcal`. The pipeline allows for star rejection in an interactive process (example shown in Figure 4.5).

The corrections are applied to measured magnitudes through `ecsncal`, which also plots the output magnitudes with respect to time, recreating the luminosity evolution of the transient. The error associated to each magnitude is the root sum of squares of instrumental magnitude error, coming from `ecsnfit`/`ecarterr`, and the photometric calibration, dominated by the zeropoint uncertainty.

Data taken after 2012 October 19^{th} show a flat light-curve. At this epoch, the transient is assumed to have faded and the corresponding magnitude is that of the galactic nucleus. This value is to be subtracted to the previous observations of the quiescent host galaxy to derive the

[2]https://www.sdss.org

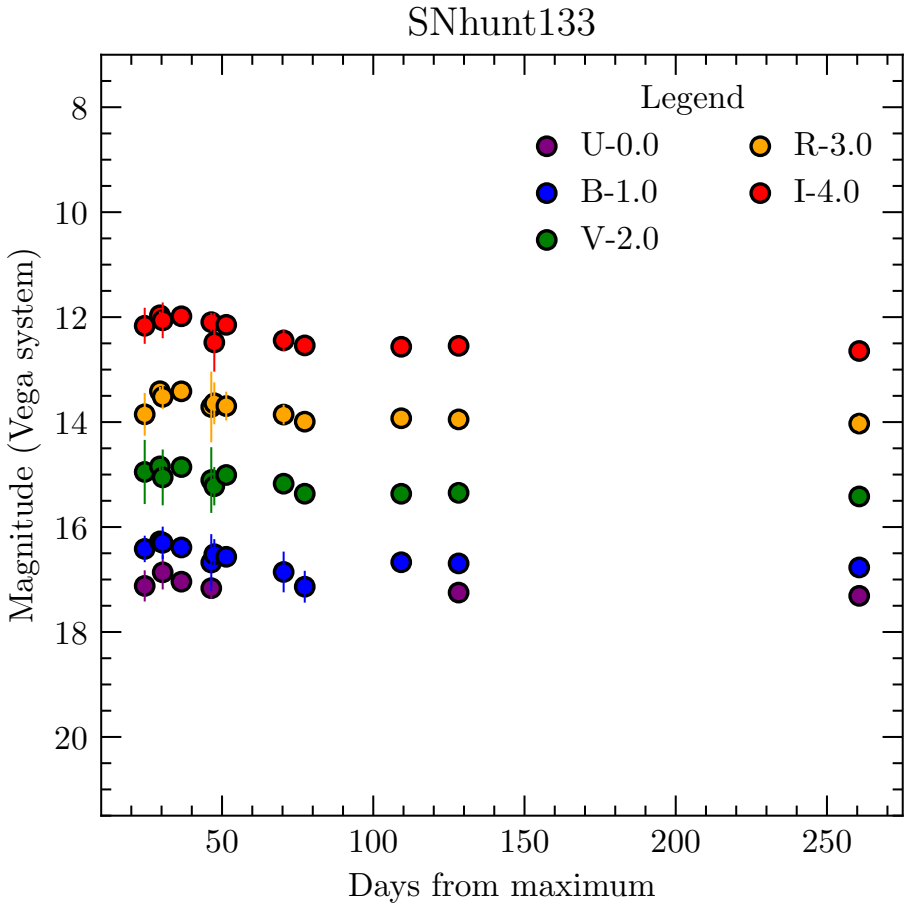

Figure 4.3: Light-curve obtained plotting the magnitudes in Table 4.1 with respect to time.

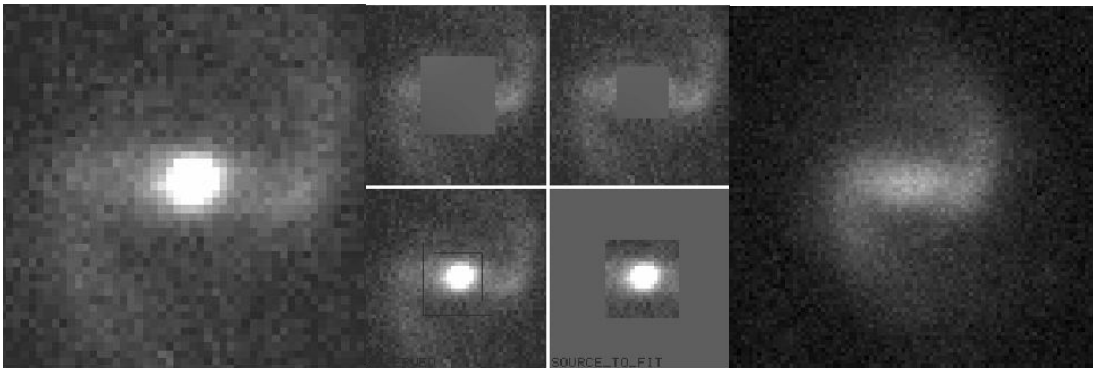

Figure 4.4: Left: Image of the target before the extraction. Centre: Image shown during the extraction process; left up is the target minus the selected region for the fit, right up is the background, left down is the target with the selected region (black square), right down is the source to fit. Right: Image of the target after the extraction. Notice how the central luminosity is way dimmer and comparable to that of the spiral arms.

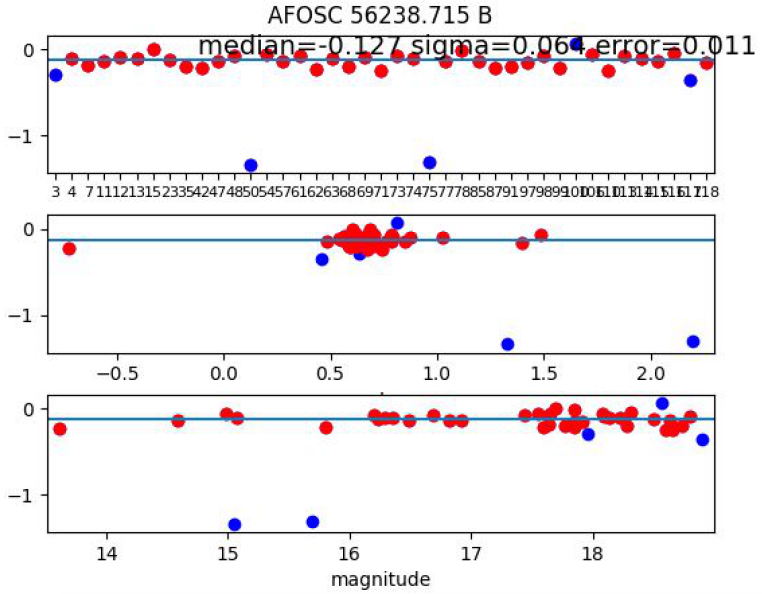

Figure 4.5: Example of zeropoints interactive calibration. Red dots are good reference stars for estimating the zeropoint, blue dots are rejected stars. In the top panel the stars are arranged following the catalogue number, following the colour in the middle and following the magnitude at the bottom. On the y-axis is the residual, whereas on the very top the intrument, MJD, filter, mean correction coefficient with its sigma and error are shown.

magnitude of the transient alone.
I first convert all magnitudes and errors in fluxes. This is done using the online tool provided by Gemini Observatory[3]. Then, fluxes are subtracted to that of the clean galactic core found before, and the result is again transformed in magnitude. I hence obtain the transient magnitude and exclude the host galaxy contribute. Magnitudes obtained with this procedure are shown in Table 4.2. Errors are computed by standard error propagation.

Date	U	B	V	R	I	Instrument
20120726	19.415 ± 0.302	18.966 ± 0.263	18.159 ± 0.614	19.533 ± 0.413	17.372 ± 0.348	AFOSC
20120731	-	18.462 ± 0.104	17.864 ± 0.100	17.435 ± 0.103	16.853 ± 0.089	AFOSC
20120801	18.143 ± 0.331	18.545 ± 0.317	18.514 ± 0.536	17.735 ± 0.238	17.083 ± 0.345	AFOSC
20120808	18.878 ± 0.063	18.854 ± 0.077	17.898 ± 0.068	17.441 ± 0.065	16.896 ± 0.058	EFOSC
20120817	19.871 ± 0.206	20.886 ± 0.546	18.724 ± 0.566	18.532 ± 0.677	17.175 ± 0.184	AFOSC
20120818	-	19.468 ± 0.297	19.38 ± 0.370	18.166 ± 0.404	18.968 ± 0.559	AFOSC
20120822	-	19.804 ± 0.149	18.347 ± 0.158	18.401 ± 0.281	17.319 ± 0.091	AFOSC
20120910	-	-	19.071 ± 0.105	19.594 ± 0.198	18.641 ± 0.211	AFOSC
20120917	-	-	21.887 ± 0.081	-	19.731 ± 0.129	AFOSC

Table 4.2: Magnitudes of the transient once the galactic component is subtracted.

4.1.4 Template subtraction

Alternatively, template subtraction allows us to subtract a physical template image to a scientific image, thus allowing to measure the instrumental magnitude of the transient after properly removing the host galaxy contamination. In this work, I used template images in different filters obtained during the night of March, 19^{th}, 2013. In fact, given the results from PSF-fitting photometry discussed in Section 4.1.3, it was assumed that the transient had already faded away to that date.

Date	MJD	U	B	V	R	I	Instrument
20120726	56134.93	17.938 ± 0.142	18.327 ± 0.041	17.726 ± 0.025	17.392 ± 0.043	17.011 ± 0.031	AFOSC
20120731	56139.965	-	18.351 ± 0.041	17.858 ± 0.028	17.405 ± 0.028	16.934 ± 0.024	AFOSC
20120801	56140.88	18.402 ± 0.131	18.467 ± 0.029	17.983 ± 0.032	17.408 ± 0.047	16.947 ± 0.071	AFOSC
20120808	56147.065	18.509 ± 0.038	18.467 ± 0.023	17.795 ± 0.011	17.515 ± 0.01	17.132 ± 0.02	EFOSC
20120817	56156.94	19.05 ± 0.118	19.042 ± 0.08	18.345 ± 0.036	17.792 ± 0.055	17.145 ± 0.051	AFOSC
20120818	56157.94	-	19.05 ± 0.059	18.372 ± 0.041	17.799 ± 0.027	17.178 ± 0.058	AFOSC
20120822	56161.885	-	19.252 ± 0.101	18.293 ± 0.029	17.801 ± 0.042	17.477 ± 0.036	AFOSC
20120910	56180.865	-	19.756 ± 0.285	19.346 ± 0.056	18.651 ± 0.044	18.264 ± 0.085	AFOSC
20120917	56187.845	-	$> 18.091 \pm 2.501$	20.58 ± 0.165	19.743 ± 0.108	19.006 ± 0.117	AFOSC
20121019	56219.74	-	20.467 ± 0.214	20.329 ± 0.156	19.901 ± 0.121	19.596 ± 0.143	AFOSC
20121107	56238.715	$> 18.467 \pm 2.500$	$> 20.120 \pm 1.000$	$> 20.156 \pm 2.500$	20.207 ± 0.239	$> 18.959 \pm 2.500$	AFOSC

Table 4.3: Magnitudes of the transient alone, obtained with the template subtraction technique.

The method first performs an accurate astrometric calibration of the two images, accounting for

[3]https://www.gemini.edu/sciops/instruments/midir-resources/imaging-calibrations/fluxmagnitude-conversion

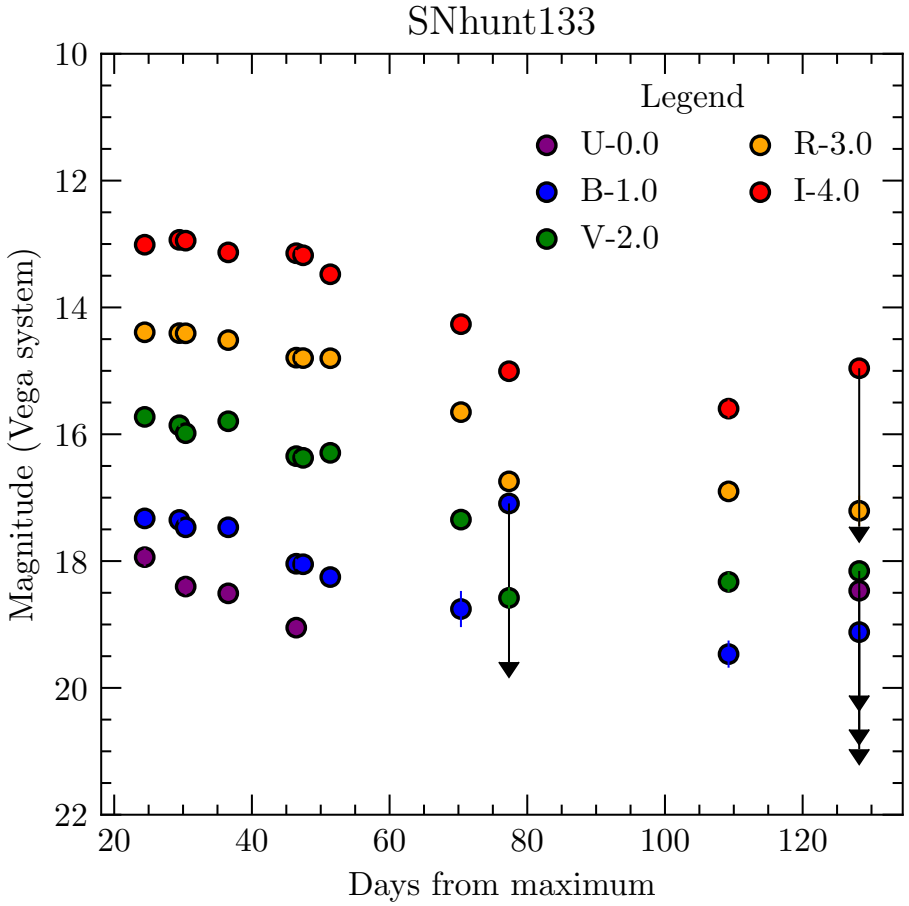

Figure 4.6: Light-curve obtained plotting the magnitudes calculated from template-subtracted images with respect to time. A black arrow indicates an individual upper limit.

different pixel sizes. It also performs photometric and seeing matching of the two images, before subtracting the template image to that with the transient object. This procedure provides the best results when the images come from the same instrument, however, it has been successfully applied also to cases where the two frames were taken with different telescopes. SNoOPy task `ecsndiff` allows for modifications to the number of sources considered during the subtraction, the background and kernel orders. Figure 4.7 shown an example of the subtraction process. It is

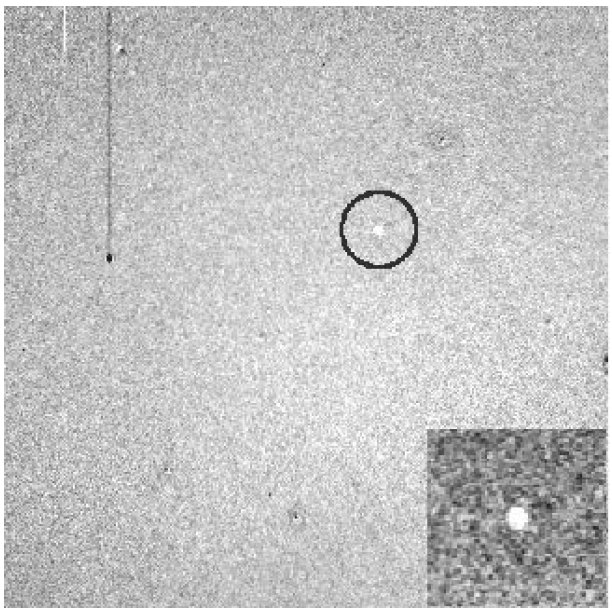

Figure 4.7: Difference images after performing template subtraction. The black circle identifies the target, whilst the square on the bottom right shows a zoom on the target.

also possible to divide the images in smaller areas and subtract those independently. This is done particularly in cases with saturated stars, poorly-corrected reflections or other imperfections make the exact subtraction difficult. Nevertheless, the subtraction is considered optimal when the background is flat and the only source of light remaining comes from the target.

The difference image then goes through the same procedure of PSF fitting described in Section 4.1.3. In Figure 4.8 an example of such fitting is shown. Errors are the square root of the error on the fit and the photometric error. These are usually smaller than those obtained through the analysis of images without template subtraction, as they are computed in a flat background.

SNhunt133 is located exactly in the galactic nucleus and is affected by strong contamination from the host, hence a fit with a stellar PSF profile sometimes failed. On these occasions, only a lower limit could be established.

Finally, the instrumental magnitudes are calibrated as described in the previous Section. Single night zeropoints and colour-corrections are calculated with SNoOPy. Calibrated magnitudes are shown in Table 4.3 and plotted with respect to the time to retrieve the light-curve (Figure 4.6).

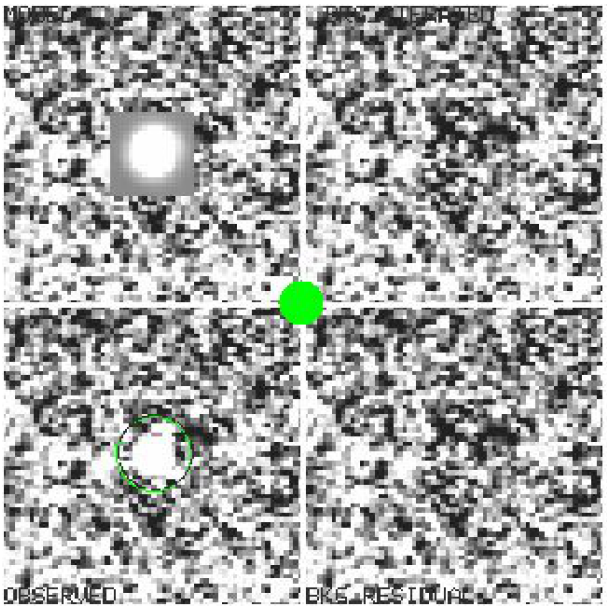

Figure 4.8: Top left: Model of the source. Top right: background. Bottom left: Source to fit. Bottom right: Residual image. The green dot in the centre indicates that the fit has a sufficient signal-to-noise (S/N) ratio to confirm a solid detection.

4.1.5 Treatment of unfiltered amateur data

The target was also observed by amateur astronomers of the Montarrenti Observatory (Siena, Italy). Aperture photometry of a number of unfiltered images spanning a seven-year period (from 2012 to 2019) has been preformed on the nucleus of NGC 6315. The data are unfiltered observations obtained with a 0.53m f/8.7 Ritchey-Chretien telescope equipped with an Apogee Alta U47 CCD camera, with a pixel scale of 1.17 arcsec/pixel (with 2×2 binning configuration). A fixed aperture of 4 pixels (hence, $\sim$ 4.7 arcsec) has been used for estimating the flux of the galaxy core, whilst the background contamination was determined using an outer annulus 5 pixels wide, detached from the fixed aperture by 10 pixels[4]. Instrumental magnitudes are then calibrated using three stars from the UNSO-A2 catalogue[5], whose magnitudes are reported in Table 4.4. The magnitudes of the three reference stars reported in Table 4.4 are systematically offset by 0.5 mag with respect to the same stars from our catalogue (see Section 4.1.3). Hence, in order to compare the amateur magnitudes to the filtered observations reported in Section 4.1.3, we apply a correction of +0.5 mag.
Once re-calibrated, amateur magnitudes, which are comprehensive of the contribution of both the transient and the galactic nucleus, are converted to fluxes. Then, an average value of the nucleus magnitude is calculated from averaging the estimates over a number of epochs, when

[4]This detachment explains the shift between amateur magnitudes of nucleus+transient showed in Figure 4.10 and the magnitudes of nucleus+transient derived with PSF-fitting photometry listed in Table 4.1. In fact, evaluating the background contamination with such distance from the nucleus, its contribution is underestimated and brighter manitudes hence result.

[5]http://tdc-www.harvard.edu/catalogs/ua2.html

USNO-A2	RA	DEC	R (mag)
1125-08079219	17:12:40.73	+23:12:45.68	15.2
1125-08081251	17:24:9.92	+23:12:37.78	15.9
1125-08082132	17:12:54.00	+23:12:25.77	16.5

Table 4.4: Standard stars used in calibration of amateur aperture photometry.

the transient was no longer visible. This value is transformed in flux and it is subtracted from the observed fluxes. The subtracted flux is finally re-converted to magnitude with the inverse transformation. For all conversions, the online tool provided by Gemini Observatory[6] is used. The resulting magnitudes are shown in Table 4.5 and Figure 4.9.

Date	MJD	R (mag)
20120516	56063.978	18.144 ± 0.066
20120530	56077.007	17.684 ± 0.049
20120607	56085.987	17.428 ± 0.059
20120612	56090.916	17.069 ± 0.155
20120617	56095.961	17.177 ± 0.045
20120626	56104.936	17.039 ± 0.036
20120708	56116.914	17.217 ± 0.052
20120709	56117.941	17.111 ± 0.038
20120712	56120.927	17.089 ± 0.047
20120717	56125.885	17.293 ± 0.043
20120717	56125.988	17.187 ± 0.038
20120726	56134.856	17.130 ± 0.039
20120802	56141.972	17.293 ± 0.044
20120803	56142.839	17.486 ± 0.044
20120803	56142.853	17.537 ± 0.043
20120807	56146.874	17.684 ± 0.034
20120815	56154.838	17.765 ± 0.035
20120819	56158.825	17.787 ± 0.035
20120827	56166.843	18.452 ± 0.038
20120906	56176.803	18.396 ± 0.036
20120910	56180.803	18.506 ± 0.036

Table 4.5: Final magnitudes of the transient from amateur astronomer observations.

Montarrenti Observatory kept observing the host of SNhunt133 in later years in order to catch other significant variations of luminosity in the nucleus. As shown in Figure 4.10, this never happened.

[6]https://www.gemini.edu/sciops/instruments/midir-resources/imaging-calibrations/fluxmagnitude-conversion

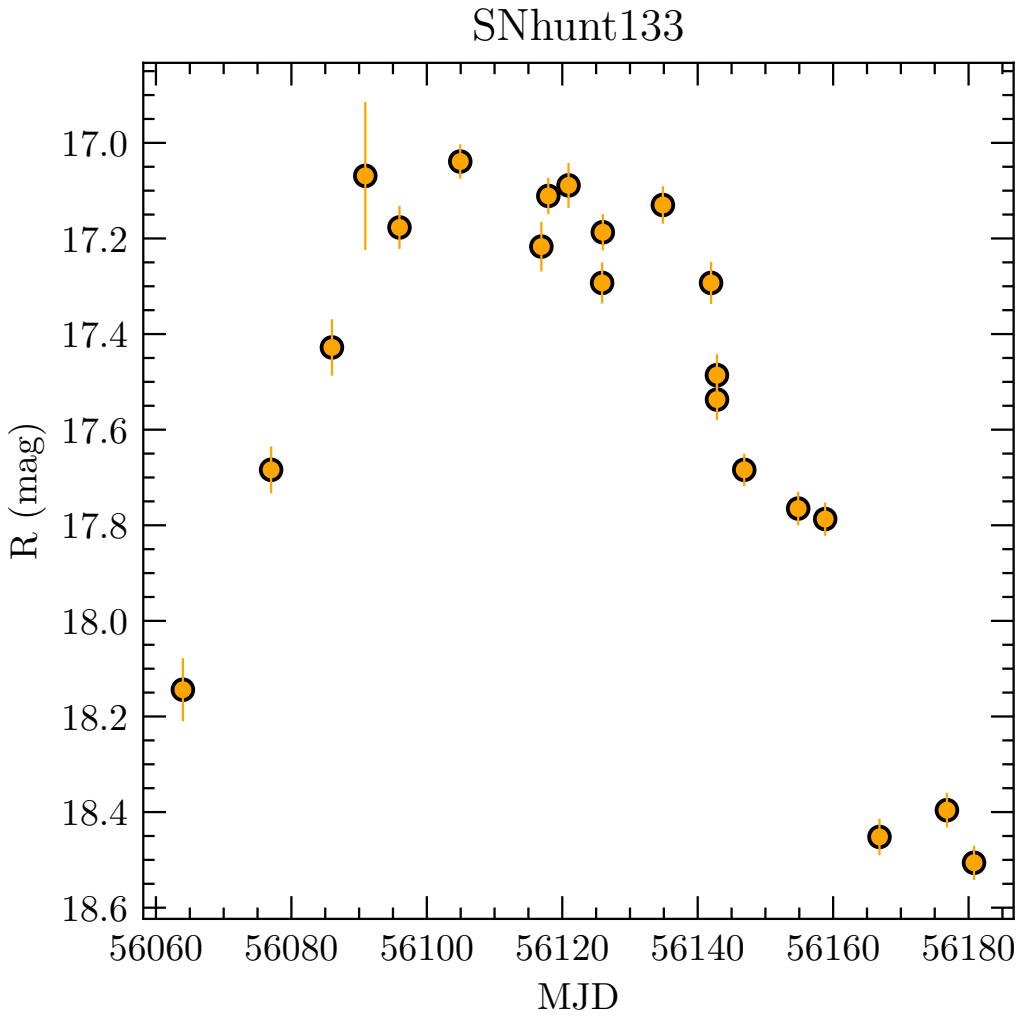

Figure 4.9: Light-curve obtained plotting the magnitudes calculated from amateur images with respect to time.

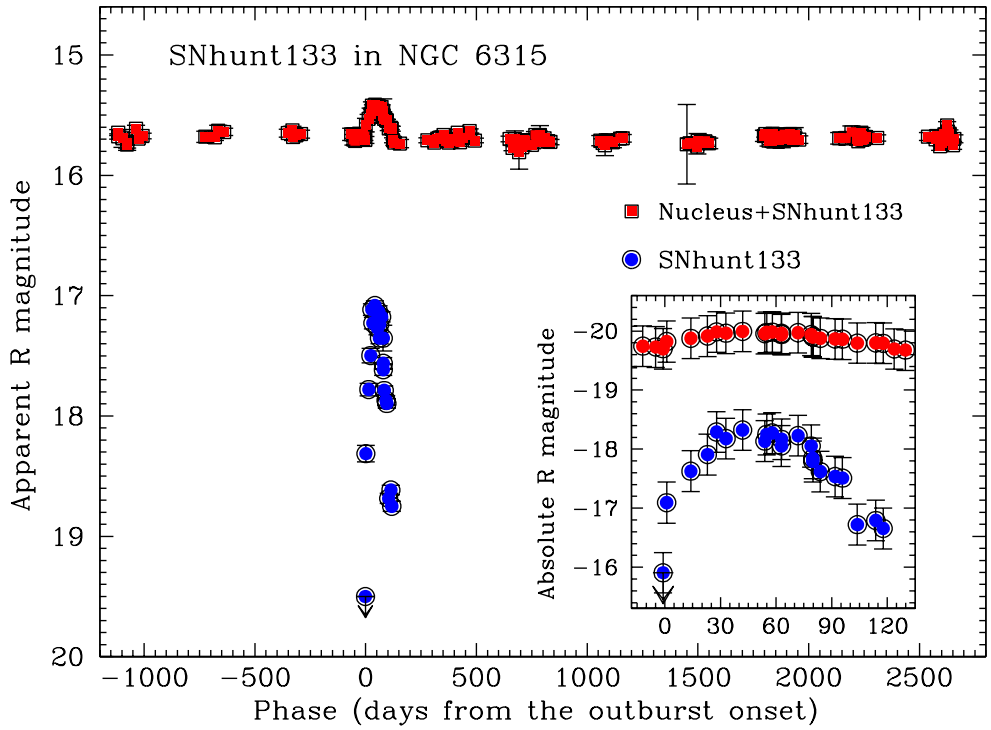

Figure 4.10: Light-curve of the nucleus of NGC 6315 in the last ten years. Magnitudes are derived from amateur astronomers with unfiltered observations and re-scaled to match professional observations (see text in Section 4.1.5). Red squares represent the composite magnitude of the galactic nucleus and of the transient, whereas blue dots represent the transient alone. The subplot in the right corner shows a blow-up of the absolute light-curve obtained from these points, in proximity of the maximum light.

4.1.6 Infrared data

Raw dithered IR images taken the same night in the same filter are median-combined to obtain a sky image using the task `imcombine` to be subtracted to individual image with `imarith`. Then, individual dithered sky-subtracted images are combined to a single target image with higher signal-noise ratio (S/N) with `imcombine`. The final image is finally astrometrised and the seeing is measured in the SNoOPy environment (see 4.1.2).
Since the template-subtraction procedure proved to be more efficient, in terms of lower errors, it is applied also to IR images with the same steps described in Section 4.1.4. As template, archival images of NGC6315 taken on the night of 1997 June 16$^{\rm th}$ from 2MASS All-Sky catalogue[7] were used. Instrumental magnitudes are calibrated as in previous sections, with the only difference that the poorly-known colour-term correction is not accounted for. Calibrated magnitudes are shown in Table 4.6 and plotted in Figure 4.11.

Date	MJD	J	H	K	Instrument
20120731	56139.000	16.462±0.028	15.464±0.030	15.702±0.037	NICS
20120819	56158.015	16.772±0.102	16.395±0.084	16.399±0.052	SOFI

Table 4.6: Infrared magnitudes of the transient obtained through template subtraction.

4.2 Light-curve analysis

The complete light-curve of SNhunt133 inclusive of both data collected by amateur astronomers and with professional telescopes (Tables 4.3, 4.5 and 4.6) is shown in Figure 4.11. It has a distinct peak, with a long ($\sim$ 50 days) rise to maximum light in the R band. Unfortunately, all observations in other bands are post-peak, but all of them show a regular decline. In the most well-sampled bands (B, V, R, I), the trace of a plateau can be seen around 50 days after maximum light.
The data analysis tool Alice (Asiago LIght Curve Environment, based on pyraf) was used to determine MJD and magnitude of the maximum in the R band, with the task `lsf`. Peak light happened on $\mathrm{MJD_{max}} = 56110.5 \pm 0.6$ days, that is to say, on July 2$^{\rm nd}$, 2012, with an apparent magnitude $M_{max}(R) = 17.07 \pm 0.03$ mag. The fit is repeated several times, adding and deleting points, in order to obtain a series of values, which are averaged to give the aforementioned results. Errors are determined as the standard deviation of the above measurements.

4.2.1 Light-curve decline

A measure of the decrease in magnitude 15 days after the peak, $\Delta_{15}(m)$, would have made for a good instrument of comparison of SNhunt133 with a Type Ia SN. Since the light-curve peak happened almost a month before the first multi-band observation, a calculation of the classical post-peak decline parameters of SNe Ia is impossible.

[7] https://irsa.ipac.caltech.edu/applications/2MASS/IM/interactive.html

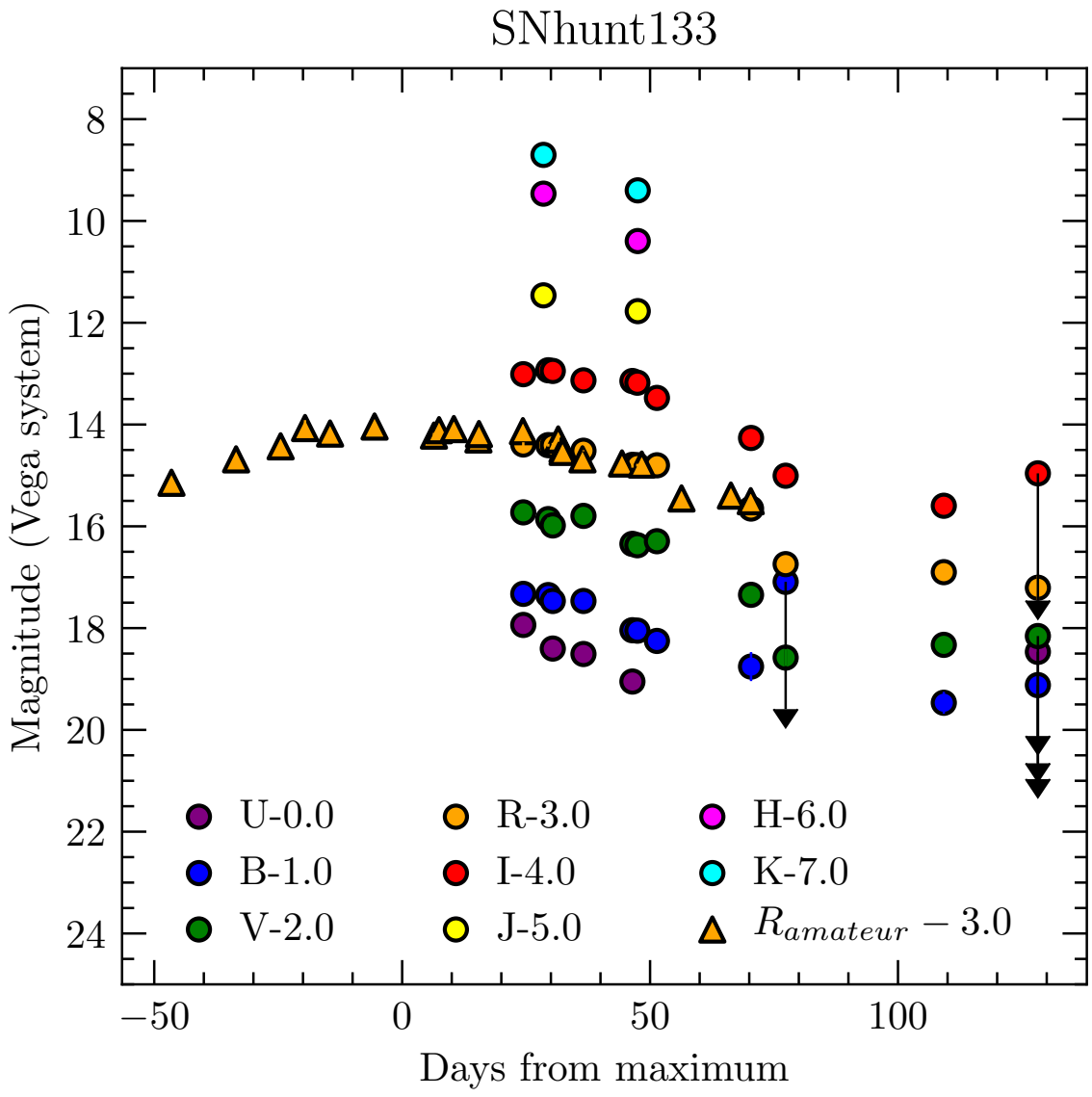

Figure 4.11: Final light-curve of SNhunt133 in optical (U, B, V, R, I) and IR (J, H, K) bands. Black arrows indicate upper limits.

ALICE task `lsf` is used to determine the decline slope in various bands, are reported in Table 4.7. It can be seen that U light declined the fastest, and R the slowest.

Band	Slope (mag/100 days)
U	4.77 ± 0.65
B	2.70 ± 0.21
V	3.20 ± 0.22
R	2.68 ± 0.12
I	3.49 ± 0.33

Table 4.7: Light-curve slope of SNhunt133 in various bands.

4.2.2 Colour curves

I calculate the evolution in colour of SNhunt133 computing $U - B$, $B - V$, $V - R$ and $R - I$. Results are listed in Table 4.8, where errors the root sum of squares and missing values stem from the lack of measure of one or both magnitudes for that epoch.

Colour curves are plotted in Figure 4.12. They show an evolution towards a redder colour in

Days (from peak)	$U - B(mag)$	$B - V(mag)$	$V - R(mag)$	$R - I(mag)$
24.430	-0.389 ± 0.162	0.601 ± 0.073	0.334 ± 0.066	0.381 ± 0.062
29.465	-	0.493 ± 0.074	0.453 ± 0.058	0.471 ± 0.049
30.380	-0.065 ± 0.150	0.484 ± 0.070	0.575 ± 0.071	0.461 ± 0.091
36.565	0.042 ± 0.080	0.672 ± 0.061	0.280 ± 0.045	0.383 ± 0.040
46.440	0.008 ± 0.157	0.697 ± 0.104	0.553 ± 0.078	0.647 ± 0.082
47.440	-	0.678 ± 0.090	0.573 ± 0.065	0.621 ± 0.072
51.385	-	0.959 ± 0.119	0.492 ± 0.067	0.324 ± 0.064
70.365	-	0.410 ± 0.296	0.695 ± 0.083	0.387 ± 0.101
77.345	-	-	0.837 ± 0.202	0.737 ± 0.163
109.240	-	0.138 ± 0.270	0.428 ± 0.202	0.305 ± 0.190

Table 4.8: Colour evolution with respect to maximum light. Missing values derive from the impossibility of measuring one or both magnitudes at the time.

all bands, except for the last point in curves V-R and R-I and the last two points in B-V, which are bluer. Nevertheless, they have large error bars, thus the measure bears less significance.

4.2.3 Absolute light-curve

The absolute light-curve shown in Figure 4.13 is calculated in the R band as $R = r - (m - M) - A_R$, where r is the apparent R magnitude, $(m - M) = 35.08 \pm 0.15$ mag is the distance modulus and $A_R = 0.379 \pm 0.027$ mag is the total absorption at R wavelength. Distance modulus and total absorption absorption are defined in Sections 3.2 and 3.3. Error bars are calculated

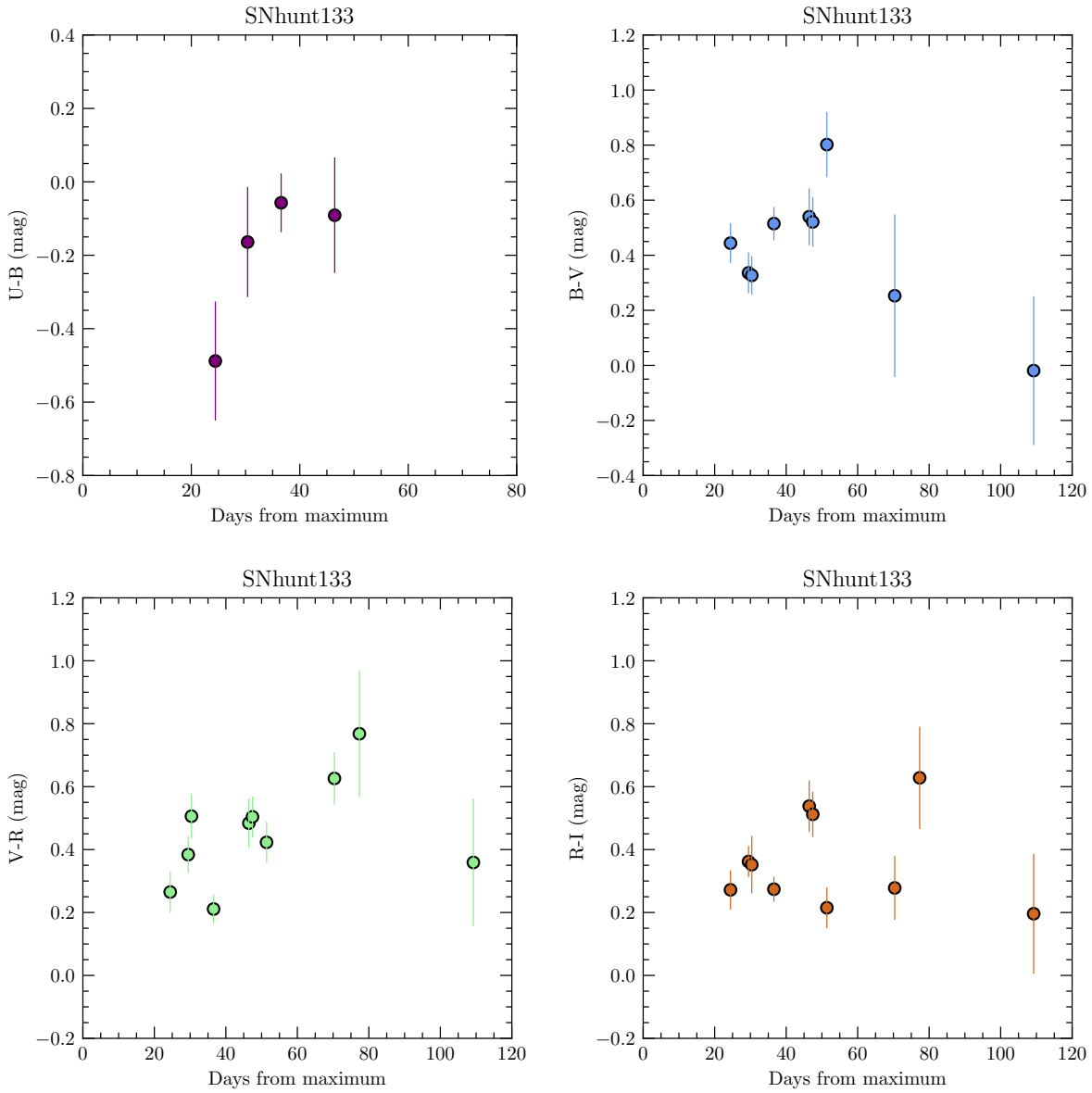

Figure 4.12: Colour curves

through standard error propagation.

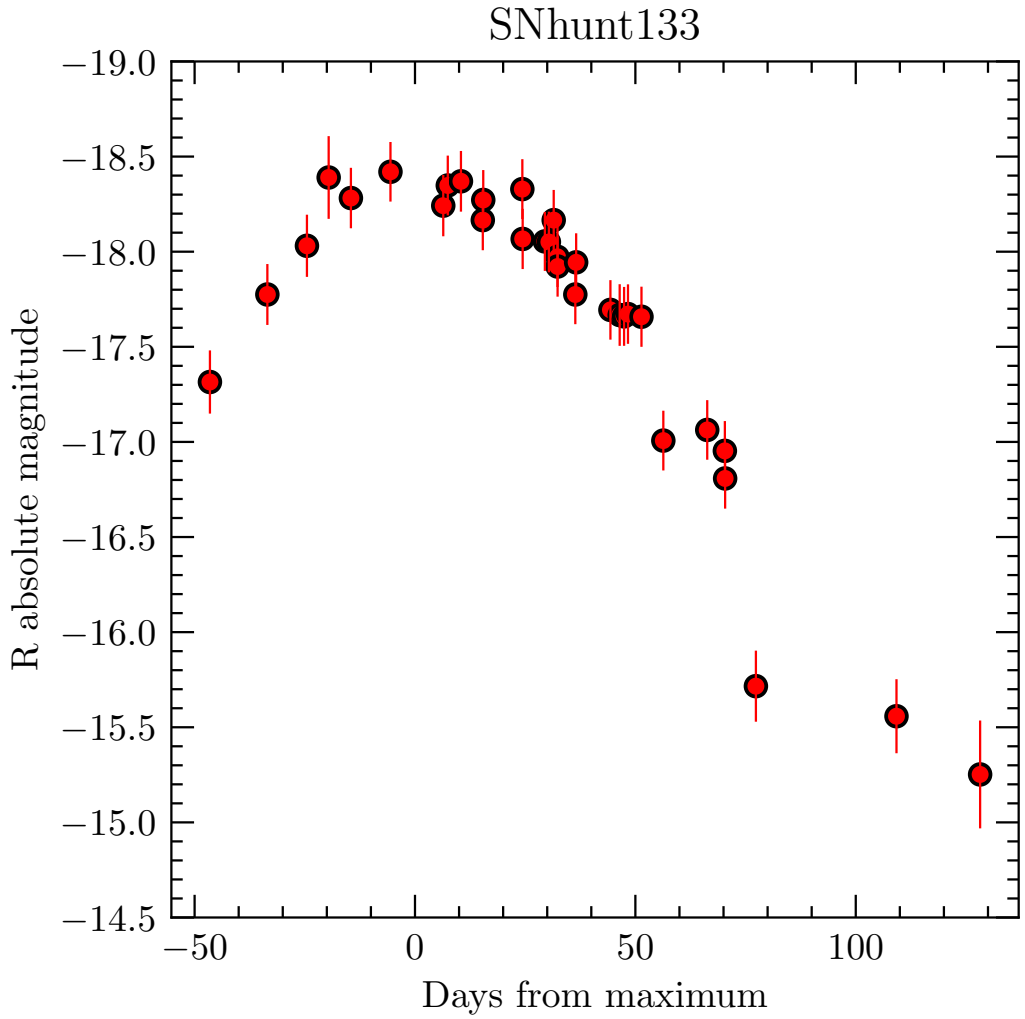

Figure 4.13: Absolute light-curve of SNhunt133 in R band.

4.2.4 Pseudo-bolometric light-curve

The pseudo-bolometric light-curve is computed converting optical absorption-corrected magnitudes in fluxes, making use of Allen's zero-points [Allen and Cox, 2001]. The procedure calculates the average flux for each band and fits a black-body. If a point is missing for a given band (upper limits are not taken into consideration, either), its contribution is estimated by interpolating the previous and subsequent observed points assuming the colour does not change

from the last available observation. All flux contribution is truncated outside the external points. The obtained fluxes are then integrated using the trapezoidal rule and converted to luminosity using the distance modulus.
The pseudo-bolometric light-curve obtained with this procedure is shown in Figure 4.14.

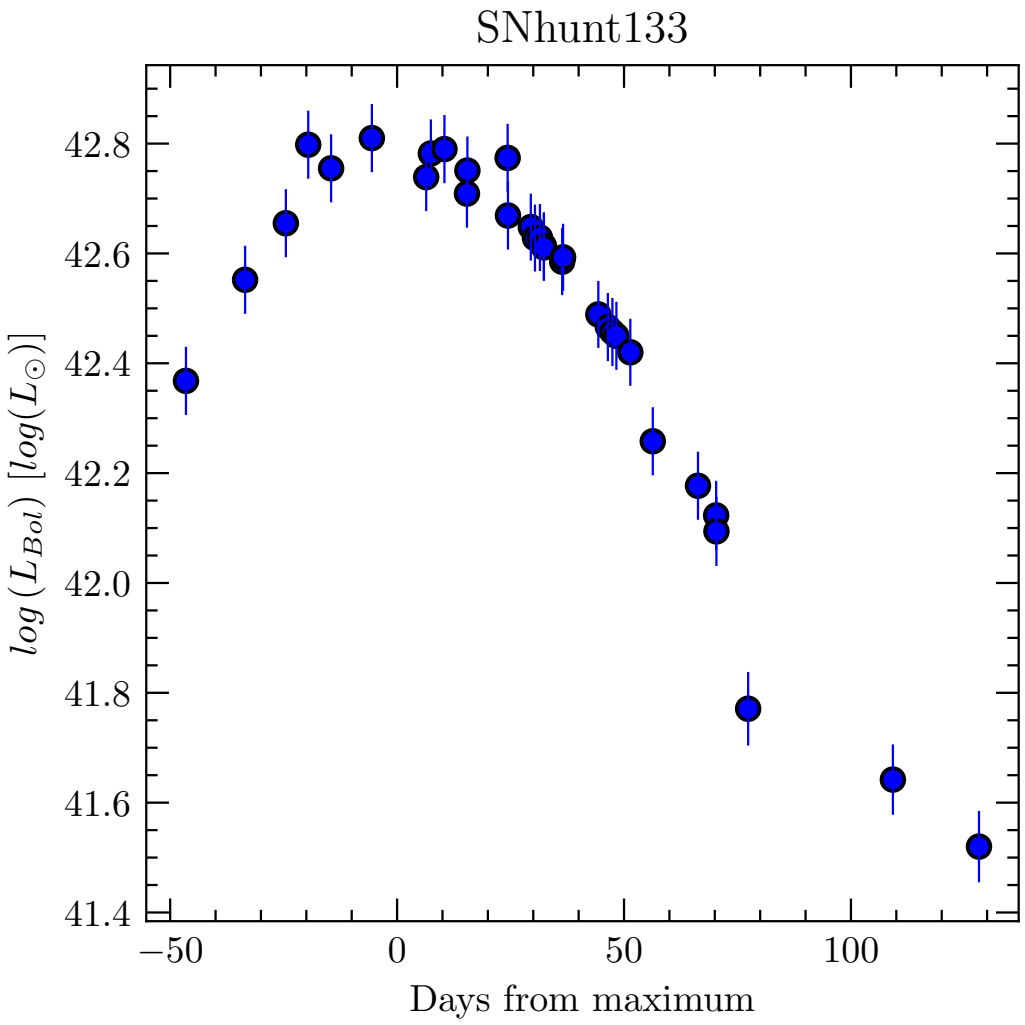

Figure 4.14: Bolometric curve of SNhunt133 based on the R band.

CHAPTER

5

SPECTROSCOPY

Spectra were taken with the following instruments (characteristics summarised in Table 5.1):

- AFOSC, mounted on Copernico 1.82 m telescope in Asiago. Grisms GR04 and VPH6.
- XShooter, mounted on Unit Telescope 2 (UT2, Kueyen) of the Very Large Telescope (VLT) at the Paranal Observatory.
- SofI (Son of ISAAC), mounted on NTT in La Silla. Grism GB.
- eBOSS (Extended Baryon Oscillation Spectroscopic Survey) of the Sloan Digital Sky Survey (SDSS).

Date	MJD	Days from R maximum	Telescope	Instrument	Grism	Resolution	Spectral range [Å]
20110526	55707	-403	SDSS	eBOSS	-	1528	3600-10400
20120726	56134.911	+24	Copernico 1.82 m	AFOSC	GR04+VPH6	451 + 413	3360-7740 + 4500-10000
20120731	56139.885	+29	Copernico 1.82 m	AFOSC	GR04+VPH6	458 + 390	3360-7740 + 4500-10000
20120817	56156.869	+46	Copernico 1.82 m	AFOSC	GR04+VPH6	452 + 408	3360-7740 + 4500-10000
20120818	56157.874	+47	Copernico 1.82 m	AFOSC	GR04+VPH6	448 + 418	3360-7740 + 4500-10000
20120819	56158.038	+48	NTT	SOFI	GB	438	9500-16400
20120819	56158.060	+48	VLT	XSHOOTER	PS6-R	2175	3000–25000
20120910	56180.787	+70	Copernico 1.82 m	AFOSC	GR04+VPH6	450 + 418	3360-7740 + 4500-10000
20120917	56187.867	+77	Copernico 1.82 m	AFOSC	GR04	400	3360-7740
20121019	56219.761	+109	Copernico 1.82 m	AFOSC	GR04	451	3360-7740

Table 5.1: Observation date and instrumental configuration of spectral data.

5.1 Preliminary reduction

First of all, raw spectra are trimmed and bias and flat correction are applied. As with photometric data, this is done through tasks `ccdproc`, `zerocombine` and `flatcombine`.
In Figure 5.1 examples of corrected spectra are shown.

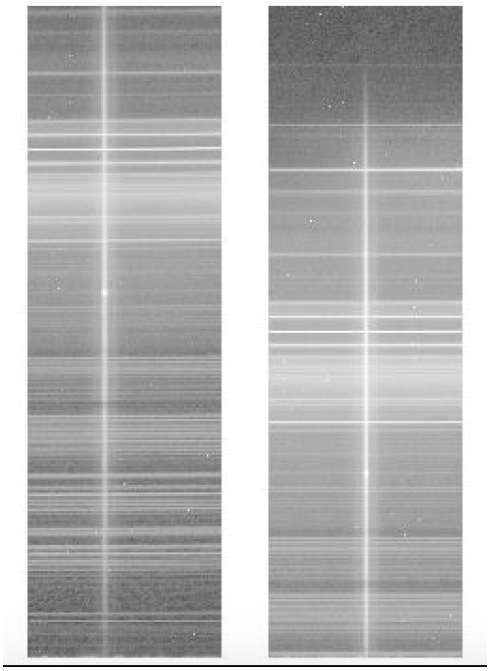

Figure 5.1: Left: Spectrum of SNhunt133 taken with AFOSC equipped with grism VPH6. Right: Spectrum of SNhunt133 taken with AFOSC equipped with grism GR04.

In order to obtain a calibrated spectrum, spectra of spectro-photometric standard stars, as well as that of standard lamps are also necessary. GD50 or BD+28d4211 are selected as preferential spectro-photometric standards. Regarding the lamps, combinations of Helium-Neon, Mercury-Cadmium and Thorium are used.
Then, the spectra of astrophysical sources are extracted at a position specified by the user. The task `apall` in IRAF package CTIOSLIT is apt for carrying this out. Lamp spectra are instead extracted through task `apsum`.
Lamp spectra are then calibrated in wavelength, using the task `identify`, associating the known wavelength for each emission line. The lamp now calibrated is used as a reference for wavelength calibrating the scientific spectra using the tasks `refspec` and `dispcor`.
The spectro-photometric standard stars are used to calibrate in flux: the star flux is compared to stellar flux tables provided by ESO[1] using the task `standard`. The task `sensfunc` is used to create the instrumental sensitivity function, taking care of cutting off the atmospheric absorption from the curve. With task `calib` the curve is applied to both the transient and the standard itself.

[1] https://www.eso.org/sci/observing/tools/standards/spectra/stanlis.html

The standard is also used to eliminate telluric bands. The telluric band spectrum (which has unit value everywhere except at the position of the main telluric bands) is then applied to the transient through task `telluric`, where it is shifted and scaled in order to erase the bands.
Spectra taken the same night with different grisms are combined, in order to produce a single spectrum with a wider spectral range.
In Figure 5.2 a step of the combination process is shown.

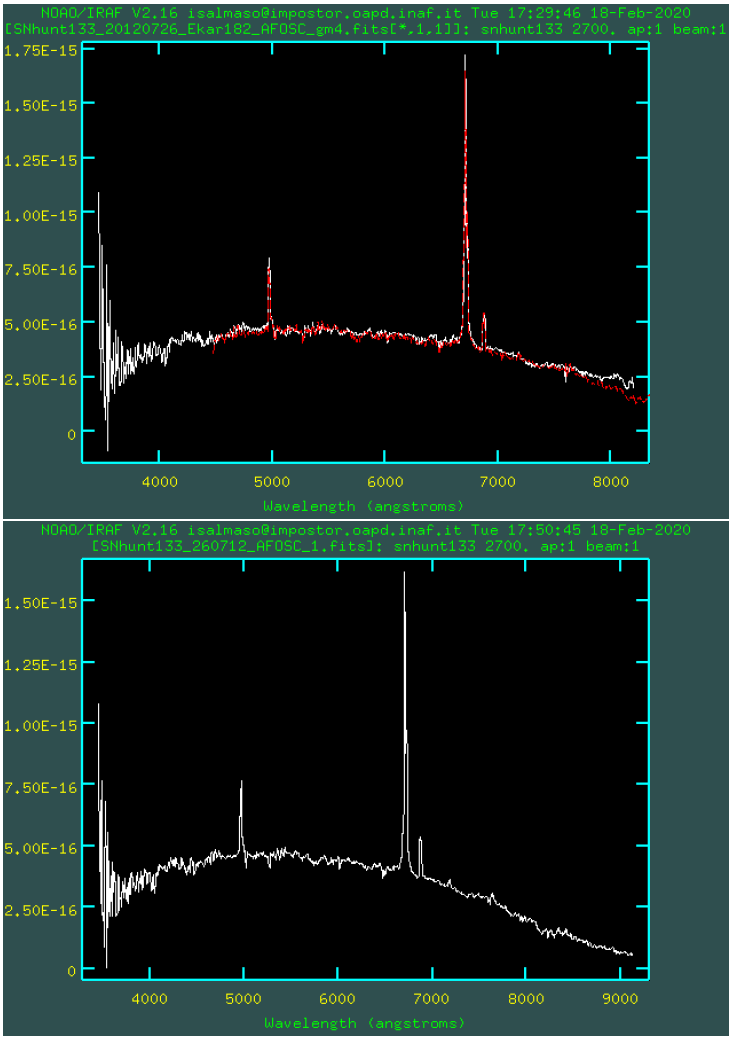

Figure 5.2: Top: Calibrated spectra of SNhunt133 obtained using AFOSC VPH6 (red) and Gr04 (white). Bottom: Resulting spectrum obtained combining VPH6 and Gr04.

The spectra are finally checked with available broadband V photometry, and in case of a discrepancy, a correction factor is applied to the flux of the spectrum.
Spectra are then corrected for extinction with IRAF task `dered`, using the $E(B-V)$ derived in Section 3.3.
Spectra are also shifted using the redshift in 3.2 to display their features at rest wavelength. The

shift is done through IRAF task `dopcor`. The resulting spectra are plotted in Figure 5.3, whilst line identification is performed in Figure 5.4 on the optical side of the XShooter spectrum.
The spectrum taken 109 days after peak light shows a red continuum, in contrast with the others. Moreover, the transient at this epoch should have disappeared, or at least have considerably dimmed, and the spectrum should be similar to the galactic one. A check with broadband photometry in bands B (18.046 mag), V (17.366 mag), R (16.946) mag) and I (16.965 mag) highlights a discrepancy between magnitudes calculated from the spectrum and from photometry (cfr. Table 4.1). This is most likely due to the fact that the object exited from the slit during observation, causing the loss of some flux with a dependence on the wavelength. Therefore, the trend of the continuum of this particular spectrum should not be taken into consideration.

5.2 Infrared spectra

Infrared spectra follow the same steps of preliminary reduction presented in Section 5.1, only with the difference of background subtraction. With IR spectra, four dithered images are taken and the background is subtracted to each other in couples, in order to obtain two bidimensional images with a positive and a negative trace. The negative trace is converted to positive values multiplying by -1. The resulting spectra are then combined into a single, clean spectrum. They are then calibrated with the same passages followed in Section 5.1.
The XShooter spectrum, instead, is calibrated using the available ESO pipeline.
Clean spectra taken with XShooter and SofI are showed in Figure 5.5.

5.3 Line ratios

Here I measure flux, peak intensity and wavelength of several emission lines from de-reddened and reshift-corrected spectra, fitting emission lines with either a Gaussian or a Lorentzian function. Results are listed in Table 5.2. In some cases, the continuum is too noisy to detect a particular line.

Date	MJD	[O II] 3727			Hγ		
		Intensity ($\cdot 10^{-16}$)	Flux ($\cdot 10^{-15}$)	λ [Å]	Intensity ($\cdot 10^{-16}$)	Flux ($\cdot 10^{-15}$)	λ [Å]
20110526	55707	8.229	4.332	3727.08	4.780	1.282	4340.11
20120726	56134.911	5.130	0.780	3725.69	5.460	0.454	4343.00
20120731	56139.885	< 2.721	< 4.101	-	< 1.515	< 2.283	-
20120817	56156.869	7.309	1.300	3724.99	< 0.434	< 0.452	-
20120818	56157.874	< 2.518	< 2.830	-	< 0.699	< 0.785	-
20120819	56158.038	7.156	1.390	3726.66	12.90	1.340	4340.83
20120910	56180.787	6.440	1.510	3724.31	0.5325	0.479	4337.74
20120917	56187.867	2.220	2.551	3727.40	0.929	0.809	4340.79
20121019	56219.761	< 1.999	< 2.025	-	0.885	0.712	4337.65

Date	MJD		Hβ			[O III] 5007	
		Intensity ($\cdot 10^{-16}$)	Flux ($\cdot 10^{-15}$)	λ [Å]	Intensity ($\cdot 10^{-16}$)	Flux ($\cdot 10^{-15}$)	λ [Å]
20110526	55707	12.52	4.119	4861.33	1.899	0.829	5006.62
20120726	56134.911	8.472	4.530	4862.41	< 0.136	< 0.188	-
20120731	56139.885	3.401	4.653	4863.38	< 1.079	< 1.626	-
20120817	56156.869	2.706	2.900	4860.74	< 0.284	< 0.296	-
20120818	56157.874	2.873	3.130	4858.91	< 0.127	< 0.142	-
20120819	56158.038	23.71	5.710	4861.62	1.478	0.286	5006.90
20120910	56180.787	2.745	3.088	4859.49	0.303	0.337	5005.47
20120917	56187.867	2.538	2.853	4862.90	0.540	0.631	5006.89
20121019	56219.761	2.881	2.880	4860.25	0.736	0.801	5005.82
Date	MJD		Hα			[N II] 6583	
		Intensity ($\cdot 10^{-16}$)	Flux ($\cdot 10^{-15}$)	λ [Å]	Intensity ($\cdot 10^{-16}$)	Flux ($\cdot 10^{-15}$)	λ [Å]
20110526	55707	35.02	21.74	6562.53	19.00	11.46	6583.26
20120726	56134.911	10.95	15.18	6563.119	5.335	9.347	6582.47
20120731	56139.885	12.64	19.68	6562.97	6.154	10.37	6583.42
20120817	56156.869	6.077	8.950	6563.14	4.037	5.953	6583.86
20120818	56157.874	5.754	7.756	6564.80	3.246	4.488	6584.07
20120819	56158.038	52.02	23.86	6562.52	27.79	11.26	6583.18
20120910	56180.787	10.79	14.83	6563.73	6.392	8.467	6582.81
20120917	56187.867	14.36	18.46	6563.54	7.096	9.340	6584.35
20121019	56219.761	15.11	17.96	6563.38	7.886	8.978	6583.61
Date	MJD		[S II] 6716			[S II] 6731	
		Intensity ($\cdot 10^{-16}$)	Flux ($\cdot 10^{-15}$)	λ [Å]	Intensity ($\cdot 10^{-16}$)	Flux ($\cdot 10^{-15}$)	λ [Å]
20110526	55707	3.836	1.956	6716.40	4.111	2.083	6730.75
20120726	56134.911	1.327	2.098	6718.72	1.309	2.137	6731.21
20120731	56139.885	0.694	1.293	6716.43	1.697	3.114	6729.36
20120817	56156.869	0.990	1.552	6716.32	1.271	2.024	6731.05
20120818	56157.874	1.023	1.601	6715.55	1.116	1.802	6728.62
20120819	56158.038	6.090	2.161	6715.96	7.321	2.941	6730.68
20120910	56180.787	1.175	1.702	6715.04	1.779	2.758	6728.34
20120917	56187.867	1.364	1.791	6717.64	1.648	2.293	6731.15
20121019	56219.761	1.879	2.927	6717.29	1.963	2.792	6730.70

Table 5.2: Intensity, flux and central wavelength of emission lines. Missing values could not be evaluated because of the too-noisy continuum. Upper limits are evaluated from the RMS of the continuum around the position of the line, as $I = 3 \cdot RMS$ and $F = 1.0644 \cdot I \cdot FWHM(H\beta)$.

I then calculate flux line ratios $\log\left(\frac{[O\ III]\ 5007}{H\beta}\right)$, $\log\left(\frac{[N\ II]\ 6583}{H\alpha}\right)$ and $\log\left(\frac{H\beta}{H\alpha}\right)$ in Table 5.3. These are key tools to eventually evaluate novel AGN-like activity in the host galaxy core. The

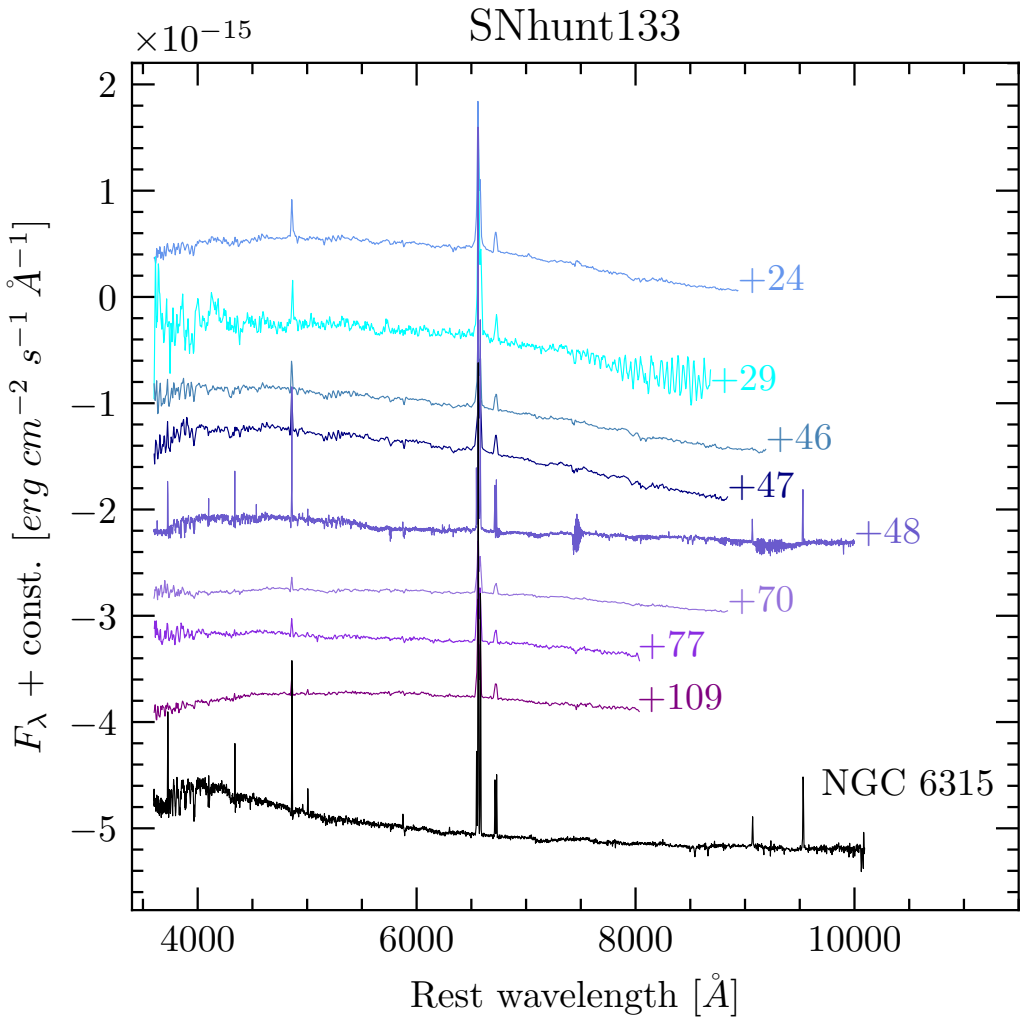

Figure 5.3: Spectral evolution of SNhunt133. Different epochs are marked alongside the respective spectrum. A comparison spectrum of NGC 6315 from SDSS is plotted in black.

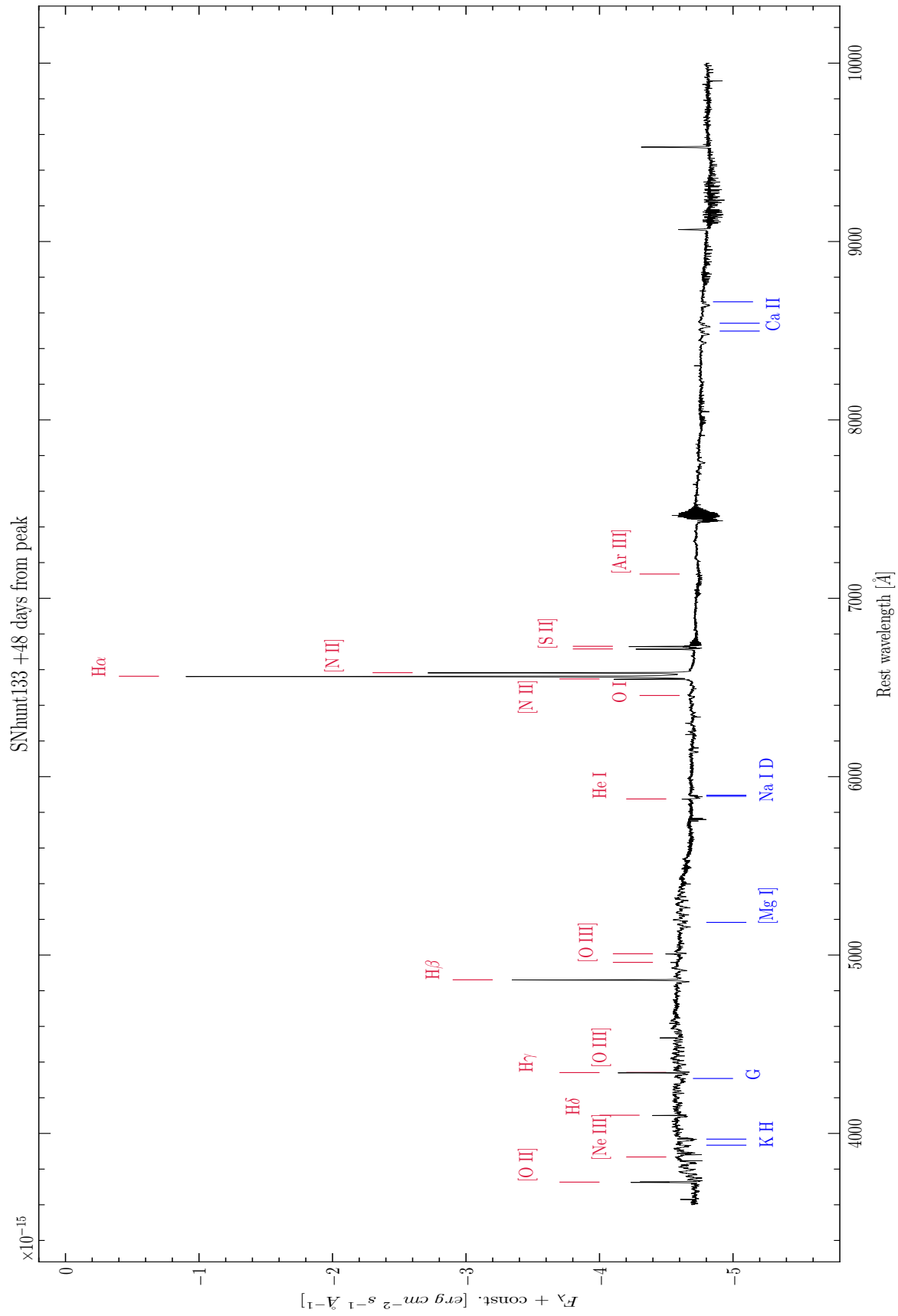

Figure 5.4: Identification of emission (red) and absorption (blue) lines on the XShooter spectrum, taken 48 days after maximum light.

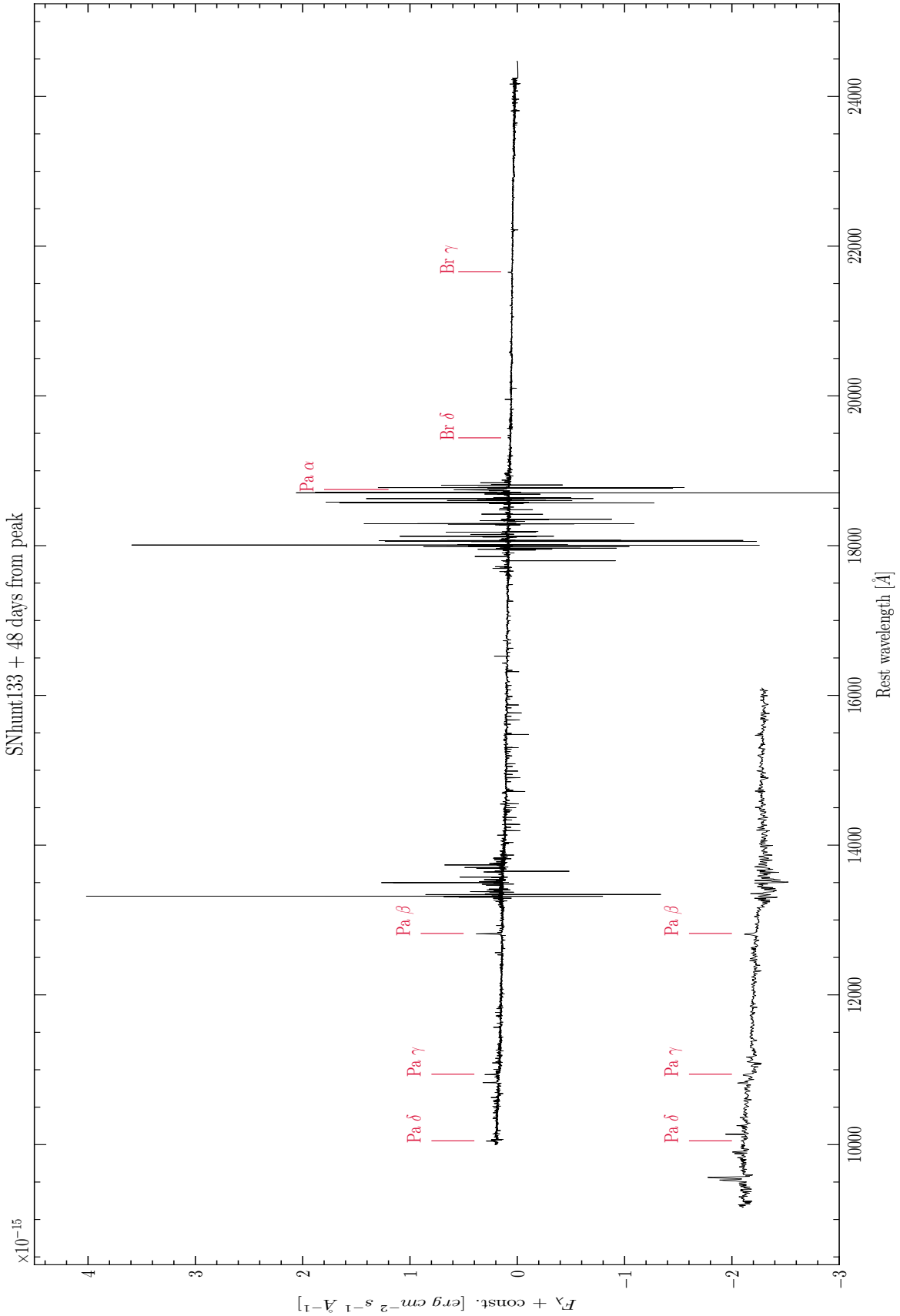

Figure 5.5: Infrared spectra of SNhunt133 taken 48 days after maximum light with instruments XShooter (upper spectrum) and SofI (lower spectrum). Hydrogen emission lines are indicated in red.

uncertainty on the flux is $\sigma_F = F \cdot \frac{\sigma_I}{I}$, where F is the flux, I is the intensity and $\sigma_I = RMS$ is the uncertainty on the intensity, with RMS calculated on the continuum close to the position of each line. Due to low S/N, occasionally the flux ratio could not be securely measured. In these cases, upper limits on the intensity are obtained measuring the RMS of the continuum and taking $I = 3 \cdot RMS$. Upper limits on the flux are calculated as $F = 1.0644 \cdot I \cdot FWHM(H\beta)$, having assumed the line has a Gaussian profile. From Figure 5.6, it is clear that the ratio of

Date	MJD	$\log\left(\frac{[O\ III]\ 5007}{H\beta}\right)$	$\log\left(\frac{[N\ II]\ 6583}{H\alpha}\right)$	$\log\left(\frac{H\beta}{H\alpha}\right)$
20110526	55707	-0.696 ± 0.026	-0.278 ± 0.002	-0.722 ± 0.004
20120726	56134.911	$< -2.0513 \pm 0.145$	-0.211 ± 0.013	-0.525 ± 0.006
20120731	56139.885	$< -0.657 \pm 0.146$	-0.278 ± 0.009	-0.626 ± 0.016
20120817	56156.869	$< -0.942 \pm 0.145$	-0.177 ± 0.016	-0.489 ± 0.013
20120818	56157.874	$< -1.140 \pm 0.145$	-0.238 ± 0.012	-0.394 ± 0.014
20120819	56158.038	-1.300 ± 0.007	-0.326 ± 0.001	-0.621 ± 0.004
20120910	56180.787	-0.962 ± 0.047	-0.243 ± 0.003	-0.681 ± 0.006
20120917	56187.867	-0.656 ± 0.109	-0.296 ± 0.003	-0.811 ± 0.010
20121019	56219.761	-0.556 ± 0.063	-0.301 ± 0.003	-0.795 ± 0.011

Table 5.3: Line ratios calculated for different epochs from fluxes shown in Table 5.2. When a line was not visible, a lower limit was calculated using the RMS of the continuum (see text). Errors are calculated through standard error propagation considering $\sigma_F = F \cdot \frac{\sigma_I}{I}$ and $\sigma_I = RMS_{continuum}$.

$\log\left(\frac{[O\ III]\ 5007}{H\beta}\right)$ was lower than the average value of the galactic nucleus within the early phases of SNhunt133. It then increased until reaching the value showed by the nucleus towards the end of the observative campaign. The ratio $\log\left(\frac{[N\ II]\ 6583}{H\alpha}\right)$, instead, does not show a clear evolution with time, remaining almost constantly lower than the average value except for the observation on August 19^{th}, when a higher value is measured.
The ratio $\log\left(\frac{H\beta}{H\alpha}\right)$ is affected by reddening, since the two lines are significantly apart. The evolution of the ratio in Figure 5.6 shows an increase in the early phases and a decline in the last observations, indicating a progressive, but not significantly high, reddening of the source.

5.4 Template subtraction

In order to find spectral signatures of a stellar transient (e.g. a SN or TDE) embedded in the spectrum of the galaxy core, we should attempt to completely remove the host galaxy contamination from the optical spectra presented in Figure 5.3. To highlight the spectral characteristics of SNhunt133, I subtract to these spectra a template spectrum taken several years before the transient appeared. The template spectrum was taken with eBOSS and it is also shown in Figure 5.3, labelled as "NGC 6315".
To operate the subtaction, a PYRAF pipeline is used [Turatto, 2020]. It assumes that the spectrum of the galactic nucleus is constant and that the relative intensity of the lines of the nucleus

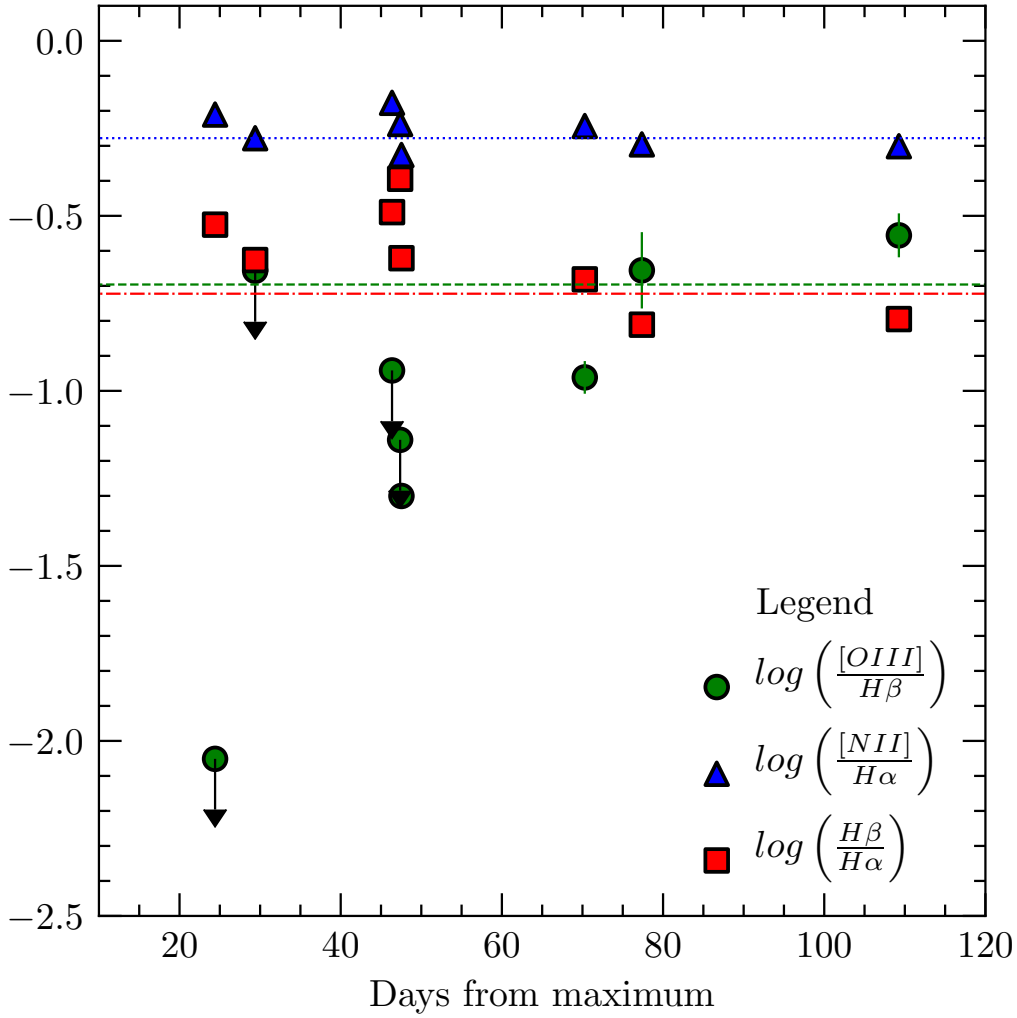

Figure 5.6: Evolution of line ratios with respect to the day of maximum light. The lines indicate the values for NGC 6315 of log([O III] 5007/Hβ) (dashed, green), log([N II] 6584/Hα) (dotted, blue) and log(Hβ/Hα) (dashed-dotted,red).

does not change with time. It degrades the spectrum, between the template and the analysed one, with the best resolution to the resolution of the other; then, the template spectrum is normalised so that the [S II] $\lambda\lambda$ 6716 – 6731 Å lines have the same intensity of the ones of the analysed spectrum. Convoluted spectra are then subtracted and line profiles are de-convoluted to give the final template-subtracted spectrum of the transient.
Resulting spectra are plotted in Figure 5.7.

Although most of the host galaxy flux has been removed, the difference spectra show some

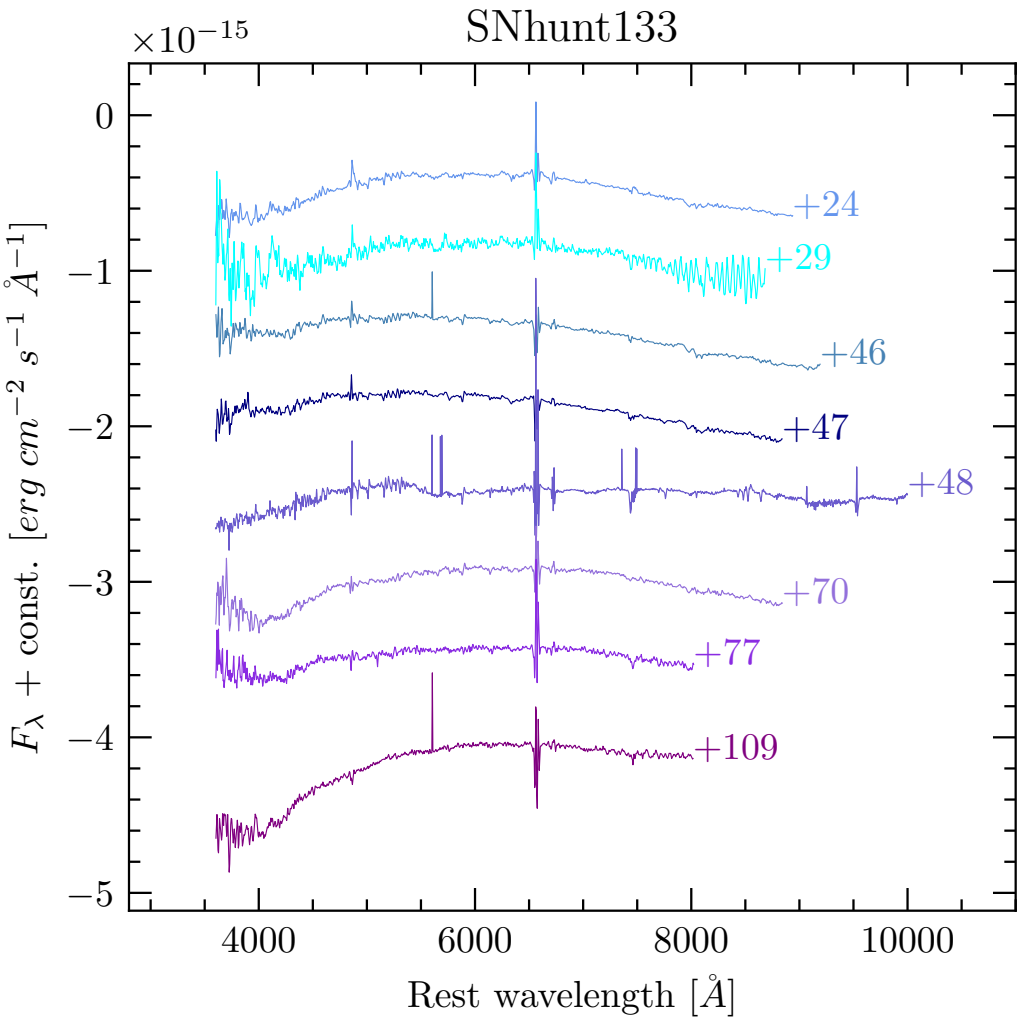

Figure 5.7: Spectral evolution of SNhunt133 once the galactic component has been subtracted (see text in Section 5.4). Different epochs are marked alongside the respective spectrum.

residual contamination of the original galaxy narrow lines. However, the spectra in Figure 5.7 show a clear temperature trend, with earlier spectra being hotter, whilst no broad features usu-

ally observed in stellar transients are detectable. This is consistent with the evolution of the Balmer ratio discussed in Section 5.3. It must also be noted that the spectrum labelled "+109" is affected by the same flux loss denoted in Section 5.1, so that the colour displayed by the continuum is not reliable. In particular, we do not see any clear SN feature over the evolution of SNhunt133, neither the classical broad lines (e.g. He II 4686) frequently observed in a TDE.

CHAPTER

6

DISCUSSION AND CONCLUSIONS

The classification of SNhunt133 was debated since its discovery, with a first classification spectrum indicating AGN-like variability [McCrum et al., 2012], and further observations pointing towards a TDE [Drake, 2012]. In this thesis, I analysed the spectro-photometric data of SNhunt133 in order to characterise it. In this final chapter, I discuss the obtained results and draw conclusions.

In Figure 6.1, a comparison of the absolute light-curve of SNhunt133 with those of other different transient is shown. The transients considered for this comparison are a regular Type Ia SN (2005cf [Wang et al., 2009]), a regular Type Ib SN (2009jf [Bianco et al., 2014]), a regular Type Ic SN (2007gr [Bianco et al., 2014]), a Ic-BL SN (2002ap [Bianco et al., 2014]) and a TDE (PTF09ge [Arcavi et al., 2014]).
SN peak magnitudes range between -17.7 and -19.3 (B) (see Sections 1.1.2 and 1.1.3), whilst TDE peak magnitude are extended from -19 to -21 (R) (see Section 2.3).
The peak magnitude of SNhunt133 is consistent within the range of variability of all these transients, therefore a distinction will be based on the shape of the light-curve.
In particular, the rise time of SNhunt133 is much slower than the typical SN. This is clearly displayed in Figure 6.1, where the light-curve of SNhunt133 is wider than the others. It is true that SLSNe have a longer rise time (e.g. [Lunnan et al., 2016]), but SLSNe have absolute peak magnitudes < -20.5 mag, which is inconsistent with SNhunt133. Moreover, Type Ia SNe show a secondary peak in the I band around 30 days after maximum light, whereas SNhunt133 declines in all bands.
Furthermore, the difference is even more evident comparing the spectrum of SNhunt133 to spectra of typical SNe at the same evolutionary phase. In Figure 6.2 such a comparison is shown with the same SNe of the photometric comparison dataset. The spectrum of SNhunt133

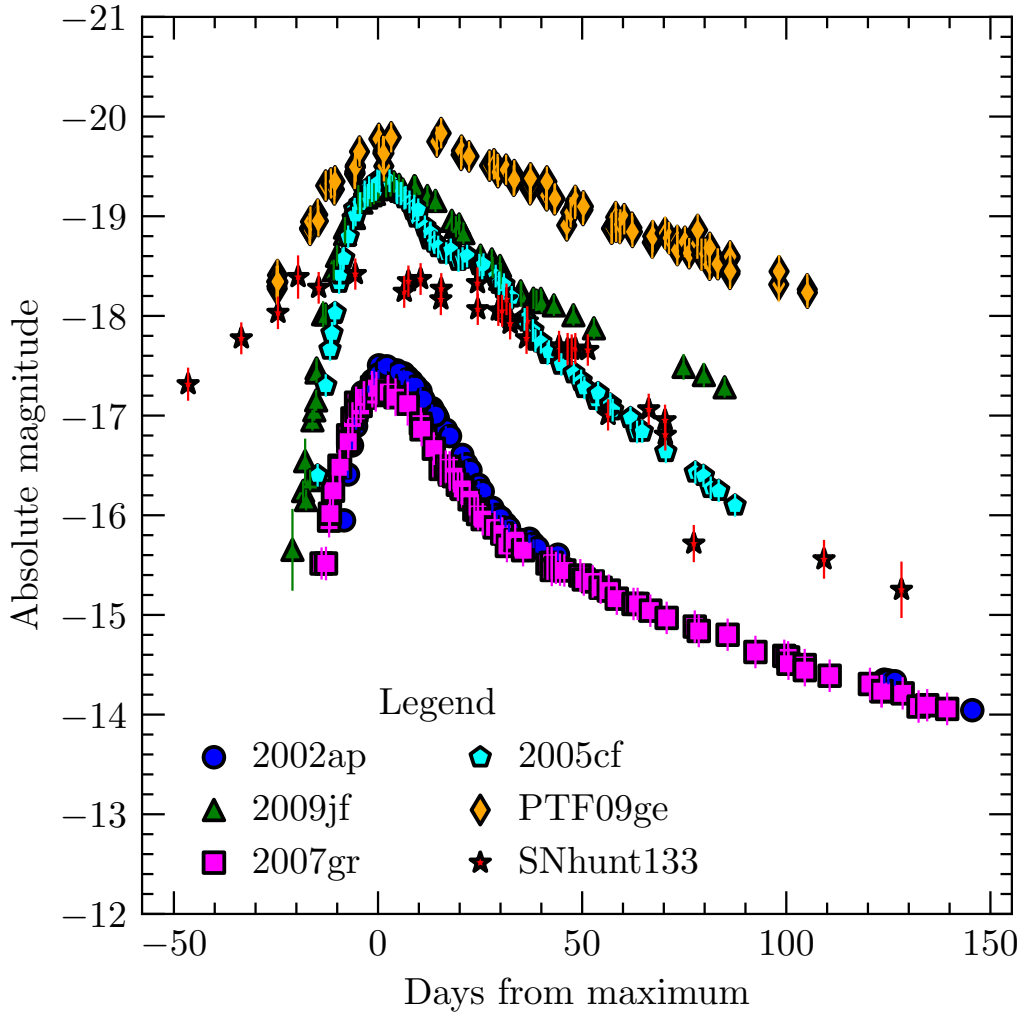

Figure 6.1: Light-curve comparison of SNhunt133 with different transients. All object are displayed in their R absolute magnitude except for PTF09ge, for which the absolute r magnitude, re-scaled to the Vega system, is plotted.

has only narrow lines (residual of the galaxy), in contrast to the broader lines of SNe. It is true that type II-n SNe have narrow lines, but their Hα is resolved, whereas in the case of SNhunt133 it is blended with [N II], even in the XShooter spectrum. This means that the observed Hα is a residual of the host galaxy. The continuum of SNhunt133 is also redder and therefore colder than the average SN at the same phase.

After these considerations, a TDE seems to be more compatible with SNhunt133, since it has a broader light-curve. The comparison with spectra of several TDEs, hence, is crucial to determine a likeness.

A comparison of the spectra of four TDEs (ASASSN-14li [Holoien et al., 2016], PTF09djl [Arcavi et al., 2014], ASASSN-14ae [Holoien et al., 2014] and ASASSN-15lh [Dong et al., 2016]) with SNhunt133 is shown in Figure 6.3. Although TDE spectra tend to be quite diverse, they have very blue continua and broad lines, especially of He II. Neither of these features, however, is detected in SNhunt133.

The values of $\log\left(\frac{[O\ III]\ 5007}{H\beta}\right)$ and $\log\left(\frac{[N\ II]\ 6583}{H\alpha}\right)$ (Table 5.3) can be plotted one versus the other in the so-called *BPT diagram* [Baldwin et al., 1981]. It is a diagnostic instrument which has $\log\left(\frac{[N\ II]\ 6583}{H\alpha}\right)$ on the x axis and $\log\left(\frac{[O\ III]\ 5007}{H\beta}\right)$ on the y axis. The area is divided in three regions which delimit line ratios characteristic of star-forming galaxies, composite galaxies (which show weak Seyfert signature) and AGN. The division between star-forming and composite galaxies is

$$log\left(\frac{[O\ III]\ 5007}{H\beta}\right) = \frac{0.61}{log\left(\frac{[N\ II]\ 6583}{H\alpha}\right) - 0.05} + 1.3$$

as reported by [Kauffmann et al., 2003], whereas the division between composite galaxies and AGN is

$$log\left(\frac{[O\ III]\ 5007}{H\beta}\right) = \frac{0.61}{log\left(\frac{[N\ II]\ 6583}{H\alpha}\right) - 0.47} + 1.19$$

as given by [Kewley et al., 2001].

The BPT diagram of SNhunt133 is shown in Figure 6.4, where each point represent a measurement of the line ratios at different epoch. The evolution with time of $\log\left(\frac{[O\ III]\ 5007}{H\beta}\right)$, $\log\left(\frac{[N\ II]\ 6583}{H\alpha}\right)$ and $\log\left(\frac{H\beta}{H\alpha}\right)$ is shown in Figure 5.6.

The BPT diagram indicates NGC 6315 as a star-forming galaxy. SNhunt133 shows an evolution in the diagram, from lower to higher values of $\log\left(\frac{[O\ III]\ 5007}{H\beta}\right)$ vs. $\log\left(\frac{[N\ II]\ 6583}{H\alpha}\right)$. It only passes the limit between star-forming and composite once, but the corresponding measure is only an upper limit, therefore bearing less significance. In any case, it is clear that SNhunt133 did not show any strong AGN-like behaviour.

In conclusion, from this analysis it is difficult to pinpoint a precise match for SNhunt133. Its light-curve and spectral evolution do not resemble the typical behaviour of a SN.

Despite the fact that SNhunt133 shows a light-curve similar to a TDE, it differs significantly in the spectrum. Even the latest spectra of SNhunt133 (see Figure 5.3) show a featureless continuum, with no clear lines of He, H or metals. A remote possibility is that SNhunt133 is a peculiar TDE with low temperature, a case which has not been observed yet.

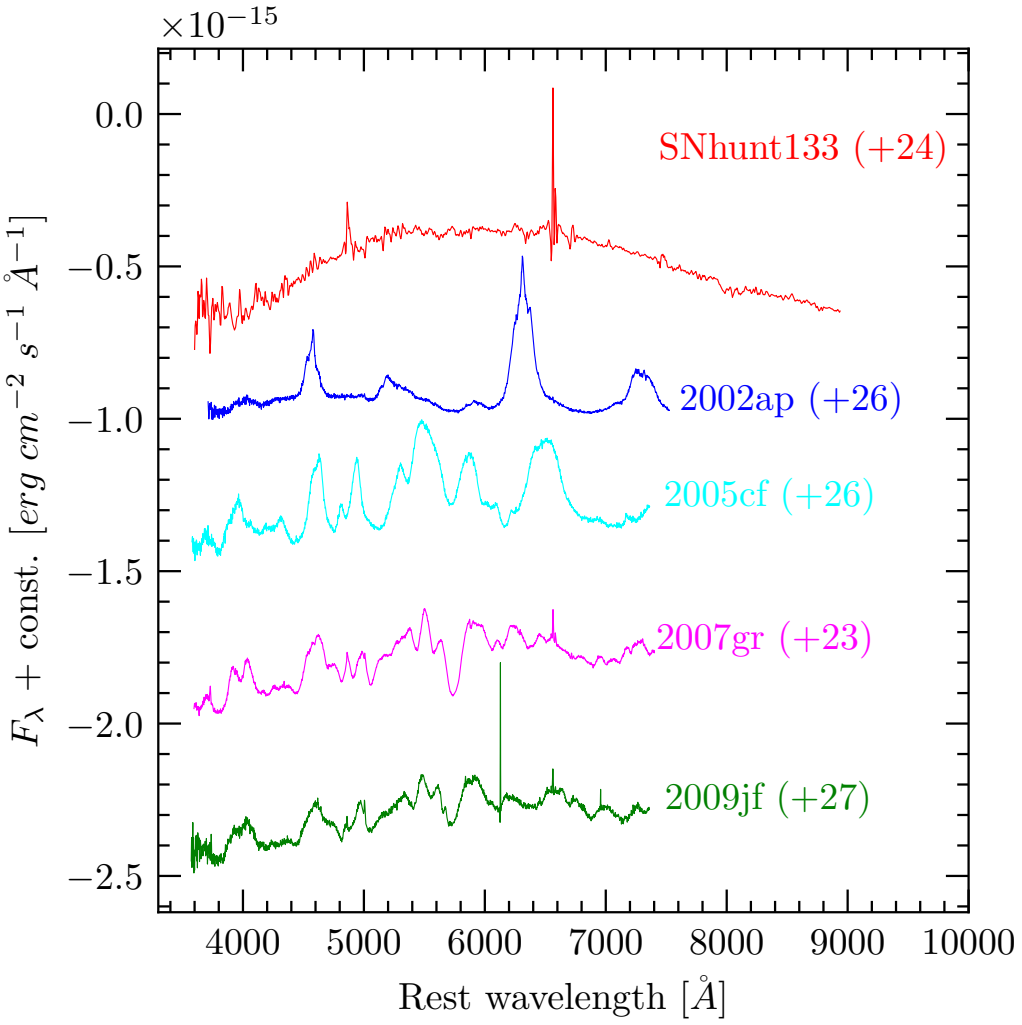

Figure 6.2: An early spectrum of SNhunt133 is compared to spectra of different SNe in a similar phase. The sample of comparison is comprehensive of a regular Type Ia SN (2005cf [Wang et al., 2009]), a regular Type Ib SN (2009jf [Modjaz et al., 2014]), a regular Type Ic SN (2007gr [Modjaz et al., 2014]) and a Ic-BL SN (2002ap [Modjaz et al., 2014]).

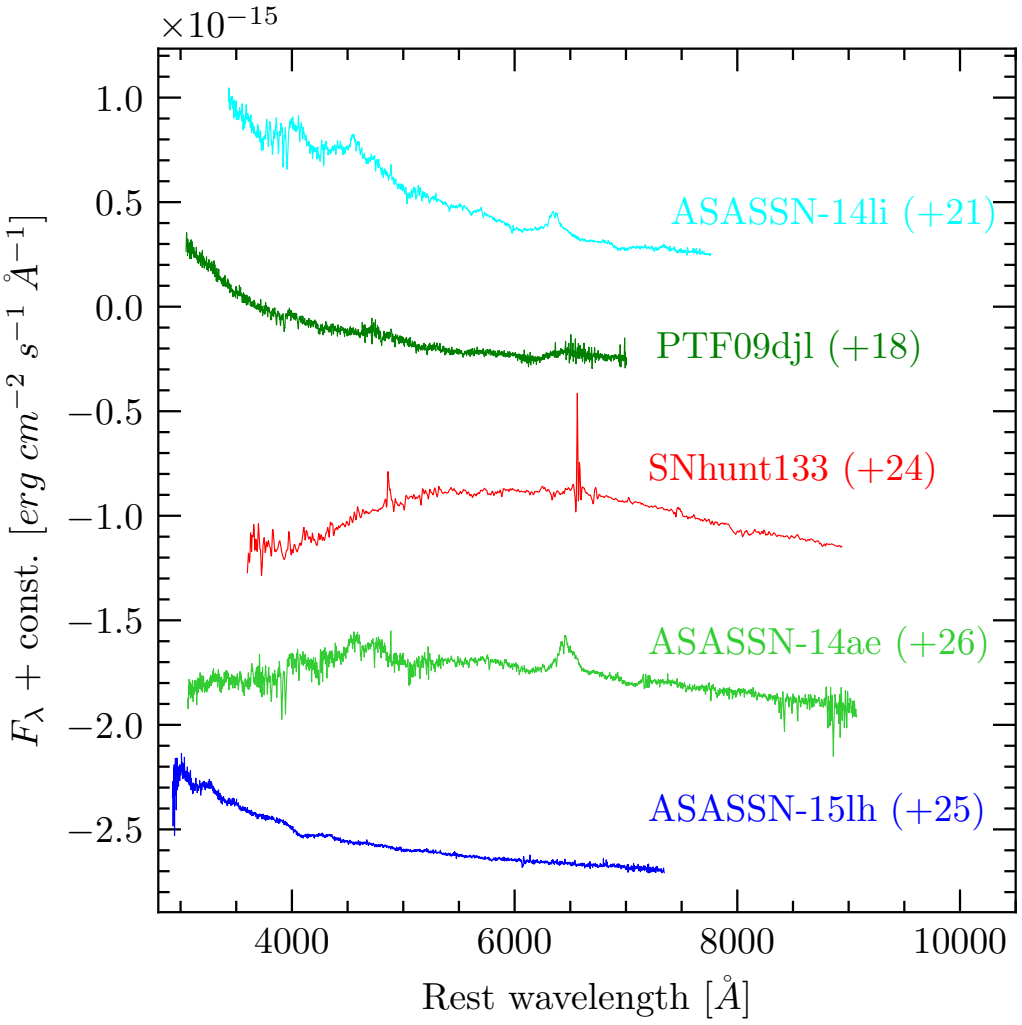

Figure 6.3: An early spectrum of SNhunt133 is compared to spectra of different SNe in a similar phase. The objects considered for the comparison are: ASASSN-14li [Holoien et al., 2016], PTF09djl [Arcavi et al., 2014], ASASSN-14ae [Holoien et al., 2014] and ASASSN-15lh [Dong et al., 2016].

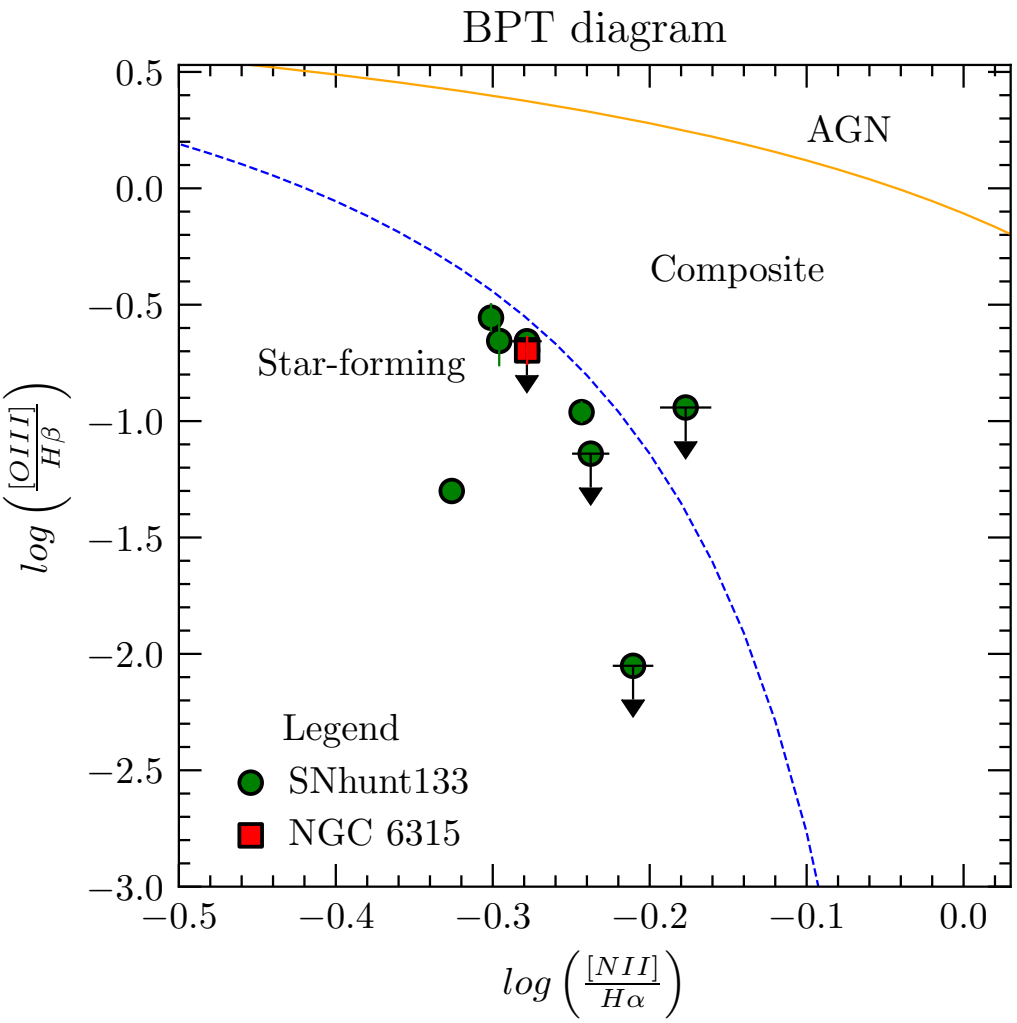

Figure 6.4: BPT diagram of SNhunt133. The dashed blue line divides the region of star-forming galaxies from composite ones, as derived from [Kauffmann et al., 2003], whereas the solid orange line separates composite galaxies from AGN, as retrieved from [Kewley et al., 2001]. The red square indicates the galactic nucleus without the transient.

The evolution of line ratios displayed in Section 5.3 identifies the host of SNhunt133 as a star-forming galaxy and not an AGN. Nevertheless, we cannot rule out the possibility that we are observing a novel type of variability of the nucleus of a seemingly quiescent galaxy, less evident and less recurring of the one typically observed in AGN.

ACKNOWLEDGEMENTS

It has been less than two years since my last degree. In that occasion, heartfelt thanks were given out (cfr. "Performance study of new photosensors for Gamma-ray Astronomy"). Since then, some people have gone but many others have come in. This arises the need to another round of THANK YOU.
First and foremost, my advisor Prof. Stefano Ciroi, who has been the most accomodating and helpful supervisor one could hope for.
Secondly, Dr. Andrea Pastorello receives the biggest "thank you" I am capable of. He has always been present for each step of the reduction, of the analysis and of the writing. He shaped this work into something I am really proud of.
All the members of the INAF supernova team in Padua (and some others around the world) have been supportive of my work, cheering for me from the sidelines and lending a hand when the need arose.
The constant support I received from my family is perhaps my most unyielding cornerstone, and it gave this thesis the backbone it needed to be completed. I do not think I would have been able to finish a master degree in such a short time without them.
Some friends have been walking with me for a long time now, others instead joined more recently. I would be lying if I affirmed that I love them all equally, but each and every one of them means the world to me. Astronomers and non-astronomers alike, their companionship made my journey the marvellous adventure it has been.
A particular "thank you" is for a person that is very dear to me. I reckon everyone reading these lines knows whom I am referring to. I shall leave the name pending but, quoting a very famous film, "I would've been lost without you".

BIBLIOGRAPHY

[Abbott et al., 2008] Abbott, B., Abbott, R., and Adhikari, R., e. a. (2008). Search for gravitational waves associated with 39 gamma-ray bursts using data from the second, third, and fourth LIGO runs. *Physical Review D*, 77(6):062004.

[Abbott et al., 2017a] Abbott, B. P., Abbott, R., and Abbott, T. D., e. a. (2017a). GW170817: Observation of Gravitational Waves from a Binary Neutron Star Inspiral. *Physical Review Letters*, 119(16):161101.

[Abbott et al., 2017b] Abbott, B. P., Abbott, R., and Abbott, T. D., e. a. (2017b). Multi-messenger Observations of a Binary Neutron Star Merger. *Astrophysical Journal, Letters*, 848(2):L12.

[Abdo et al., 2009] Abdo, A. A., Ackermann, M., and Ajello, M., e. a. (2009). Fermi Discovery of Gamma-ray Emission from NGC 1275. *Astrophysical Journal*, 699(1):31–39.

[Allen and Cox, 2001] Allen, C. W. and Cox, A. N. (2001). *Allen's astrophysical quantities*. Springer Science & Business Media.

[Antonucci, 1993] Antonucci, R. (1993). Unified models for active galactic nuclei and quasars. *Annual Review of Astron and Astrophys*, 31:473–521.

[Arav et al., 1998] Arav, N., Barlow, T. A., and Laor, Ari, e. a. (1998). Are AGN broad emission lines formed by discrete clouds? Analysis of Keck high-resolution spectroscopy of NGC 4151. *Monthly Notices of the RAS*, 297(4):990–998.

[Arcavi et al., 2014] Arcavi, I., Gal-Yam, A., and Sullivan, Mark, e. a. (2014). A Continuum of H- to He-rich Tidal Disruption Candidates With a Preference for E+A Galaxies. *Astrophysical Journal*, 793(1):38.

[Arnett, 1969] Arnett, W. D. (1969). A Possible Model of Supernovae: Detonation of ^{12}C. *Astrophysics and Space Science*, 5(2):180–212.

[Auchettl et al., 2018] Auchettl, K., Ramirez-Ruiz, E., and Guillochon, J. (2018). A Comparison of the X-Ray Emission from Tidal Disruption Events with those of Active Galactic Nuclei. *Astrophysical Journal*, 852(1):37.

[Baillard et al., 2011] Baillard, A., Bertin, E., and de Lapparent, V., e. a. (2011). The EFIGI catalogue of 4458 nearby galaxies with detailed morphology. *Astronomy and Astrophysics*, 532:A74.

[Baldini, 2015] Baldini, U. (2015). *JET'S POWER IN RADIO-LOUD ACTIVE GALACTIC NUCLEI: A CASE STUDY ON THE NATURE OF BLAZAR CANDIDATES*. PhD thesis.

[Baldwin et al., 1981] Baldwin, J. A., Phillips, M. M., and Terlevich, R. (1981). Classification parameters for the emission-line spectra of extragalactic objects. *Publications of the ASP*, 93:5–19.

[Baloković et al., 2012] Baloković, M., Smolčić, V., and Ivezić, Ž., e. a. (2012). Disclosing the Radio Loudness Distribution Dichotomy in Quasars: An Unbiased Monte Carlo Approach Applied to the SDSS-FIRST Quasar Sample. *Astrophysical Journal*, 759(1):30.

[Barkat, 1975] Barkat, Z. (1975). Neutrino processes in stellar interiors. *Annual Review of Astron and Astrophys*, 13:45–68.

[Barvainis, 1987] Barvainis, R. (1987). Hot Dust and the Near-Infrared Bump in the Continuum Spectra of Quasars and Active Galactic Nuclei. *Astrophysical Journal*, 320:537.

[Benetti et al., 2006] Benetti, S., Cappellaro, E., and Turatto, M., e. a. (2006). Supernova 2002ic: The Collapse of a Stripped-Envelope, Massive Star in a Dense Medium? *Astrophysical Journal, Letters*, 653(2):L129–L132.

[Bentz et al., 2013] Bentz, M. C., Denney, K. D., and Grier, Catherine J., e. a. (2013). The Low-luminosity End of the Radius-Luminosity Relationship for Active Galactic Nuclei. *Astrophysical Journal*, 767(2):149.

[Bethe, 1990] Bethe, H. A. (1990). Supernova mechanisms. *Reviews of Modern Physics*, 62(4):801–866.

[Bianco et al., 2014] Bianco, F. B., Modjaz, M., and Hicken, M., e. a. (2014). Multi-color Optical and Near-infrared Light Curves of 64 Stripped-envelope Core-Collapse Supernovae. *Astrophysical Journal, Supplement*, 213(2):19.

[Blagorodnova et al., 2018] Blagorodnova, N., Neill, J. D., and Walters, Richard, e. a. (2018). The SED Machine: A Robotic Spectrograph for Fast Transient Classification. *Publications of the ASP*, 130(985):035003.

[Bonnerot et al., 2017] Bonnerot, C., Rossi, E. M., and Lodato, G. (2017). Long-term stream evolution in tidal disruption events. *Monthly Notices of the RAS*, 464(3):2816–2830.

[Boylan-Kolchin et al., 2008] Boylan-Kolchin, M., Ma, C.-P., and Quataert, E. (2008). Dynamical friction and galaxy merging time-scales. *Monthly Notices of the RAS*, 383(1):93–101.

[Brachwitz et al., 2000] Brachwitz, F., Dean, D. J., and Hix, W. Raphael, e. a. (2000). The Role of Electron Captures in Chandrasekhar-Mass Models for Type IA Supernovae. *Astrophysical Journal*, 536(2):934–947.

[Branch and Wheeler, 2017] Branch, D. and Wheeler, J. C. (2017). *Supernova explosions*. Springer.

[Burrows, 2013] Burrows, A. (2013). Colloquium: Perspectives on core-collapse supernova theory. *Reviews of Modern Physics*, 85(1):245–261.

[Cai, 2019] Cai, Y. Z. (2019). *Intermediate Luminosity Optical Transients*. PhD thesis.

[Carroll and Ostlie, 2017] Carroll, B. W. and Ostlie, D. A. (2017). *An introduction to modern astrophysics*. Cambridge University Press.

[Carter and Luminet, 1982] Carter, B. and Luminet, J. P. (1982). Pancake detonation of stars by black holes in galactic nuclei. *Nature*, 296(5854):211–214.

[Cenko et al., 2016] Cenko, S. B., Cucchiara, A., and Roth, Nathaniel, e. a. (2016). An Ultraviolet Spectrum of the Tidal Disruption Flare ASASSN-14li. *Astrophysical Journal, Letters*, 818(2):L32.

[Chen et al., 2011] Chen, X., Sesana, A., Madau, P., and Liu, F. K. (2011). Tidal Stellar Disruptions by Massive Black Hole Pairs. II. Decaying Binaries. *Astrophysical Journal*, 729(1):13.

[Chevalier et al., 1994] Chevalier, R. A., Fransson, C., and Lundqvist, P. (1994). Shock phenomena around SN 1993J. In *Bulletin of the AAS*, volume 26, page 791.

[Chonis and Gaskell, 2007] Chonis, T. S. and Gaskell, C. M. (2007). Setting ubvri photometric zero-points using sloan digital sky survey ugriz magnitudes. *The Astronomical Journal*, 135(1):264–267.

[Churazov et al., 2001] Churazov, E., Gilfanov, M., and Revnivtsev, M. (2001). Soft state of Cygnus X-1: stable disc and unstable corona. *Monthly Notices of the RAS*, 321(4):759–766.

[Coughlin and Nixon, 2019] Coughlin, E. R. and Nixon, C. J. (2019). Partial Stellar Disruption by a Supermassive Black Hole: Is the Light Curve Really Proportional to t $^{-9/4}$? *Astrophysical Journal, Letters*, 883(1):L17.

[Dai et al., 2015] Dai, L., McKinney, J. C., and Miller, M. C. (2015). Soft X-Ray Temperature Tidal Disruption Events from Stars on Deep Plunging Orbits. *Astrophysical Journal, Letters*, 812(2):L39.

[Dai et al., 2018] Dai, L., McKinney, J. C., and Roth, Nathaniel, e. a. (2018). A Unified Model for Tidal Disruption Events. *Astrophysical Journal, Letters*, 859(2):L20.

[De Vaucouleurs et al., 1991] De Vaucouleurs, De Vaucouleurs, and Corwin, e. a. (1991). Third Reference Catalogue of Bright Galaxies, version 3.9.

[Done, 2010] Done, C. (2010). Observational characteristics of accretion onto black holes. *arXiv e-prints*, page arXiv:1008.2287.

[Dong et al., 2016] Dong, S., Shappee, B. J., and Prieto, J. L., e. a. (2016). ASASSN-15lh: A highly super-luminous supernova. *Science*, 351(6270):257–260.

[Drake, 2012] Drake, A. J. (2012). SNhunt133, an AGN outburst? *The Astronomer's Telegram*, 4279:1.

[Dressler and Gunn, 1983] Dressler, A. and Gunn, J. E. (1983). Spectroscopy of galaxies in distant clusters. II. The population of the 3C 295 cluster. *Astrophysical Journal*, 270:7–19.

[Drout et al., 2011] Drout, M. R., Soderberg, A. M., and Gal-Yam, Avishay, e. a. (2011). The First Systematic Study of Type Ibc Supernova Multi-band Light Curves. *Astrophysical Journal*, 741(2):97.

[Elitzur and Shlosman, 2006] Elitzur, M. and Shlosman, I. (2006). The AGN-obscuring Torus: The End of the "Doughnut" Paradigm? *Astrophysical Journal, Letters*, 648(2):L101–L104.

[Elvis, 2000] Elvis, M. (2000). A Structure for Quasars. *Astrophysical Journal*, 545(1):63–76.

[Evans and Kochanek, 1989] Evans, C. R. and Kochanek, C. S. (1989). The Tidal Disruption of a Star by a Massive Black Hole. *Astrophysical Journal, Letters*, 346:L13.

[Falcke et al., 1998] Falcke, H., Wilson, A. S., and Simpson, C. (1998). Hubble Space Telescope and VLA Observations of Seyfert 2 Galaxies: The Relationship between Radio Ejecta and the Narrow-Line Region. *Astrophysical Journal*, 502(1):199–217.

[Fausnaugh et al., 2016] Fausnaugh, M. M., Denney, K. D., and Barth, A. J., e. a. (2016). Space Telescope and Optical Reverberation Mapping Project. III. Optical Continuum Emission and Broadband Time Delays in NGC 5548. *Astrophysical Journal*, 821(1):56.

[Ferland and Mushotzky, 1982] Ferland, G. J. and Mushotzky, R. F. (1982). Broad line region clouds and the absorbing material in NGC 4151. *Astrophysical Journal*, 262:564–577.

[Filippenko, 1997] Filippenko, A. V. (1997). Optical Spectra of Supernovae. *Annual Review of Astron and Astrophys*, 35:309–355.

[Foley et al., 2013] Foley, R. J., Challis, P. J., and Chornock, R., e. a. (2013). Type Iax Supernovae: A New Class of Stellar Explosion. *Astrophysical Journal*, 767(1):57.

[French et al., 2016] French, K. D., Arcavi, I., and Zabludoff, A. (2016). Tidal Disruption Events Prefer Unusual Host Galaxies. *Astrophysical Journal, Letters*, 818(1):L21.

[French et al., 2017] French, K. D., Arcavi, I., and Zabludoff, A. (2017). The Post-starburst Evolution of Tidal Disruption Event Host Galaxies. *Astrophysical Journal*, 835(2):176.

[French et al., 2020a] French, K. D., Arcavi, I., and Zabludoff, Ann I., e. a. (2020a). The Structure of Tidal Disruption Event Host Galaxies on Scales of Tens to Thousands of Parsecs. *Astrophysical Journal*, 891(1):93.

[French et al., 2020b] French, K. D., Wevers, T., and Law-Smith, Jamie, e. a. (2020b). The Host Galaxies of Tidal Disruption Events. *arXiv e-prints*, page arXiv:2003.02863.

[Fujimoto, 1982] Fujimoto, M. Y. (1982). A Theory of Hydrogen Shell Flashes on Accreting White Dwarfs - Part Two - the Stable Shell Burning and the Recurrence Period of Shell Flashes. *Astrophysical Journal*, 257:767.

[Gal-Yam, 2017] Gal-Yam, A. (2017). *Observational and Physical Classification of Supernovae*, page 195.

[Gezari et al., 2017] Gezari, S., Cenko, S. B., and Arcavi, I. (2017). X-Ray Brightening and UV Fading of Tidal Disruption Event ASASSN-15oi. *Astrophysical Journal, Letters*, 851(2):L47.

[Gezari et al., 2012] Gezari, S., Chornock, R., and Rest, A., e. a. (2012). An ultraviolet-optical flare from the tidal disruption of a helium-rich stellar core. *Nature*, 485(7397):217–220.

[Gierliński and Done, 2004] Gierliński, M. and Done, C. (2004). Is the soft excess in active galactic nuclei real? *Monthly Notices of the RAS*, 349(1):L7–L11.

[Giveon et al., 1999] Giveon, U., Maoz, D., and Kaspi, Shai, e. a. (1999). Long-term optical variability properties of the Palomar-Green quasars. *Monthly Notices of the RAS*, 306(3):637–654.

[Goldreich and Weber, 1980] Goldreich, P. and Weber, S. V. (1980). Homologously collapsing stellar cores. *Astrophysical Journal*, 238:991–997.

[Graur et al., 2018] Graur, O., French, K. D., and Zahid, H. Jabran, e. a. (2018). A Dependence of the Tidal Disruption Event Rate on Global Stellar Surface Mass Density and Stellar Velocity Dispersion. *Astrophysical Journal*, 853(1):39.

[Guillochon et al., 2014] Guillochon, J., Manukian, H., and Ramirez-Ruiz, E. (2014). PS1-10jh: The Disruption of a Main-sequence Star of Near-solar Composition. *Astrophysical Journal*, 783(1):23.

[Guillochon and Ramirez-Ruiz, 2015] Guillochon, J. and Ramirez-Ruiz, E. (2015). A Dark Year for Tidal Disruption Events. *Astrophysical Journal*, 809(2):166.

[Hamann et al., 2018] Hamann, F., Chartas, G., Reeves, J., and Nardini, E. (2018). Does the X-ray outflow quasar PDS 456 have a UV outflow at 0.3c? *Monthly Notices of the RAS*, 476(1):943–953.

[Hills, 1975] Hills, J. G. (1975). Possible power source of Seyfert galaxies and QSOs. *Nature*, 254(5498):295–298.

[Hinkle et al., 2020] Hinkle, J. T., Holoien, T. W. S., and Shappee, Benjamin. J., e. a. (2020). Peak-Luminosity/Decline-Rate Relationship for Tidal Disruption Events. *arXiv e-prints*, page arXiv:2001.08215.

[Höflich et al., 2004] Höflich, P., Gerardy, C. L., and Nomoto, Ken'ichi, e. a. (2004). Signature of Electron Capture in Iron-rich Ejecta of SN 2003du. *Astrophysical Journal*, 617(2):1258–1266.

[Hogg and Reynolds, 2016] Hogg, J. D. and Reynolds, C. S. (2016). Testing the Propagating Fluctuations Model with a Long, Global Accretion Disk Simulation. *Astrophysical Journal*, 826(1):40.

[Holoien et al., 2019] Holoien, T. W. S., Huber, M. E., and Shappee, B. J., e. a. (2019). PS18kh: A New Tidal Disruption Event with a Non-axisymmetric Accretion Disk. *Astrophysical Journal*, 880(2):120.

[Holoien et al., 2016] Holoien, T. W. S., Kochanek, C. S., and Prieto, J. L., e. a. (2016). Six months of multiwavelength follow-up of the tidal disruption candidate ASASSN-14li and implied TDE rates from ASAS-SN. *Monthly Notices of the RAS*, 455(3):2918–2935.

[Holoien et al., 2014] Holoien, T. W. S., Prieto, J. L., and Bersier, D., e. a. (2014). ASASSN-14ae: a tidal disruption event at 200 Mpc. *Monthly Notices of the RAS*, 445(3):3263–3277.

[Hosseinzadeh et al., 2017] Hosseinzadeh, G., Arcavi, I., and Valenti, Stefano, e. a. (2017). Type Ibn Supernovae Show Photometric Homogeneity and Spectral Diversity at Maximum Light. *Astrophysical Journal*, 836(2):158.

[Howell, 2017] Howell, D. A. (2017). *Superluminous Supernovae*, page 431.

[Humphreys and Davidson, 1994] Humphreys, R. M. and Davidson, K. (1994). The Luminous Blue Variables: Astrophysical Geysers. *Publications of the ASP*, 106:1025.

[Hung et al., 2017] Hung, T., Gezari, S., and Blagorodnova, N., e. a. (2017). Revisiting Optical Tidal Disruption Events with iPTF16axa. *Astrophysical Journal*, 842(1):29.

[Inserra et al., 2013] Inserra, C., Smartt, S. J., and Jerkstrand, A., e. a. (2013). Super-luminous Type Ic Supernovae: Catching a Magnetar by the Tail. *Astrophysical Journal*, 770(2):128.

[Ivanov et al., 2005] Ivanov, P. B., Polnarev, A. G., and Saha, P. (2005). The tidal disruption rate in dense galactic cusps containing a supermassive binary black hole. *Monthly Notices of the RAS*, 358(4):1361–1378.

[Janka, 2012] Janka, H.-T. (2012). Explosion Mechanisms of Core-Collapse Supernovae. *Annual Review of Nuclear and Particle Science*, 62(1):407–451.

[Jiang et al., 2016] Jiang, Y.-F., Guillochon, J., and Loeb, A. (2016). Prompt Radiation and Mass Outflows from the Stream-Stream Collisions of Tidal Disruption Events. *Astrophysical Journal*, 830(2):125.

[Kankare et al., 2017] Kankare, E., Kotak, R., Mattila, S., and Lundqvist, P. (2017). A new population of highly energetic nuclear transients. *Nature Astronomy*, 1(12):865–871.

[Kashyap et al., 2019] Kashyap, R., Raman, G., and Parameswaran, A. (2019). Can Kilonova Light Curves Be Standardized? *Astrophysical Journal, Letters*, 886(1):L19.

[Kasliwal, 2012] Kasliwal, M. M. (2012). Systematically Bridging the Gap Between Novae and Supernovae. *Publications of the Astron. Soc. of Australia*, 29(4):482–488.

[Kasliwal et al., 2012] Kasliwal, M. M., Kulkarni, S. R., and Gal-Yam, Avishay, e. a. (2012). Calcium-rich Gap Transients in the Remote Outskirts of Galaxies. *Astrophysical Journal*, 755(2):161.

[Kauffmann et al., 2003] Kauffmann, G., Heckman, T. M., and Tremonti, Christy, e. a. (2003). The host galaxies of active galactic nuclei. *Monthly Notices of the RAS*, 346(4):1055–1077.

[Kawaguchi et al., 2020] Kawaguchi, K., Shibata, M., and Tanaka, M. (2020). Diversity of Kilonova Light Curves. *Astrophysical Journal*, 889(2):171.

[Kewley et al., 2001] Kewley, L. J., Dopita, M. A., and Sutherland, R. S., e. a. (2001). Theoretical Modeling of Starburst Galaxies. *Astrophysical Journal*, 556(1):121–140.

[Khokhlov, 1991] Khokhlov, A. M. (1991). Delayed detonation model for type IA supernovae. *Astronomy and Astrophysics*, 245(1):114–128.

[Khokhlov et al., 1997] Khokhlov, A. M., Oran, E. S., and Wheeler, J. C. (1997). Deflagration-to-Detonation Transition in Thermonuclear Supernovae. *Astrophysical Journal*, 478(2):678–688.

[Kochanek, 2016] Kochanek, C. S. (2016). Tidal disruption event demographics. *Monthly Notices of the RAS*, 461(1):371–384.

[Komossa, 2015] Komossa, S. (2015). Tidal disruption of stars by supermassive black holes: Status of observations. *Journal of High Energy Astrophysics*, 7:148–157.

[Koratkar and Blaes, 1999] Koratkar, A. and Blaes, O. (1999). The Ultraviolet and Optical Continuum Emission in Active Galactic Nuclei: The Status of Accretion Disks. *Publications of the ASP*, 111(755):1–30.

[Kouveliotou et al., 1993] Kouveliotou, C., Meegan, C. A., and Fishman, Gerald J., e. a. (1993). Identification of Two Classes of Gamma-Ray Bursts. *Astrophysical Journal, Letters*, 413:L101.

[Krolik et al., 2020] Krolik, J., Piran, T., and Ryu, T. (2020). Tidal Disruptions of Main Sequence Stars – V. The Varieties of Disruptions. *arXiv e-prints*, page arXiv:2001.03234.

[Krolik et al., 2016] Krolik, J., Piran, T., Svirski, G., and Cheng, R. M. (2016). ASASSN-14li: A Model Tidal Disruption Event. *Astrophysical Journal*, 827(2):127.

[Lacy et al., 1982] Lacy, J. H., Townes, C. H., and Hollenbach, D. J. (1982). The nature of the central parsec of the Galaxy. *Astrophysical Journal*, 262:120–134.

[Law-Smith et al., 2017] Law-Smith, J., Ramirez-Ruiz, E., Ellison, S. L., and Foley, R. J. (2017). Tidal Disruption Event Host Galaxies in the Context of the Local Galaxy Population. *Astrophysical Journal*, 850(1):22.

[Leighly et al., 2001] Leighly, K. M., Halpern, J. P., and Helfand, D. J., e. a. (2001). FIRST Observations of the Second-Brightest Quasar. *Astronomical Journal*, 121(6):2889–2894.

[Leloudas et al., 2019] Leloudas, G., Dai, L., and Arcavi, Iair, e. a. (2019). The Spectral Evolution of AT 2018dyb and the Presence of Metal Lines in Tidal Disruption Events. *Astrophysical Journal*, 887(2):218.

[Lunnan et al., 2016] Lunnan, R., Chornock, R., and Berger, E., e. a. (2016). PS1-14bj: A Hydrogen-poor Superluminous Supernova With a Long Rise and Slow Decay. *Astrophysical Journal*, 831(2):144.

[Lyubarskii, 1997] Lyubarskii, Y. E. (1997). Flicker noise in accretion discs. *Monthly Notices of the RAS*, 292(3):679–685.

[Marconi and Hunt, 2003] Marconi, A. and Hunt, L. K. (2003). The Relation between Black Hole Mass, Bulge Mass, and Near-Infrared Luminosity. *Astrophysical Journal, Letters*, 589(1):L21–L24.

[Marscher and Gear, 1985] Marscher, A. P. and Gear, W. K. (1985). Models for high-frequency radio outbursts in extragalactic sources, with application to the early 1983 millimeter-to-infrared flare of 3C 273. *Astrophysical Journal*, 298:114–127.

[Mattila et al., 2018] Mattila, S., Pérez-Torres, M., and Efstathiou, A., e. a. (2018). A dust-enshrouded tidal disruption event with a resolved radio jet in a galaxy merger. *Science*, 361(6401):482–485.

[Mazzali et al., 2005] Mazzali, P. A., Kawabata, K. S., and Maeda, Keiichi, e. a. (2005). An Asymmetric Energetic Type Ic Supernova Viewed Off-Axis, and a Link to Gamma Ray Bursts. *Science*, 308(5726):1284–1287.

[McCrum et al., 2012] McCrum, M., Fraser, M., and Kotak, R., e. a. (2012). SNhunt133 is an AGN in NGC 6315. *The Astronomer's Telegram*, 4274:1.

[Metzger and Stone, 2016] Metzger, B. D. and Stone, N. C. (2016). A bright year for tidal disruptions. *Monthly Notices of the RAS*, 461(1):948–966.

[Metzger and Stone, 2017] Metzger, B. D. and Stone, N. C. (2017). Periodic Accretion-powered Flares from Colliding EMRIs as TDE Imposters. *Astrophysical Journal*, 844(1):75.

[Miller, 2015] Miller, M. C. (2015). Disk Winds as an Explanation for Slowly Evolving Temperatures in Tidal Disruption Events. *Astrophysical Journal*, 805(1):83.

[Mobberley, 1999] Mobberley, M. (1999). Novae. *Journal of the British Astronomical Association*, 109:57–69.

[Modjaz, 2007] Modjaz, M. (2007). *Varied deaths of massive stars: Properties of nearby type IIb, Ib and Ic supernovae.* PhD thesis, Harvard University.

[Modjaz et al., 2014] Modjaz, M., Blondin, S., and Kirshner, R. P., e. a. (2014). Optical Spectra of 73 Stripped-envelope Core-collapse Supernovae. *Astronomical Journal*, 147(5):99.

[Moorwood, 1999] Moorwood, A. (1999). *ISO Observations of AGN (invited talk)*, volume 177 of *Astronomical Society of the Pacific Conference Series*, page 141.

[Mould et al., 2000] Mould, J. R., Huchra, J. P., and Freedman, Wendy L., e. a. (2000). The Hubble Space Telescope Key Project on the Extragalactic Distance Scale. XXVIII. Combining the Constraints on the Hubble Constant. *Astrophysical Journal*, 529(2):786–794.

[Mukherjee et al., 1998] Mukherjee, S., Feigelson, E. D., and Jogesh Babu, Gutti, e. a. (1998). Three Types of Gamma-Ray Bursts. *Astrophysical Journal*, 508(1):314–327.

[Netzer, 1990] Netzer, H. (1990). AGN emission lines. In Blandford, R. D., Netzer, H., Woltjer, L., Courvoisier, T. J. L., and Mayor, M., editors, *Active Galactic Nuclei*, pages 57–160.

[Netzer et al., 1996] Netzer, H., Heller, A., and Loinger, Friedel, e. a. (1996). Optical monitoring of luminous AGN - I. Radio-loud quasars. *Monthly Notices of the RAS*, 279(2):429–446.

[Neufeld et al., 1994] Neufeld, D. A., Maloney, P. R., and Conger, S. (1994). Water maser emission from X-ray-heated circumnuclear gas in active galaxies. *Astrophysical Journal, Letters*, 436:L127–L130.

[Nicholl et al., 2019] Nicholl, M., Blanchard, P. K., and Berger, E., e. a. (2019). The tidal disruption event AT2017eqx: spectroscopic evolution from hydrogen rich to poor suggests an atmosphere and outflow. *Monthly Notices of the RAS*, 488(2):1878–1893.

[Nicholl et al., 2013] Nicholl, M., Smartt, S. J., and Jerkstrand, A., e. a. (2013). Slowly fading super-luminous supernovae that are not pair-instability explosions. *Nature*, 502(7471):346–349.

[Nomoto, 1984] Nomoto, K. (1984). Evolution of 8-10 solar mass stars toward electron capture supernovae. I - Formation of electron-degenerate O + NE + MG cores. *Astrophysical Journal*, 277:791–805.

[Olson, 1975] Olson, B. I. (1975). On the ratio of total-to-selective absorption. *Publications of the ASP*, 87:349–351.

[Paczyński, 1972] Paczyński, B. (1972). Carbon Ignition in Degenerate Stellar Cores. *Astrophysics Letters*, 11:53.

[Padovani et al., 2017] Padovani, P., Alexander, D. M., and Assef, R. J., e. a. (2017). Active galactic nuclei: what's in a name? *Astronomy and Astrophysics Reviews*, 25(1):2.

[Pastorello and Fraser, 2019] Pastorello, A. and Fraser, M. (2019). Supernova impostors and other gap transients. *Nature Astronomy*, 3:676–679.

[Pastorello et al., 2019] Pastorello, A., Mason, E., and Taubenberger, S., e. a. (2019). Luminous red novae: Stellar mergers or giant eruptions? *Astronomy and Astrophysics*, 630:A75.

[Pastorello et al., 2008] Pastorello, A., Mattila, S., and Zampieri, L., e. a. (2008). Massive stars exploding in a He-rich circumstellar medium - I. Type Ibn (SN 2006jc-like) events. *Monthly Notices of the RAS*, 389(1):113–130.

[Pastorello et al., 2010] Pastorello, A., Smartt, S. J., and Botticella, M. T., e. a. (2010). Ultra-bright Optical Transients are Linked with Type Ic Supernovae. *Astrophysical Journal, Letters*, 724(1):L16–L21.

[Pastorello et al., 2016] Pastorello, A., Wang, X. F., and Ciabattari, F., e. a. (2016). Massive stars exploding in a He-rich circumstellar medium - IX. SN 2014av, and characterization of Type Ibn SNe. *Monthly Notices of the RAS*, 456(1):853–869.

[Perets et al., 2010] Perets, H. B., Gal-Yam, A., and Mazzali, P. A., e. a. (2010). A faint type of supernova from a white dwarf with a helium-rich companion. *Nature*, 465(7296):322–325.

[Phillips, 1993] Phillips, M. M. (1993). The Absolute Magnitudes of Type IA Supernovae. *Astrophysical Journal, Letters*, 413:L105.

[Pian et al., 2017] Pian, E., D'Avanzo, P., and Benetti, S., e. a. (2017). Spectroscopic identification of r-process nucleosynthesis in a double neutron-star merger. *Nature*, 551(7678):67–70.

[Piran, 2004] Piran, T. (2004). The physics of gamma-ray bursts. *Reviews of Modern Physics*, 76(4):1143–1210.

[Piran et al., 2015] Piran, T., Svirski, G., and Krolik, Julian, e. a. (2015). Disk Formation Versus Disk Accretion: What Powers Tidal Disruption Events? *Astrophysical Journal*, 806(2):164.

[Ponti et al., 2010] Ponti, G., Gallo, L. C., and Fabian, A. C., e. a. (2010). Relativistic disc reflection in the extreme NLS1 IRAS13224-3809. *Monthly Notices of the RAS*, 406(4):2591–2604.

[Poznanski et al., 2012] Poznanski, D., Prochaska, J. X., and Bloom, J. S. (2012). An empirical relation between sodium absorption and dust extinction. *Monthly Notices of the Royal Astronomical Society*, 426(2):1465–1474.

[Quimby et al., 2011] Quimby, R. M., Kulkarni, S. R., and Kasliwal, M. M., e. a. (2011). Hydrogen-poor superluminous stellar explosions. *Nature*, 474(7352):487–489.

[Rees, 1988] Rees, M. J. (1988). Tidal disruption of stars by black holes of 10^6-10^8 solar masses in nearby galaxies. *Nature*, 333(6173):523–528.

[Reynolds et al., 2014] Reynolds, C., Ueda, Y., and Awaki, H., e. a. (2014). Astro-h white paper - agn reflection.

[Richardson et al., 2014] Richardson, D., Jenkins, Robert L., I., Wright, J., and Maddox, L. (2014). Absolute-magnitude Distributions of Supernovae. *Astronomical Journal*, 147(5):118.

[Risaliti, 2010] Risaliti, G. (2010). AGN structure from X-ray absorption variability. In Comastri, A., Angelini, L., and Cappi, M., editors, *X-ray Astronomy 2009; Present Status, Multi-Wavelength Approach and Future Perspectives*, volume 1248 of *American Institute of Physics Conference Series*, pages 351–354.

[Risaliti and Elvis, 2004] Risaliti, G. and Elvis, M. (2004). *A Panchromatic View of AGN*, volume 308 of *Astrophysics and Space Science Library*, page 187.

[Rose, 1968] Rose, W. K. (1968). A Model for the Nova Outburst. *Astrophysical Journal*, 152:245.

[Ryu et al., 2020] Ryu, T., Krolik, J., Piran, T., and Noble, S. C. (2020). Tidal Disruptions of Main Sequence Stars – I. Observable Quantities and their Dependence on Stellar and Black Hole Mass. *arXiv e-prints*, page arXiv:2001.03501.

[Sagar et al., 2004] Sagar, R., Stalin, C. S., Gopal-Krishna, and Wiita, P. J. (2004). Intranight optical variability of blazars. *Monthly Notices of the RAS*, 348(1):176–186.

[Schlafly and Finkbeiner, 2011] Schlafly, E. F. and Finkbeiner, D. P. (2011). Measuring Reddening with Sloan Digital Sky Survey Stellar Spectra and Recalibrating SFD. *Astrophysical Journal*, 737(2):103.

[Schlegel, 1990] Schlegel, E. M. (1990). A new subclass of type II supernovae ? *Monthly Notices of the RAS*, 244:269–271.

[Silverman et al., 2013] Silverman, J. M., Nugent, P. E., and Gal-Yam, Avishay, e. a. (2013). Type Ia Supernovae Strongly Interacting with Their Circumstellar Medium. *Astrophysical Journal, Supplement*, 207(1):3.

[Stalin et al., 2004] Stalin, C. S., Gopal-Krishna, Sagar, R., and Wiita, P. J. (2004). Intranight optical variability of radio-quiet and radio lobe-dominated quasars. *Monthly Notices of the RAS*, 350(1):175–188.

[Stone and Metzger, 2016] Stone, N. C. and Metzger, B. D. (2016). Rates of stellar tidal disruption as probes of the supermassive black hole mass function. *Monthly Notices of the RAS*, 455(1):859–883.

[Suganuma et al., 2006] Suganuma, M., Yoshii, Y., and Kobayashi, Yukiyasu, e. a. (2006). Reverberation Measurements of the Inner Radius of the Dust Torus in Nearby Seyfert 1 Galaxies. *Astrophysical Journal*, 639(1):46–63.

[Taddia et al., 2016] Taddia, F., Sollerman, J., and Fremling, C., e. a. (2016). Long-rising Type II supernovae from Palomar Transient Factory and Caltech Core-Collapse Project. *Astronomy and Astrophysics*, 588:A5.

[Tartaglia et al., 2015] Tartaglia, L., Pastorello, A., and Taubenberger, S., e. a. (2015). Interacting supernovae and supernova impostors. SN 2007sv: the major eruption of a massive star in UGC 5979. *Monthly Notices of the RAS*, 447(1):117–131.

[Taubenberger, 2017] Taubenberger, S. (2017). *The Extremes of Thermonuclear Supernovae*, page 317.

[Taubenberger et al., 2008] Taubenberger, S., Hachinger, S., and Pignata, G., e. a. (2008). The underluminous Type Ia supernova 2005bl and the class of objects similar to SN 1991bg. *Monthly Notices of the RAS*, 385(1):75–96.

[Terrell, 1967] Terrell, J. (1967). Luminosity Fluctuations and a Local Model of Quasi-Stellar Objects. *Astrophysical Journal*, 147:827.

[Thompson et al., 2009] Thompson, T. A., Prieto, J. L., and Stanek, K. Z., e. a. (2009). A New Class of Luminous Transients and a First Census of their Massive Stellar Progenitors. *Astrophysical Journal*, 705(2):1364–1384.

[Turatto, 2020] Turatto, M. (2020). Personal communication.

[Tylenda et al., 2011] Tylenda, R., Hajduk, M., and Kamiński, T., e. a. (2011). V1309 Scorpii: merger of a contact binary. *Astronomy and Astrophysics*, 528:A114.

[Uttley and McHardy, 2001] Uttley, P. and McHardy, I. M. (2001). The flux-dependent amplitude of broadband noise variability in X-ray binaries and active galaxies. *Monthly Notices of the RAS*, 323(2):L26–L30.

[Uttley et al., 2002] Uttley, P., McHardy, I. M., and Papadakis, I. E. (2002). Measuring the broad-band power spectra of active galactic nuclei with RXTE. *Monthly Notices of the RAS*, 332(1):231–250.

[Uttley et al., 2005] Uttley, P., McHardy, I. M., and Vaughan, S. (2005). Non-linear X-ray variability in X-ray binaries and active galaxies. *Monthly Notices of the RAS*, 359(1):345–362.

[van Velzen, 2018] van Velzen, S. (2018). On the Mass and Luminosity Functions of Tidal Disruption Flares: Rate Suppression due to Black Hole Event Horizons. *Astrophysical Journal*, 852(2):72.

[van Velzen et al., 2016] van Velzen, S., Anderson, G. E., and Stone, N. C., e. a. (2016). A radio jet from the optical and x-ray bright stellar tidal disruption flare ASASSN-14li. *Science*, 351(6268):62–65.

[van Velzen and Farrar, 2014] van Velzen, S. and Farrar, G. R. (2014). Measurement of the Rate of Stellar Tidal Disruption Flares. *Astrophysical Journal*, 792(1):53.

[van Velzen et al., 2011] van Velzen, S., Farrar, G. R., and Gezari, Suvi, e. a. (2011). Optical Discovery of Probable Stellar Tidal Disruption Flares. *Astrophysical Journal*, 741(2):73.

[van Velzen et al., 2019] van Velzen, S., Gezari, S., and Cenko, S. Bradley, e. a. (2019). The First Tidal Disruption Flare in ZTF: From Photometric Selection to Multi-wavelength Characterization. *Astrophysical Journal*, 872(2):198.

[van Velzen et al., 2020] van Velzen, S., Gezari, S., and Hammerstein, Erica, e. a. (2020). Seventeen Tidal Disruption Events from the First Half of ZTF Survey Observations: Entering a New Era of Population Studies. *arXiv e-prints*, page arXiv:2001.01409.

[Vanden Berk et al., 2001] Vanden Berk, D. E., Richards, G. T., and Bauer, Amanda, e. a. (2001). Composite Quasar Spectra from the Sloan Digital Sky Survey. *Astronomical Journal*, 122(2):549–564.

[Véron-Cetty et al., 2000] Véron-Cetty, M. P., Woltjer, L. L., Staveley-Smith, L., and Ekers, R. D. (2000). The nature of powerful compact radio galaxies. *Astronomy and Astrophysics*, 362:426–434.

[Vestergaard et al., 2000] Vestergaard, M., Wilkes, B. J., and Barthel, P. D. (2000). Clues to Quasar Broad-Line Region Geometry and Kinematics. *Astrophysical Journal, Letters*, 538(2):L103–L106.

[Wang and Merritt, 2004] Wang, J. and Merritt, D. (2004). Revised Rates of Stellar Disruption in Galactic Nuclei. *Astrophysical Journal*, 600(1):149–161.

[Wang et al., 2009] Wang, X., Li, W., and Filippenko, A. V., e. a. (2009). The Golden Standard Type Ia Supernova 2005cf: Observations from the Ultraviolet to the Near-Infrared Wavebands. *Astrophysical Journal*, 697(1):380–408.

[Webb and Malkan, 2000] Webb, W. and Malkan, M. (2000). Rapid Optical Variability in Active Galactic Nuclei and Quasars. *Astrophysical Journal*, 540(2):652–677.

[Wevers et al., 2019a] Wevers, T., Pasham, D. R., and van Velzen, S., e. a. (2019a). Evidence for rapid disc formation and reprocessing in the X-ray bright tidal disruption event candidate AT 2018fyk. *Monthly Notices of the RAS*, 488(4):4816–4830.

[Wevers et al., 2019b] Wevers, T., Stone, N. C., and van Velzen, Sjoert, e. a. (2019b). Black hole masses of tidal disruption event host galaxies II. *Monthly Notices of the RAS*, 487(3):4136–4152.

[Wevers et al., 2017] Wevers, T., van Velzen, S., and Jonker, Peter G., e. a. (2017). Black hole masses of tidal disruption event host galaxies. *Monthly Notices of the RAS*, 471(2):1694–1708.

[Williams, 1992] Williams, R. E. (1992). The Formation of Novae Spectra. *Astronomical Journal*, 104:725.

[Wills et al., 1985] Wills, B. J., Netzer, H., and Wills, D. (1985). Broad emission features in QSOs and active galactic nuclei. II. New observations and theory of Fe II and HI emission. *Astrophysical Journal*, 288:94–116.

[Yahil, 1983] Yahil, A. (1983). Self-similar stellar collapse. *Astrophysical Journal*, 265:1047–1055.

[Yalinewich et al., 2019] Yalinewich, A., Steinberg, E., and Piran, T., e. a. (2019). Radio emission from the unbound debris of tidal disruption events. *Monthly Notices of the RAS*, 487(3):4083–4092.